International Journal of Physical Sciences

Volume 8 Number 22 16 June, 2013

ISSN 1992-1950

Academic Journals

ABOUT IJPS

The **International Journal of Physical Sciences (IJPS)** is published weekly (one volume per year) by Academic Journals.

International Journal of Physical Sciences (IJPS) is an open access journal that publishes high-quality solicited and unsolicited articles, in English, in all Physics and chemistry including artificial intelligence, neural processing, nuclear and particle physics, geophysics, physics in medicine and biology, plasma physics, semiconductor science and technology, wireless and optical communications, materials science, energy and fuels, environmental science and technology, combinatorial chemistry, natural products, molecular therapeutics, geochemistry, cement and concrete research, metallurgy, crystallography and computer-aided materials design. All articles published in IJPS are peer-reviewed.

Submission of Manuscript

Submit manuscripts as e-mail attachment to the Editorial Office at: ijps@academicjournals.org. A manuscript number will be mailed to the corresponding author shortly after submission.

For all other correspondence that cannot be sent by e-mail, please contact the editorial office (at ijps@academicjournals.org).

The International Journal of Physical Sciences will only accept manuscripts submitted as e-mail attachments.

Please read the **Instructions for Authors** before submitting your manuscript. The manuscript files should be given the last name of the first author.

Editors

Editorial Board

Instructions for Author

Electronic submission of manuscripts is strongly encouraged, provided that the text, tables, and figures are included in a single Microsoft Word file (preferably in Arial font).

The **cover letter** should include the corresponding author's full address and telephone/fax numbers and should be in an e-mail message sent to the Editor, with the file, whose name should begin with the first author's surname, as an attachment.

Article Types

Three types of manuscripts may be submitted:

Regular articles: These should describe new and carefully confirmed findings, and experimental procedures should be given in sufficient detail for others to verify the work. The length of a full paper should be the minimum required to describe and interpret the work clearly.

Short Communications: A Short Communication is suitable for recording the results of complete small investigations or giving details of new models or hypotheses, innovative methods, techniques or apparatus. The style of main sections need not conform to that of full-length papers. Short communications are 2 to 4 printed pages (about 6 to 12 manuscript pages) in length.

Reviews: Submissions of reviews and perspectives covering topics of current interest are welcome and encouraged. Reviews should be concise and no longer than 4-6 printed pages (about 12 to 18 manuscript pages). Reviews are also peer-reviewed.

Review Process

All manuscripts are reviewed by an editor and members of the Editorial Board or qualified outside reviewers. Authors cannot nominate reviewers. Only reviewers randomly selected from our database with specialization in the subject area will be contacted to evaluate the manuscripts. The process will be blind review.

Decisions will be made as rapidly as possible, and the journal strives to return reviewers' comments to authors as fast as possible. The editorial board will re-review manuscripts that are accepted pending revision. It is the goal of the IJPS to publish manuscripts within weeks after submission.

Regular articles

All portions of the manuscript must be typed double-spaced and all pages numbered starting from the title page.

The Title should be a brief phrase describing the contents of the paper. The Title Page should include the authors' full names and affiliations, the name of the corresponding author along with phone, fax and E-mail information. Present addresses of authors should appear as a footnote.

The Abstract should be informative and completely self-explanatory, briefly present the topic, state the scope of the experiments, indicate significant data, and point out major findings and conclusions. The Abstract should be 100 to 200 words in length.. Complete sentences, active verbs, and the third person should be used, and the abstract should be written in the past tense. Standard nomenclature should be used and abbreviations should be avoided. No literature should be cited.

Following the abstract, about 3 to 10 key words that will provide indexing references should be listed.

A list of non-standard **Abbreviations** should be added. In general, non-standard abbreviations should be used only when the full term is very long and used often. Each abbreviation should be spelled out and introduced in parentheses the first time it is used in the text. Only recommended SI units should be used. Authors should use the solidus presentation (mg/ml). Standard abbreviations (such as ATP and DNA) need not be defined.

The Introduction should provide a clear statement of the problem, the relevant literature on the subject, and the proposed approach or solution. It should be understandable to colleagues from a broad range of scientific disciplines.

Materials and methods should be complete enough to allow experiments to be reproduced. However, only truly new procedures should be described in detail; previously published procedures should be cited, and important modifications of published procedures should be mentioned briefly. Capitalize trade names and include the manufacturer's name and address. Subheadings should be used. Methods in general use need not be described in detail.

Results should be presented with clarity and precision. The results should be written in the past tense when describing findings in the authors' experiments. Previously published findings should be written in the present tense. Results should be explained, but largely without referring to the literature. Discussion, speculation and detailed interpretation of data should not be included in the Results but should be put into the Discussion section.

The Discussion should interpret the findings in view of the results obtained in this and in past studies on this topic. State the conclusions in a few sentences at the end of the paper. The Results and Discussion sections can include subheadings, and when appropriate, both sections can be combined.

The Acknowledgments of people, grants, funds, etc should be brief.

Tables should be kept to a minimum and be designed to be as simple as possible. Tables are to be typed double-spaced throughout, including headings and footnotes. Each table should be on a separate page, numbered consecutively in Arabic numerals and supplied with a heading and a legend. Tables should be self-explanatory without reference to the text. The details of the methods used in the experiments should preferably be described in the legend instead of in the text. The same data should not be presented in both table and graph form or repeated in the text.

Figure legends should be typed in numerical order on a separate sheet. Graphics should be prepared using applications capable of generating high resolution GIF, TIFF, JPEG or Powerpoint before pasting in the Microsoft Word manuscript file. Tables should be prepared in Microsoft Word. Use Arabic numerals to designate figures and upper case letters for their parts (Figure 1). Begin each legend with a title and include sufficient description so that the figure is understandable without reading the text of the manuscript. Information given in legends should not be repeated in the text.

References: In the text, a reference identified by means of an author‘s name should be followed by the date of the reference in parentheses. When there are more than two authors, only the first author‘s name should be mentioned, followed by ’et al‘. In the event that an author cited has had two or more works published during the same year, the reference, both in the text and in the reference list, should be identified by a lower case letter like ’a‘ and ’b‘ after the date to distinguish the works.

Examples:

Abayomi (2000), Agindotan et al. (2003), (Kelebeni, 1983), (Usman and Smith, 1992), (Chege, 1998; 1987a,b; Tijani, 1993,1995), (Kumasi et al., 2001)

References should be listed at the end of the paper in alphabetical order. Articles in preparation or articles submitted for publication, unpublished observations, personal communications, etc. should not be included in the reference list but should only be mentioned in the article text (e.g., A. Kingori, University of Nairobi, Kenya, personal communication). Journal names are abbreviated according to Chemical Abstracts. Authors are fully responsible for the accuracy of the references.

Examples:

Ogunseitan OA (1998). Protein method for investigating mercuric reductase gene expression in aquatic environments. Appl. Environ. Microbiol. 64:695-702.

Gueye M, Ndoye I, Dianda M, Danso SKA, Dreyfus B (1997). Active N2 fixation in several Faidherbia albida provenances. Ar. Soil Res. Rehabil. 11:63-70.

Charnley AK (1992). Mechanisms of fungal pathogenesis in insects with particular reference to locusts. In: Lomer CJ, Prior C (eds) Biological Controls of Locusts and Grasshoppers: Proceedings of an international workshop held at Cotonou, Benin. Oxford: CAB International, pp 181-190.

Mundree SG, Farrant JM (2000). Some physiological and molecular insights into the mechanisms of desiccation tolerance in the resurrection plant Xerophyta viscasa Baker. In Cherry et al. (eds) Plant tolerance to abiotic stresses in Agriculture: Role of Genetic Engineering, Kluwer Academic Publishers, Netherlands, pp 201-222.

Short Communications

Short Communications are limited to a maximum of two figures and one table. They should present a complete study that is more limited in scope than is found in full-length papers. The items of manuscript preparation listed above apply to Short Communications with the following differences: (1) Abstracts are limited to 100 words; (2) instead of a separate Materials and Methods section, experimental procedures may be incorporated into Figure Legends and Table footnotes; (3) Results and Discussion should be combined into a single section.

Proofs and Reprints: Electronic proofs will be sent (e-mail attachment) to the corresponding author as a PDF file. Page proofs are considered to be the final version of the manuscript. With the exception of typographical or minor clerical errors, no changes will be made in the manuscript at the proof stage.

International Journal of Physical Sciences

Table of Contents: Volume 8 Number 22 16 June, 2013

ARTICLES

PHYSICS

CHEMISTRY

ARTICLES

MATHEMATICS

APPLIED SCIENCE

academicJournals

Vol. 8(22), pp. 1193-1200, 16 June, 2013
DOI: 10.5897/IJPS2013.3878
ISSN 1992-1950 © 2013 Academic Journals
http://www.academicjournals.org/IJPS

International Journal of Physical Sciences

Full Length Research Paper

Photovoltaic solar cell simulation of shockley diode parameters in matlab

Awodugba, A. O.*, Sanusi, Y. K., and Ajayi, J. O.

Department of Pure and Applied Physics, Ladoke Akintola University of Technology, Ogbomoso, Nigeria.

Accepted 10 June, 2013

In this work, the Shockley diode parameters were simulated using the Matlab software package with the solar cell I - V and P - V characteristics in focus. Our model has been based on previous studies while the effects of varying cell temperature, series resistance, R_s ambient irradiation and diode quality factor were put into consideration and the output current and power characteristics of the PV model simulated, all for 10 iterations using the Newton - Raphson algorithm. The effect of shunt is neglected throughout the simulation while the results showed expected trends as reported by previous authors. This work therefore will be very useful for users, especially researchers in this field.

Key words: Photovoltaic, solar cell, Matlab, simulation, photocurrent.

INTRODUCTION

The quest for alternative energy sources and requirements in the next decades has attracted a lot of attention because there is a strong worldwide demand for energy, not to mention the fact that there is dwindling fossil-fuel reserves and global warming stemming from climate change that has resulted in various degrees of natural disaster like flooding, extreme heat /drought and rise in ocean levels.

One of the candidates to replace pollutant fossil-fuel energy sources and which is also inexhaustible is the solar energy which can be harvested using the solar cells, modules and arrays.

When exposed to light, photons with energy greater than the bandgap energy of the semiconductor are absorbed and create an electron-hole pair. These carriers are swept apart under the influence of the internal electric fields of the p-n junction and thus creating a photogenerated current proportional to the incident radiation.

In the dark, the I-V output characteristic of a solar cell has an exponential characteristic of a solar cell has an exponential characteristic similar to that of a diode. When the cell is short circuited, this current flows in the external circuit, and when open circuited, this current is shunted internally by the intrinsic p-n junction diode. The characteristics of this diode therefore set the open circuit voltage characteristics of the cell Geoff (2000).

In all solar power systems, efficient simulations including PV panel are required before any experimental verification is carried out. To this end, several authors (Akihiro, 2005; Ashish and Rakesh, 2011; Abdulkadir et al., 2012; Gonzalez-Longatt, 2010; 2005; Salmi et al 2012; Mohammed 2009; Gow and Manning; 1999) have carried out simulations aimed at harvesting greater amount of solar energy or simply to improve on the efficiency of the solar cell.

Also, Bourdoucen and Gastli (2007) developed an analytical model for PV panels and arrays based on extracted physical parameters of solar cells with an advantage of simplifying mathematical modelling of different cells and panel configurations without losing necessary accuracy of system operation.

This paper therefore focuses on the simulation of an improved model of the solar cell based on the Shockley

*Corresponding author. E-mail: aoawodugba@lautech.edu.ng.

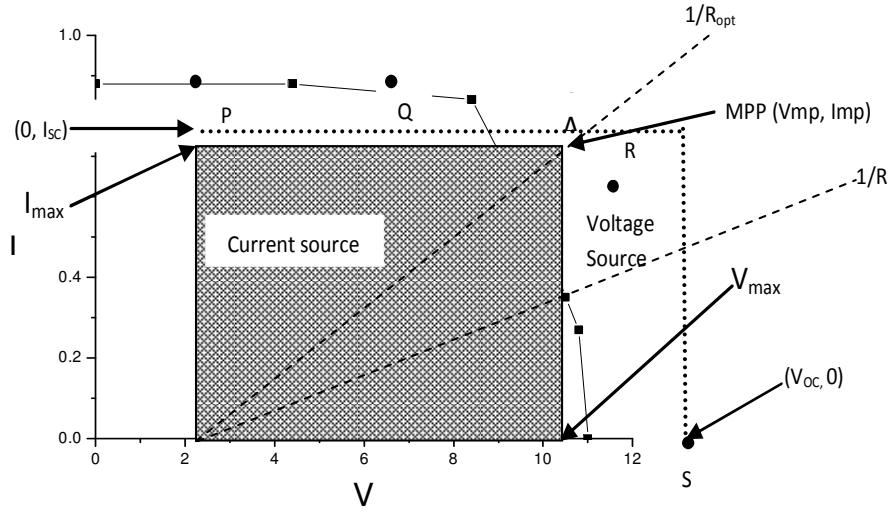

Figure 1. I - V Curve from the constructed and mounted module.

diode parameters using the Newton-Raphson algorithm in conjunction with Matlab software package.

METHODOLOGY

Mathematical formulation of the photovoltaic cell

The solar cell which is the basic unit of a photovoltaic module consists of a p-n junction fabricated in a thin wafer or layer of semiconductor. Though the electrical characteristics differ very little from a diode, it is represented by the Shockley Equation (1). In an ideal solar cell, $R_s = R_{sh} = 0$, a very relatively common assumption (Ramos et al., 2010). The Shockley equation is given as:

$$I_D = I_0\left(e^{\frac{V_C q}{nkT_{CK}}} - 1\right) \quad (1)$$

Where:
"I_D" is the dark current (A)
"I_0" is the saturation current of the diode (A)
"V_C" is a cell voltage (V)
"q" is the electronic charge ($1.6.10^{-19}$(Coul.)
"n" is the diode ideality constant
"k" is the Boltmann constant ($1.38.10^{-23}$J/K
"T_{CK}" is the cell temperature.
The net current "I" which is the difference between the photogenerated current (I_L) and the normal diode current

$$I = I_L - I_D \quad (2)$$

A simplified model [10] is given as:

$$I = I_L - I_0\left(e^{\frac{(V_C + IR_S)q}{nkT_{CK}}} - 1\right) \quad (3)$$

Where R_S is the series resistance in Ohms.

Equation (3) does not represent the I - V characteristics of a practical PV module, thus, inclusion of additional parameter R_{SH} (Shunt). Thus, Equation (3) becomes:

$$I = I_L - I_0\left(e^{\frac{(V_C + IR_S)q}{nkT_{CK}}} - 1\right) - \left(\frac{V_C + IR_S}{R_{SH}}\right) \quad (4)$$

The Series resistance R_S and the shunt R_{SH} are included in the real operation of the solar module to cater for the losses that exist in the cells and between the cells in the module. Thus, the simplest PV model of a solar cell is as shown in Figure 1.

$$I_L = I_L(T_1) + K_0(T - T_1) \quad (5)$$

$$I_L(T_1) = I_{SC}(T_{1,nom})\frac{G}{G_{nom}} \quad (6)$$

$$K_0 = \frac{I_{SC}(T_2) - I_{SC}(T_1)}{T_2 - T_1} \quad (7)$$

$$I_0 = I_0(T_1) \times \left[\frac{T}{T_1}\right]^{\frac{3}{n}} \times e^{\frac{qV_q(T_1)}{nk\left(\frac{1}{T} - \frac{1}{T_1}\right)}} \quad (8)$$

$$I_0(T_1) = \frac{I_{SC}(T_1)}{\left(e^{\frac{qV_{OC}(T_1)}{nkT_1}} - 1\right)} \quad (9)$$

$$R_S = -\frac{dV}{dI_{Voc}} - \frac{1}{X_V} \quad (10)$$

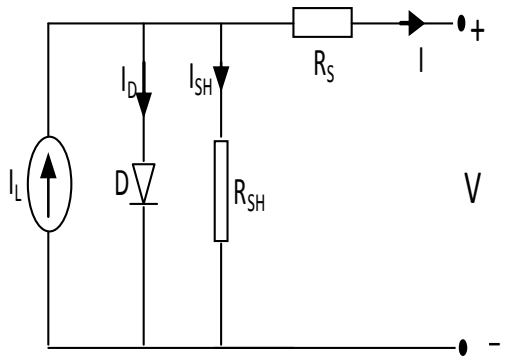

Figure 2. Single diode model of a solar cell.

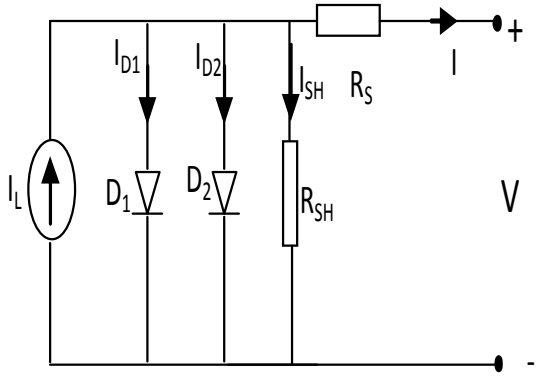

Figure 3. Double diode model of a solar cell.

$$X_V = I_o(T_1)\frac{q}{nkT_1}e^{\frac{qV_{OC}(T_1)}{nkT_1}} - \frac{1}{X_V} \quad (11)$$

In all these equations that is, (5) to (11), the shunt resistance has been neglected while all the constants can be determined by examining the manufacturers' ratings of the PV cell, and then the measured I - V curves of the module.

Important features of a Current – Voltage (I - V) Curve for a solar cell

The plot of current against voltage for a typical solar cell is shown in Figure 1.

1). Short-circuit current, $I_{SC.}$ This is the greatest value of the current generated by a cell and is produced when V = 0, the short circuit conditions.

2). Open circuit voltage, V_{OC}. This is the voltage drop across the diode (p-n junction) when photogenerated current, I_{ph} = 0, that is, at night when there is no illumination at all. This is represented mathematically as:

$$V_{OC} = \frac{nkT}{q}\ln\left[\frac{I_L}{I_O}\right] = V_t \ln\left[\frac{I_L}{I_O}\right] \quad (12)$$

Where $V_t = \left[\frac{mkT_C}{e}\right]$ is known as thermal voltage and T is the absolute cell temperature.

3). Maximum power point, A. This is the point (V_{max}, I_{max}) at which the power dissipated in theresistive load is maximum: $P_{max} = V_{max} I_{max}$.

4). Maximum efficiency, η. The ratio between the maximum power and the incident light power.

$$\eta = \frac{P_{max}}{P_{in}} = \frac{I_{max} V_{max}}{AG_a} \quad (13)$$

Where G_a is the ambient irradiation and A, is the cell area.

5). Fill factor, FF. The ratio of the maximum power that can be delivered to the load and the product of I_{SC} and V_{OC} .

$$FF = \frac{P_{max}}{V_{OC} I_{SC}} = \frac{I_{max} V_{max}}{V_{OC} I_{SC}} \quad (14)$$

The fill factor is a measure of the real I - V characteristic with a value higher than 0.7 connoting a good cell. This value diminishes as the cell temperature is increased.

It has also been established, Gonzalez-Longatt (2010) that for a resistive load, the load characteristic is a straight line with slope 1/V = 1/R. The power delivered to the load depends on the value of the resistance only. If this load R is small, the cell operates in the region P - Q of the curve where the cell behaves as a constant current source, almost equal to the short circuit current. On the other hand, if the load R is large, the cell operates on the region R – S of the curve where the cell behaves more as constant voltage source, almost equal to the open-circuit voltage, Hansen et al. (2000).

Modeling of the solar cell

Various models have been developed and utilized in order to study solar cell behavior. The simplest and the most widely used equivalent circuit of a solar cell is a current source in parallel with a diode as shown in Figure 2. The double diode equivalent circuit Nishioka et al. (2007) shown in Figure 3 has also been reported.

In this work the single diode model is adapted because of its simplicity to program using the Matlab package.

This model is based on the previous works (Geoff, 2000; Gonzalez – Longatt, 2005; Ramos et al., 2010; Akihiro, 2005; Savita et al., 2010).

All the authors used Matlab Software which requires 3 values to calculate the net operating current of the module. These are:

1). Va = Module operating voltage
2). G = [Suns] = Irradiance with 1 suns = 1000 W/m^2
3). TaC = Module temperature, in °C

The body of the program is divided in 4 main parts:

1). Definition of constants (Boltzmann's constant, k, electronic charge, q, diode –ideality quality factor, A, irradiance, G, etc
2). Definition of variables
3). Calculation of I_L, I_o and R_s (Equations 5 – 10 are used)
4). Calculation of I

Newton – Raphson iterative method is exploited in this work to solve the double –exponential Equation (4) because of its quick convergence. In this work, ten iterations were performed to reduce error. The algorithm of the adopted MPPT logic is shown in figure 4

while The Matlab script file used to generate the simulation results in this work are listed below:

```
function Itt = calcur (Vd,Suns,Temp)
%k = 2 + Temp;
% Given voltage, illumination and temperature
% Itt,Vd = array current, voltage
 % G = num of Suns (1 Sun = 1000 W/mˆ2)
% T = Temp in Deg C
k = 1.38e-23; % Boltzman's const
q = 1.60e-19; % charge on an electron
Voo = Va;
tr = 3.016;
cap = 10;
Iph = Voo / tr * exp(- 1/(tr * cap));
A = 1.2; % "diode quality" factor, =2 for crystaline, <2 for
amorphous
Vg = 1.12; % band gap voltage, 1.12eV for xtal Si, ˜1.75 for
amorphous Si.
Ns = 36; % number of series connected cells (diodes)
 T1 = 273 + 25;
Voc_T1 = 21.06 /Ns; % open cct voltage per cell at temperature T1
Isc_T1 = 3.80; % short cct current per cell at temp T1
T2 = 273 + 75;
disp(T2);
Voc_T2 = 17.05 /Ns; % open cct voltage per cell at temperature T2
Isc_T2 = 3.92; % short cct current per cell at temp T2
TaK = 273 + Temp; % array working temp
TrK = 273 + 25; % reference temp
% constant "a" can be determined from Isc vs T
Iph_T1 = Isc_T1 * Suns;
aa =Isc_T2 - Isc_T1;
 ab = Isc_T1 * 1/(T2 - T1);
a = aa/ab;
Vt_T1 = k * T1 / q; % = A * kT/q
 Ir_T1 = Isc_T1 / (exp(Voc_T1/(A*Vt_T1))-1);
Ir_T2 = Isc_T2 / (exp(Voc_T2/(A*Vt_T1))-1);
b = Vg * q/(A*k);
 rvl = exp(-b *(1/TaK - 1/T1);
 Ir = Ir_T1 * (TaK/T1).^(3/A) * rvl);
X2v = Ir_T1/(A*Vt_T1) * exp(Voc_T1/(A*Vt_T1));
dVdI_Voc = - 1.15/Ns / 2; % dV/dI at Voc per cell --
% from manufacturers graph
Rs = - dVdI_Voc - 1/X2v; % series resistance per cell
% Itt = 0:0.01:Iph;
Vt_Ta = A * 1.38e-23 * TaK / 1.60e-19; % = A * kT/q
% solve for Itt: f(Itt) = Iph - Itt - Ir.*( exp((Vc+Itt.*Rs)./Vt_Ta) -1) = 0;
% Newton's method: Itt2 = Itt1 - f(Itt1)/f'(Itt1)
Vc = Vd/Ns;
 Itt = zeros(size(Vc));
% Ittv = Itt;
for j=1:10;
Itt = Itt - (Iph - Itt - Ir.*( exp((Vc+Itt.*Rs)/Vt_Ta) -1))/ (-1 -
(Ir.*(exp((Vc+Itt.*Rs)./Vt_Ta) -1)).*Rs./Vt_Ta);
end.
```

RESULTS

1). Effect of varying cell temperature.
The effect of varying cell temperature at solar irradiance G = 1Suns on the open-circuit voltage V_{oc} and the short circuit current I_{sc} is shown in Figures 5 and 6.

2). Effect of varying series resistance, R_s
Figures 7 and 8 showed the effect of the variation of R_s, the series resistance on the slope angle of the I - V curves.

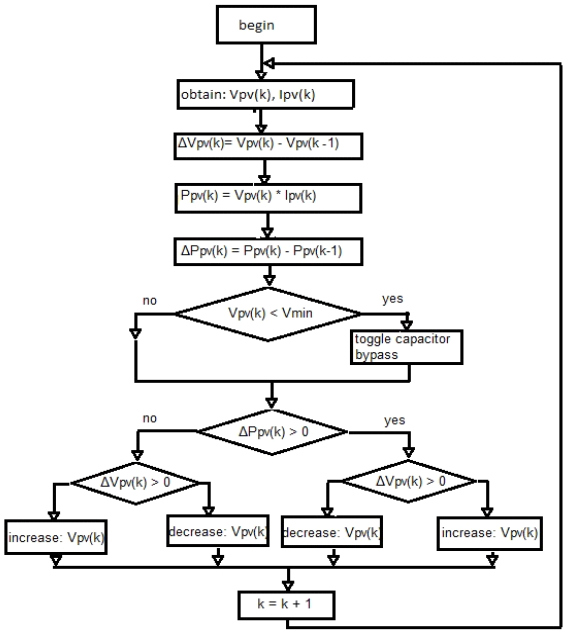

Figure 4. Algorithm of the adopted MPPT logic.

3). Effect of ambient irradiation
Figure 9 showed the effect of irradiance variation 0.2 – 1.5 Suns at constant temperature 25°C (Pandiarajan et al., 2011; Atlas and Sharaf, 2007; Kumari et al., 2012; Yushaizad, 2004).

4). Effect of diode quality factor
The response of I_{sc} and V_{oc} with the diode quality factor is shown in Figure 10.

DISCUSSION

With G = 1 Suns, the open circuit voltage V_{oc} dropped slightly with increasing cell temperature while the short circuit current, I_{SC} increased, the cell being thus less efficient. For instance, when the cell temperature is 24°C at an irradiance of G = 1 suns, the open circuit voltage is about 15.05 V. However, if the temperature is reduced to 0°C at the same irradiance, the open circuit voltage increased to 20.1 V. This behaviour is presented in Figures 5 and 6.

Also, the variation of R_s, the series resistance of the PV affected the slope angle of thel - V curves with the attendant deviation from the maximum power point as shown in Figures 7 and 8. This series resistance which is always very low, and some cases be neglected (Tsai et al., 2008; Savita et al., 2010), was included in this work so as to enable the model to be used for any given PV cell.

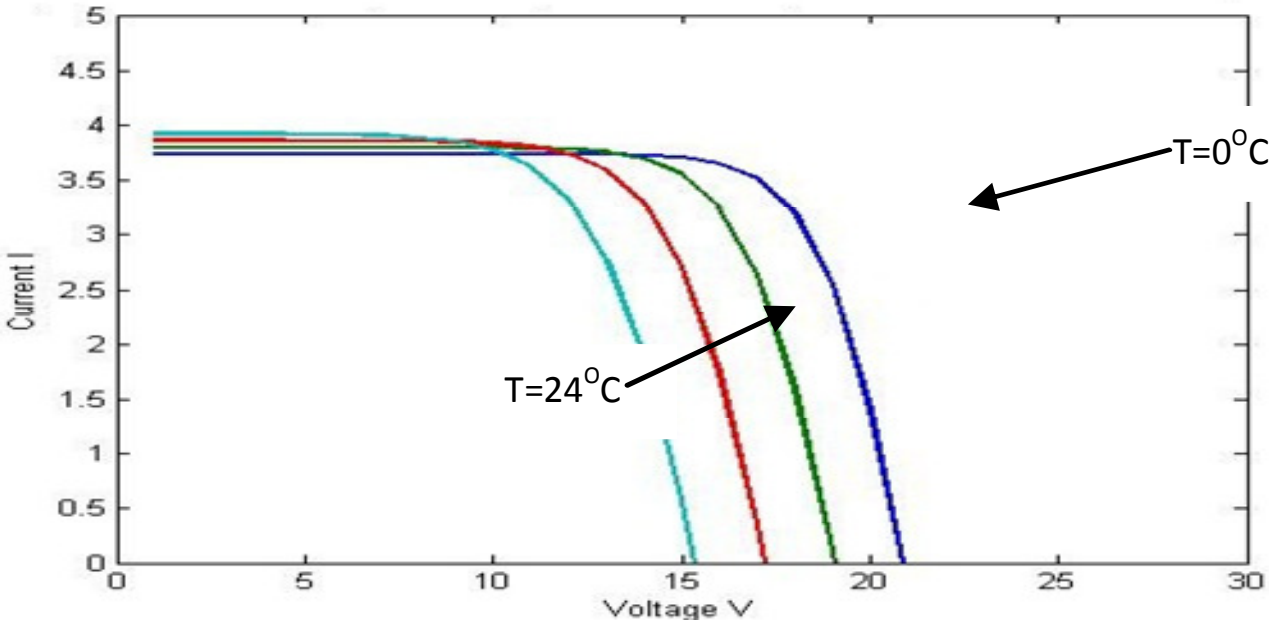

Figure 5. Module current against voltage at G= 1 Suns and at various temperature levels for zero bias.

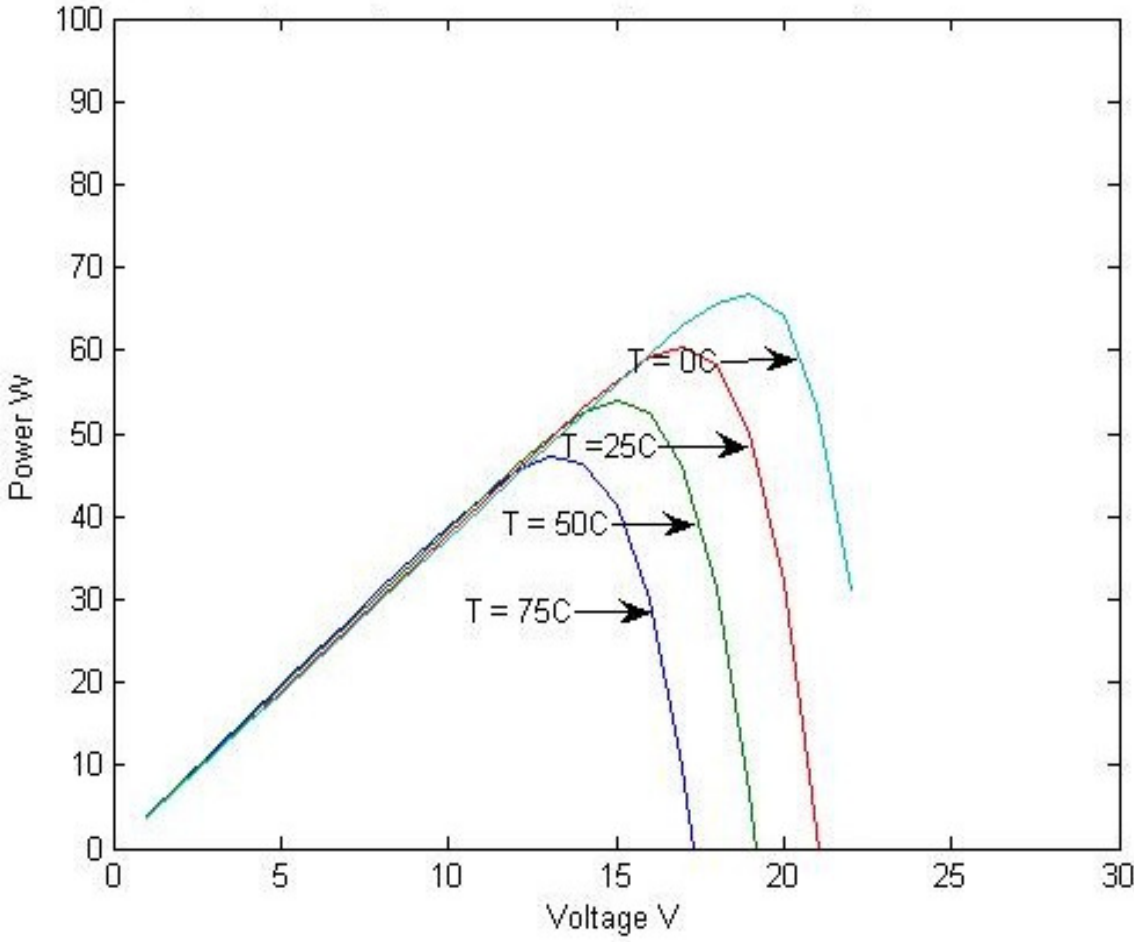

Figure 6. Power against module voltage at G = 1 Suns and at various temperature levels.

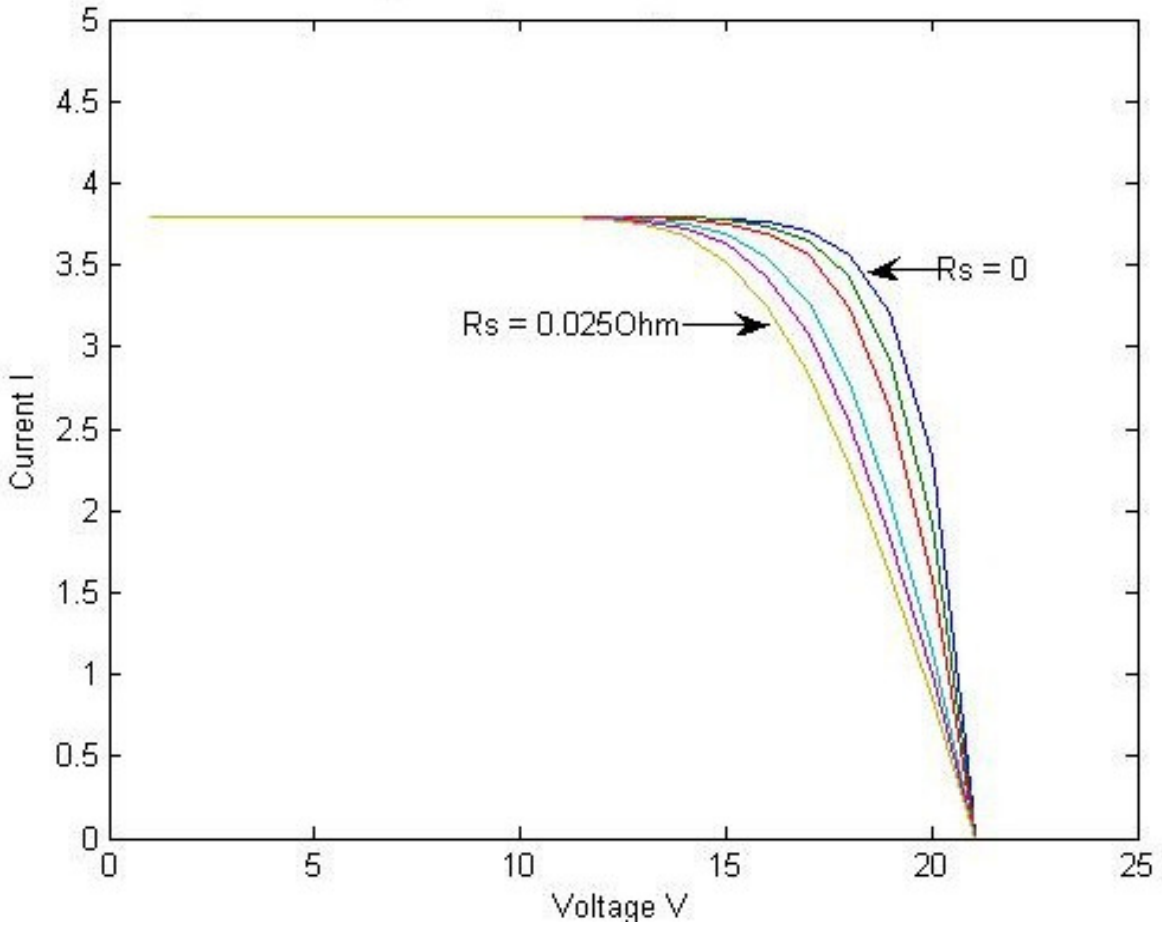

Figure 7. Graph of current against module voltage at G= 1 Suns and at various series resistance (Rs).

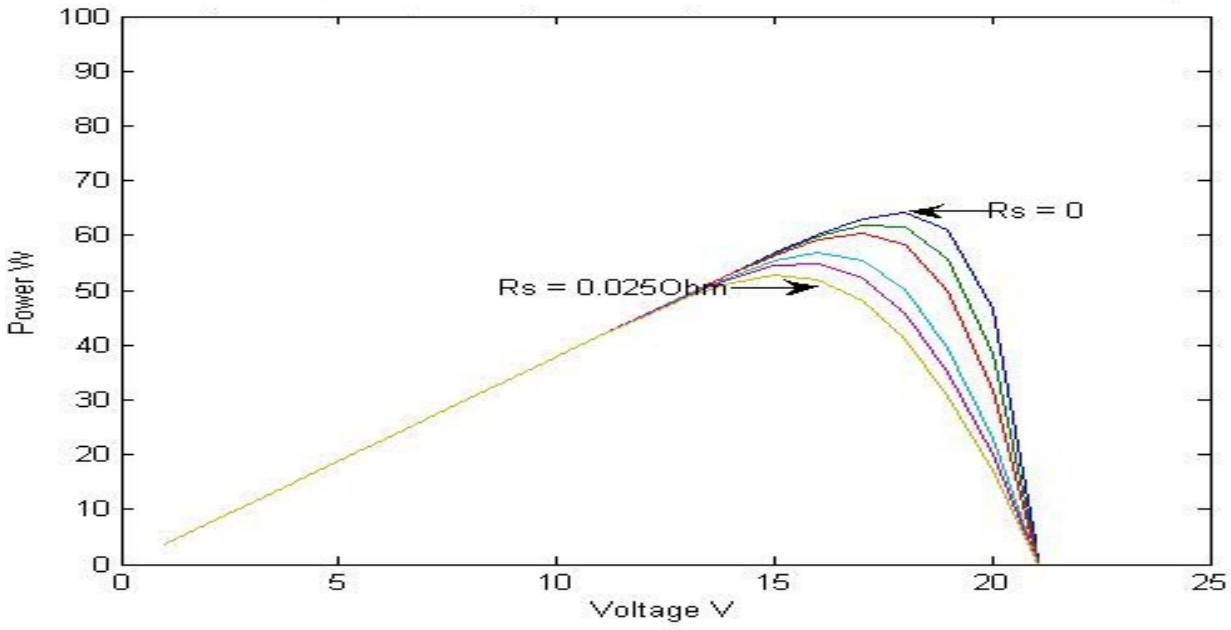

Figure 8. Power against module voltage at G = 1 Suns and at various series resistance, (Rs).

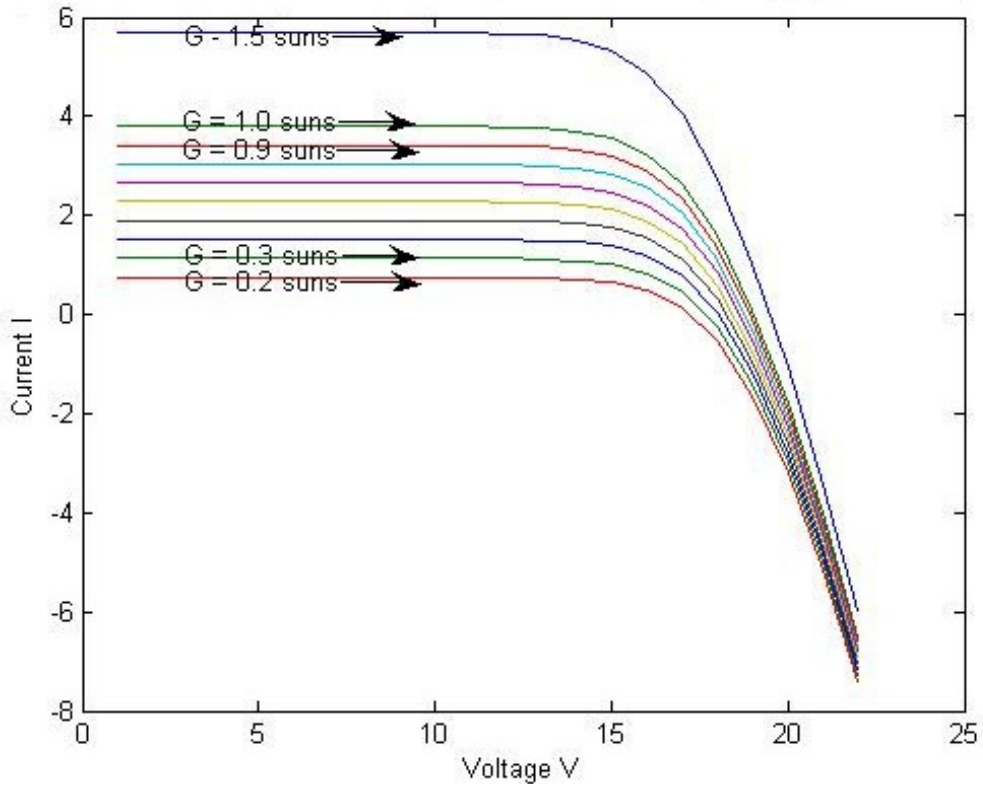

Figure 9. Module current against voltage at T = 25°C and at various irradiation levels.

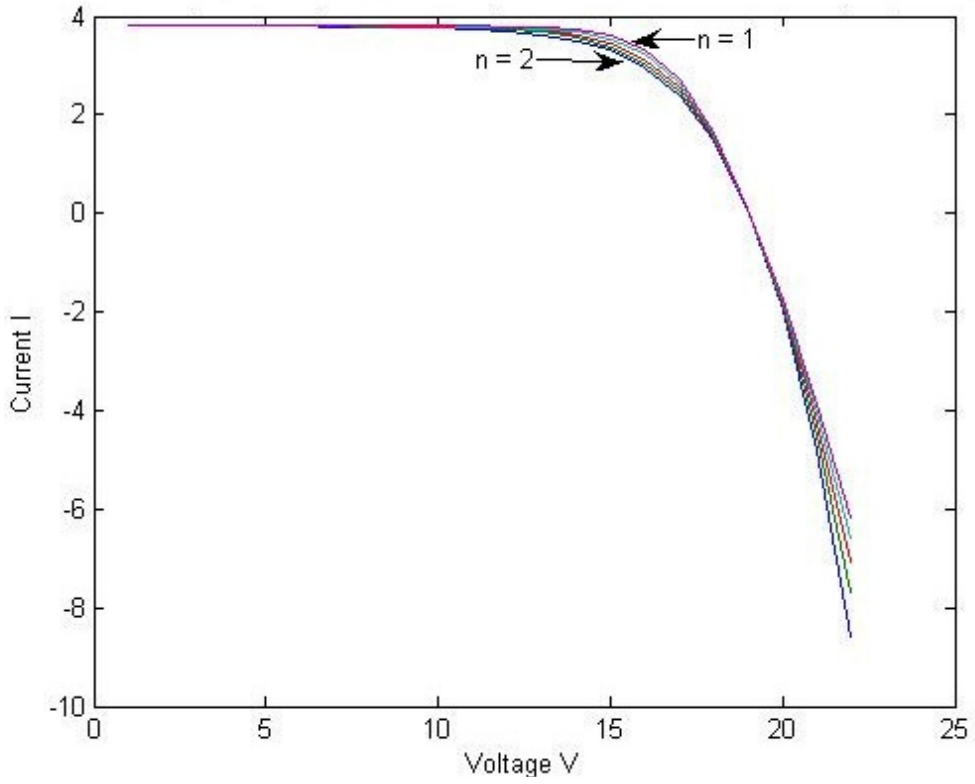

Figure 10. Module current against voltage at G = 1 Suns, 25°C with various diode quality factor values.

Figure 9 showed the effect of irradiance variation 0.2 – 1.5 Suns at constant temperature 25°C (Pandiarajan et al., 2011; Atlas and Sharaf, 2007; Yushaizad, 2004). The open circuit voltage, V_{oc} did not vary much as it is logarithmically dependent on the solar irradiance while the short circuit current is a linear function of the ambient irradiation since photocurrent depends on the irradiation. The higher the irradiation, the greater the current. It was also noted that reducing the irradiation will result in decreasing the output voltage of the panel.

As the diode quality factor is increased, the open circuit voltage of the cell increased. The ideal value of quality factor for solar cell is unity but its practical value for Silicon PV cell ranges between 1 and 2. Green (1992) states that diode quality factor takes a value between 1 and 2; being near 1 at high currents, rising towards 2 at low currents. This is demonstrated in Figure 10.

Conclusion

A Matlab simulation of PV solar cell using the Shockley diode circuit equations of a solar cell using the single diode equivalent circuit and taking into account the effects of physical and environmental parameters like cell temperature, series resistance, R_s , ambient irradiation and diode quality factor was carried out. The effect of shunt is however not considered. The results obtained followed the expected trends as reported by previous authors. This is the first step in the use of our results to model the I - V and P - V characteristics of a solar module deployed to take data in our location.

ACKNOWLEDGEMENT

One of the authors wishes to thank Mr Asonibare Oluwatosin for the MATLAB codes and implementation.

REFERENCES

Abdulkadir M, Samosir AS, Yatim AHM (2012). Modeling and simulation based approach of Photovoltaic system in Simulink Model APRN. J. Eng. Appl. Sci. 7(5):616-623.

Akihiro OI (2005). Doctoral Thesis. Design and simulation of photovoltaic water pumping system.

Ashish KS, Rakesh N (2011). PSIM and MATLAB based Simulation of PV Array for Enhance the Performance by using MPPT Algoirthm Int. J. Elect. Eng. 4(5):511-520.

Atlas IH, Sharaf AM (2007). A Photovoltaic Array Simulation Model for Matlab- Simulink GUI Environment. IEEE, Clean Electrical Power, International Conference on Clean Electrical Power (ICEP '07), June 14-16, Ischia, Italy.

Bourdoucen H, Gastli A (2007). Analytical Modeling and Simulation of Photovoltaic Panels and Arrays. J. Eng. Res. 4(1):75-81.

Gonzalez-Longatt FM (2005). "Model of Photovoltaic Module in MatlabTM", 2do congreso iberoamericano de estudiantes de ingeneria Electrica, electronica y Computacion (II CIBELEC).

Gonzalez-Longatt FM (2010). Model of Photovoltaic Module in MatlabTM", 2do congreso iberoamericano de estudiantes de ingeneria Electrica, electronica y Computacion (II CIBELEC).Spain. pp. 1-5.

Geoff W (2000). "Evaluating MPPT Converter Topologies using a MATLAB PV model" Australian Universities Power Engineering Conference, AUPEC '00, Brisbane.

Gow JA, Manning CD (1999). "Development of a photovoltaic array model for use in power electronic simulation studies," IEE Proc. Elect. Power Appl. 146(2):691-696.

Hansen A, Lars H, Bindner H (2000). "Models for a Stand-Alone PV System" Risø National Laboratory, Roskilde, December, ISBN 87 – 550-2776 – 8. [Online]. Available: http://www.risoe.dk/rispubl/VEA/ris-r-1219.htm

Kumari JS, Babu Ch. Sai H (2012). Mathematical Modeling and simulation of Photovoltaic Cell using Matlab_Simulink Environment. Int. J. Elect. Comput. Eng. 2(1):26-34.

Mohammed A (2009). Improved Circuit Model of Photovoltaic Array. Int. J. Elect. Power Energy Syst. Eng. 2:3.

Nishioka K, Nobuhiro S, Yakiharu U, Takashi F (2007). Analysis of multicrystalline silicon solar cells by modified 3-diode equivalent circuit model taking leakage current through periphery into consideration. Solar Energy Mater. Solar Cells. 91(13):1222-1227.

Pandiarajan N, Ramapragha R, Ranganath M (2011). Application of circuit model for Photovoltaic energy conversion system. Int. J. Adv. Eng. Technol. IJAPET. 2(4):118-127.

Ramos HJA, Campayo MJJ, Zamora BI, Larranaga LJ, Zulueta GE, Puelles PE (2010). Modelling of Photovoltaic Module In proceedings of the International Conference on Renewable Energies and Power Quality (ICREPQ'10) Granada Spain.

Salmi T, Bouzguenda M, Gastli A, Masmoudi A (2012). MATLAB/Simulink Based Modelling of Solar Photovoltaic Cell. Int. J. Renew. Energy Res. 2(2):213-217.

Savita N, Nema RK, Gayatri A (2010). "MATLAB/Simulink based study of photovolataic cells/modules/array and their experimental verification". Int. J. Energy Environ. 1(3):487-500.

Tsai HL, Tu CS, Su YJ (2008). Development of Generalized Photovoltaic Model Using MATLAB?SIMULINK Proceedings of the World Congress on Engineering and Computer Science 2008 WCECS, San Fransisco, USA. pp. 22-24.

Yushaizad Y (2004). Modeling and Simulation of maximum power point tracker for Photovoltaic System. National power and energy conference, proceedings, Kuala Lumpur, Malasia.

academicJournals

Vol. 8(22), pp. 1201-1208, 16 June, 2013
DOI: 10.5897/IJPS2013.3924
ISSN 1992-1950 © 2013 Academic Journals
http://www.academicjournals.org/IJPS

International Journal of Physical Sciences

Full Length Research Paper

Novel nano photocatalyst for the degradation of sky blue 5b textile dye

Zulfiqar Ali[1,2], Syed Tajammul Hussain[2], Muhammad Nawaz Chaudhry[1], Syeda Adila Batool[3], and Tariq Mahmood[2]*

[1]College of Earth and Environmental Sciences, University of the Punjab, Lahore, Pakistan.
[2]Nano Science and Catalysis Division, National Centre for Physics, Islamabad, Pakistan.
[3]Department of Space Science Punjab University Lahore, Pakistan.

Accepted 10 June, 2013

A new Nano photocatalyst, $CuO-Al_2O_3-ZrO_2-TiO_2$ was synthesized by co-precipitation for the removal of textile dye under ultra violet and direct sunlight. The synthesized catalyst was characterized by using X-rays diffraction, X-rays fluorescent, thermo gravimetric analysis, DRS, scanning electron microscopy and EDX. The dopants reduced the recombination of e_{cb}^- and h_{vb}^+ and decreased the band gap of TiO_2 from 3.25eV to 1.38eV. Due to this change, light absorption increased under sun light. The photocatalytic activity of the degraded samples of direct sky blue5B was analyzed by UV/Visible spectrophotometer. The results showed an enhanced photocatalytic activity under sun light about 96.8% in time duration of 100 min. It was also found that the degraded samples followed the pseudo first order kinetic model. This technique is cheap, easy and novel for the treatment of textile industrial waste water. In present energy crises of the world it can replace old expensive technologies.

Key words: Nano photocatalysis, direct sky blue5B, photocatalytic degradation, textile dyes, nano catalytic characterization.

INTRODUCTION

The extensive disposal of textile and other industrial waste water that contains organic dyes creates a severe contamination throughout the world. About 1 to 20% of the total dyes produced globally are lost during dyeing and other processes. These dyes are released into water as textile effluent (Weber and Stickney, 1993; Rafols and Barcelo, 1997; Houas et al., 2001; Kansal et al., 2009). These organic dyes weathered through oxidation; hydrolysis and other chemical reactions taking place in the wastewater phase can produce toxic metabolites (Bianco-Prevot et al., 2001; Neppolian et al., 2002; Pagga and Brown, 1986; Saquib and Muneer, 2003). These products produce unfavorable effects on human and animal health (Davydov et al., 2001) which requires a suitable treatment of wastewater for environmental contamination prevention. After the development of novel heterogeneous photocatalytic, oxidation process in the 1970s is of special interest particularly under solar irradiation (Malato et al., 2002). In these processes hydroxyl radicals ($OH^{\cdot}$) and superoxide anion ($O_2^{\cdot-}$), are produced due to absorption of radiation by semiconductor catalyst in contact with water and oxygen (Herrmann, 1999). Amongst a variety of catalysts, semiconductor photocatalyst containing titanium dioxide (TiO_2) is widely used due to its strong oxidizing power, non-toxicity and long-term photo stability (Pirkanniemi and Sillanpaa, 2002).

On the other hand, the photocatalytic efficiency of TiO_2 regarding the degradation of dyes reduces significantly due to the high recombination ratio of photo-induced

*Corresponding author. E-mail: tariqm20002000@yahool.com. Tel: +92-333-5178543, Fax: +92-512077395.

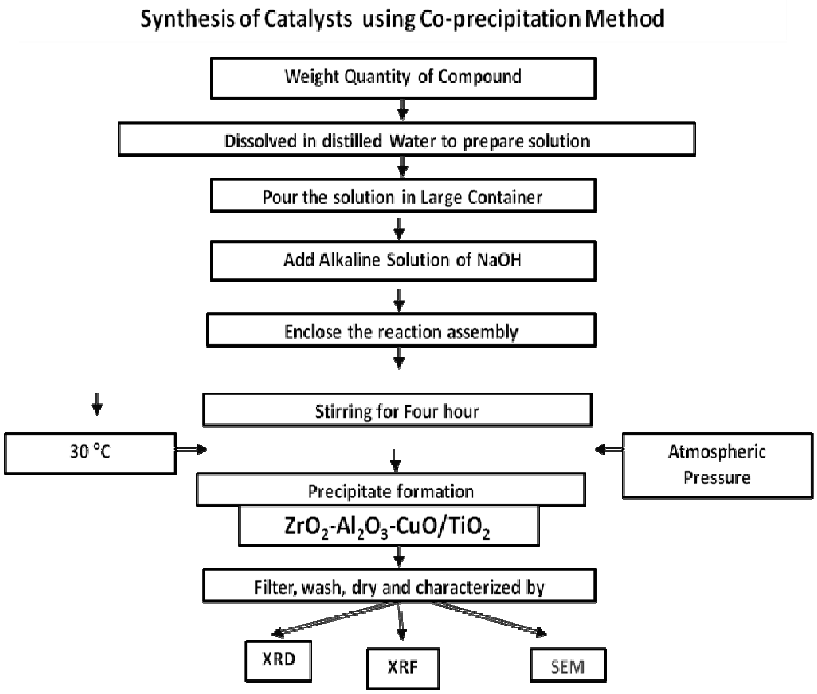

Figure 1. Summary of synthesis of photocatalyst Cuo-Zro_2-Al_2O_3-TiO_2.

electrons (e^-) and holes (h^+), which are produced due to irradiation under ultraviolet (UV) light (Bao et al., 2004; Malato et al., 2003). For TiO_2 the ideal wavelength regarding the band-gap energy is of 3.2 eV, which is at near-ultraviolet radiation (300nm) (Adewuyi, 2005; Meena and Pachwarya, 2009; Poulios and Aetopoulou, 2013). Thus the industrial efficacy of this process is bound to limited applications due to the need of ultra violet excitation energy source. As the solar light contains only 5% UV spectrum, hence further research in future is needed for the development of TiO_2 materials which is able to capture more amount of solar energy spectrum (Sonawane et al., 2004). Therefore the development of solar light active modified TiO_2 photo-catalyst with high catalytic efficiency in the visible region for the treatment of waste water is always of great interest and demand in both academic and commercial sectors. This paper aims at organic dyes degradation in wastewater treatment by modified TiO_2 photocatalytic systems. In particular, it focuses on enhancing the degradation efficiency of textile dyes by the use of visible light region, and improving the retrieval and reuse of TiO_2 photo-catalysts.

MATERIALS AND METHODS

TiO_2 (Degussa 25) was purchased from Sigma-Aldrich. Copper Nitrate, Zirconium Nitrate and Aluminum Nitrate (99.9% pure) were purchased from Merck Germany. The dye direct sky blue5B was purchased from Sigma-Aldrich. These chemicals were AR grade and there was no need of further purification before use.

The catalyst was prepared by a facile co-precipitation method as shown in Figure 1. CuO-ZrO_2-Al_2O_3-TiO_2 composite was synthesized by co-precipitation sedimentation method using ammonium carbonate as precipitating agent (Adewuyi, 2005). In this synthesis, the appropriate amount of TiO_2 (70 g) was suspended in 500 cm^3 of deionized water and homogenized for 30 min by stirring. Then equimolar copper nitrate, zirconium nitrate and aluminum nitrate each 10 g were mixed and dissolved in 100 cm^3 deionized water. The solution was homogenized by standard method. The mixture of these nitrates was then slowly mixed with TiO_2 solution and homogenized. The suspension, was precipitated against drop wise addition of $(NH_4)_2CO_3$. The precipitate was then dried overnight with continuous stirring at room temperature. The resultant precipitate was then washed and filtered until the pH of the solution reached near 7 and then dried at 100°C overnight. It was then calcinated at 400°C for 4 h in Muffle furnace. The resultant material was grinded and sieved. The prepared sample was characterized by XRD, SEM (Mahmood, 2011), XRF, EDX, TGA and RBS.

The band gap of synthesized catalyst was found by UV/Vis/NIR Spectrometer Lambda 950 diffused reflectance spectroscopy. The Powder XRD of the catalyst was investigated by using Scintag XDS 2000 diffractometer with Cu Kα radiation source. The XRD analysis was performed from 0° to 90° (2θ) for the confirmation of structure and crystalline phases. By applying Scherer's equation, the crystallite size was evaluated. For the investigation of morphology of synthesized catalyst, Scanning Electron Microscope (JEOL, JSM 6490-A) was used. The X-Ray fluorescence (JEOL, Model JSX 3202M)) was used for the elemental analysis. The TGA was performed by Perkin Elmer Diamond Series, USA. The photo-degradation of the solution of dye direct sky blue5B was investigated by UV/Vis Spectrometer (Perkin Elmer Lambda 25).

The solution containing different concentration of dye and dosage of catalyst was exposed to UV and solar irradiation. The experimental setup under solar light is shown in Figure 2. The dye

Figure 2. Photocatalytic degradation of direct sky blue5B dye experimental set up.

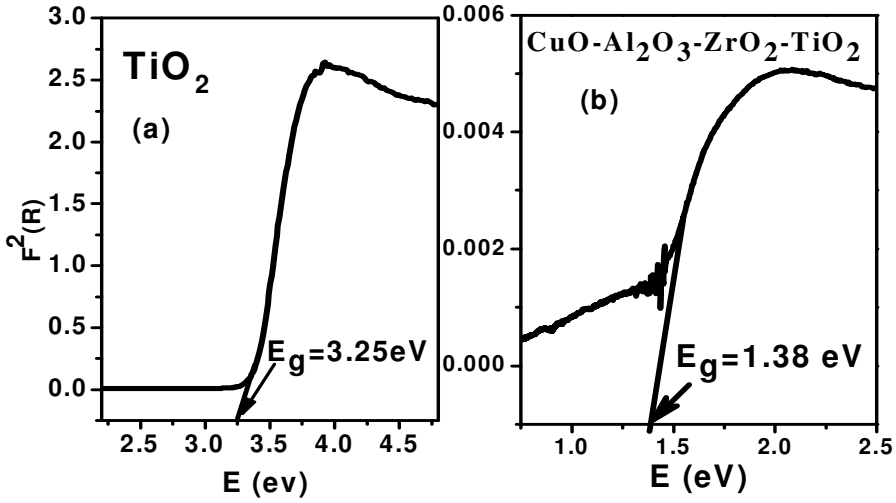

Figure 3. Band gap of TiO_2 and $CuO\text{-}ZrO_2\text{-}Al_2O_3\text{-}TiO_2$ nano composite.

solution was taken in a beaker with a magnetic stirrer for stirring and was exposed to the solar irradiation. 4 mirrors were used for focusing the sunlight to enhance the intensity of light. The degraded sample solution of 5 ml was taken after each 10 min interval up to 100 min. After filtering the sample solution, analyzed by UV/V is spectrometer. The removal percent of the dye direct sky blue5B samples were calculated by applying the formula:

$$\text{Degradation/Decolonization (\%)} = (C_t\text{-}C_o) / C_o \times 100 = (A_t\text{-}A_o) / A_o \times 100$$

Where C_o and C_t are the concentrations while A_o and A_t are the absorbance values of the dye solution before and after the exposure to sunlight respectively.

RESULTS AND DISCUSSION

The band gap of the synthesized powder was evaluated by UV-Visible Diffuse Reflectance Spectroscopy (DRS) in the solid phase. The band gap analysis plots of Kubelka-Munk function versus energy for TiO_2 and the synthesized sample is shown in Figure 3. The band gap of TiO_2 is 3.25 eV which shows its anatase character. When TiO_2 is modified by $CuO\text{-}Al_2O_3\text{-}ZrO_2$ its band gap is decreased from 3.25 eV to 1.38 eV which is clear in Figure 3.

The shifting of the band gap from higher to lower wavelength is probably due to enhanced d-d and charge transfer transitions in the solid phase.

A comparison of XRD pattern of the synthesized composite photocatalyst is presented in Figure 4, where it can be observed that the reflections arising from TiO_2 are dominant in the XRD pattern composite. The XRD patterns were matched with the standard pattern for the TiO_2 (JCPDS - 71-1168). The reflections at 25.195°, 47.772°, 53.704°, 54.851° and 62.521° represent TiO_2

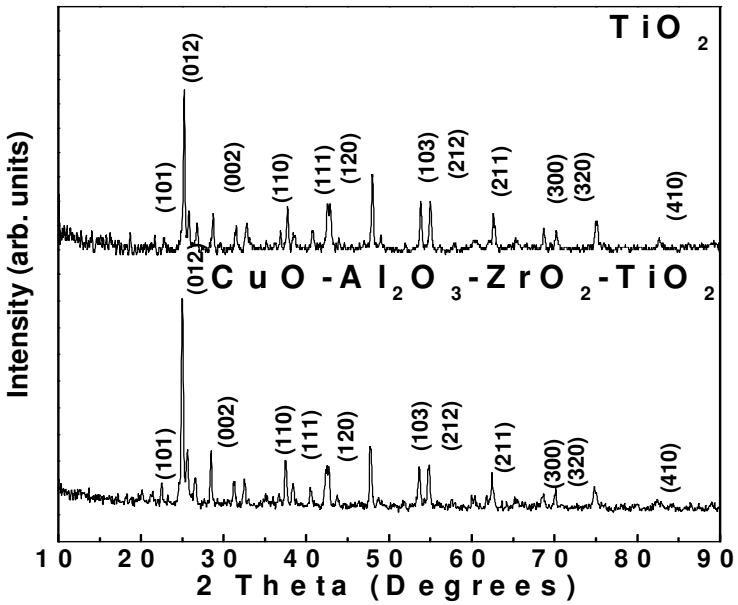

Figure 4. XRD Spectrum of TiO_2 and CuO-ZrO_2-Al_2O_3-TiO_2 nano composite.

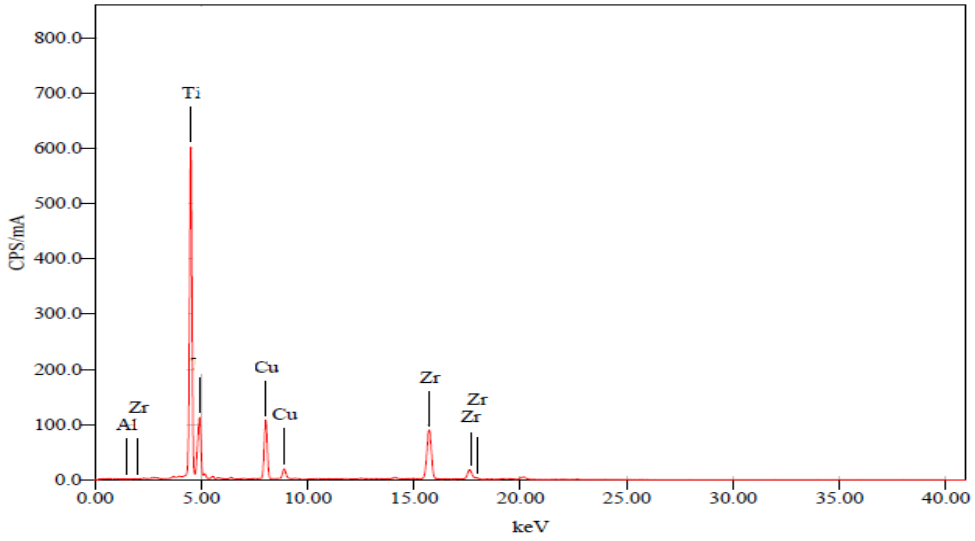

Figure 5. XRF peaks of photocatalyst CuO-Al_2O_3-ZrO_2-TiO_2.

(JCPDS -71 - 1168) whereas the reflections at 26.634°, 32.281° and 74.398° confirmed the presence of CuO phase (JCPDS - 34 - 1354). Similarly, the reflections at 2θ positions of 35.190° and 67.883° were matched with the Al_2O_3 (JCPDS - 34 - 0493). Low intensity peaks at the 2θ positions of 38.362°, 60.05° and 70.369° were identical with the standard pattern of ZrO_2 (JCPDS - 17 - 0385). The average crystallite sizes as calculated by Scherrer's equation using FWHM values of most intense peaks, was 29 nm.

The elemental composition of the synthesized sample CuO-Al_2O_3-ZrO_2/TiO_2 was confirmed by the X-ray Fluorescence analysis shown in Figure 5. It is found that all elements of the prepared catalyst were present and the major peak of TiO_2 shows that it is present as a base element in the catalyst. It is also confirmed from the analysis that no other peak rather than these elements is present in the catalyst, which shows its purity.

The thermo gravimetric analysis curve shows the weight loss against temperature rise as shown in Figure 6.

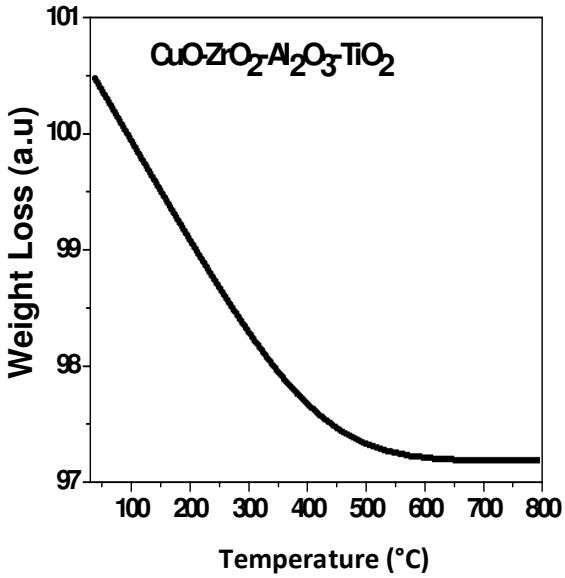

Figure 6. TGA of Photocatalyst (CuO-Al_2O_3-ZrO_2-TiO_2).

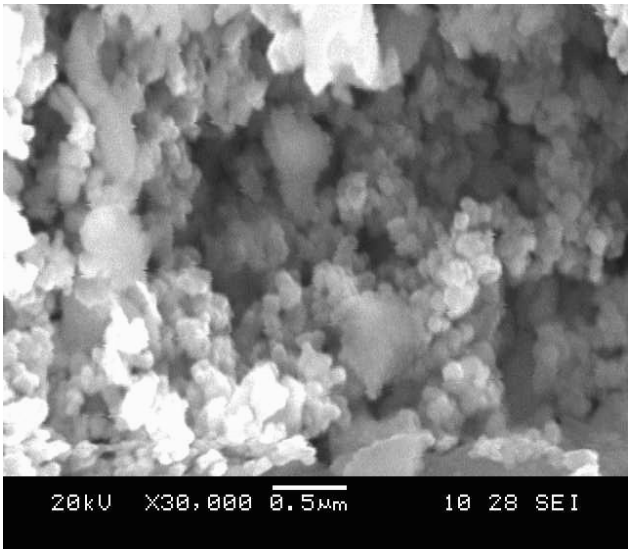

Figure 7. SEM of Photocatalyst (CuO-Al_2O_3-ZrO_2-TiO_2).

It was observed in the TGA curve of synthesized catalyst CuO-Al_2O_3-ZrO_2-TiO_2, there was a slight weight loss of about 2.49% in the temperature range of 100°C to 600°C, which corresponds to the removal of adsorbed water from the catalyst. The weight loss from 600 to 800°C is about 0.134% which shows that the catalyst is thermally stable and suitable for photo degradation investigation.

The morphology of synthesized catalyst CuO-Al_2O_3-ZrO_2-TiO_2 was evaluated by SEM as presented in Figure 7. The porous nano-aggregates can be clearly seen in micrograph. It was observed that the metal loading, in the form of oxides, have no significant effect on the

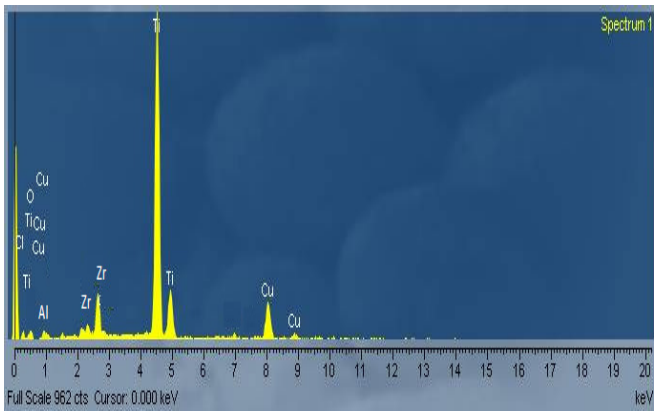

Figure 8. EDX peaks of Photocatalyst (CuO-Al_2O_3-ZrO_2-TiO_2).

morphology of TiO_2, however a meek increase in the particle size is observed due to doping which is in accordance with XRD graph. Metal oxides can amend the surface of the catalyst by increasing the dispersion of active site. The sample composition is determined by the energy dispersive X-ray utility of SEM. The compositions obtained by EDX (Figure 8) and XRF (Figure 5) were in accordance with the theoretical values and within the limits of experimental errors.

The proficient degradation by a photocatalyst in aqueous medium depends upon its ability of absorbing light and its less rate of recombination of electron-hole pair. This ability promotes the generation of oxidizing hydroxyl ($OH^{\bullet}$) radicals that requires suitable band gap energy compared to that of incident photons. To enhance the generation of hydroxyl radicals is dependent on charge carrier recombination rate. The drawback of TiO_2 is that it has high recombination rate suffers, as the life time of excited states is of the order of 10^{-9} to 10^{-12} s, which in turns suppresses the formation of oxidizing species (Hoffmann et al., 1995). The other drawback is that, it has a wide band gap of 3.2eV, which lies in near-UV radiation (300 nm) (Adewuyi, 2005). This reduces its ability to absorb the photons in the visible spectrum that is, $E_{photon} \leq 380$ nm limits its use in the sunlight having major portion above 380 nm. The matter of recombination inhibition and light harvesting in the visible region can be made effective through the modification of the surface of TiO_2 by composite formation. This will induce the charge separation through the interfacial charge transfer between the allowed energy states. The possible mechanisms of recombination inhibition through mutual charge transfer between the interfacial energy states of the base material, TiO_2 and the components of the synthesized composites that is, CuO, Al_2O_3 and ZrO_2.

It is clear in Figure 9a that, when 100ppm solution of the dye was irradiated by a UV source (8 W lamp) by using TiO_2 (5 mg/L) as a catalyst, the degradation rate was about 65%, but under the same concentration of dye and catalyst under solar irradiation, the degradation rate

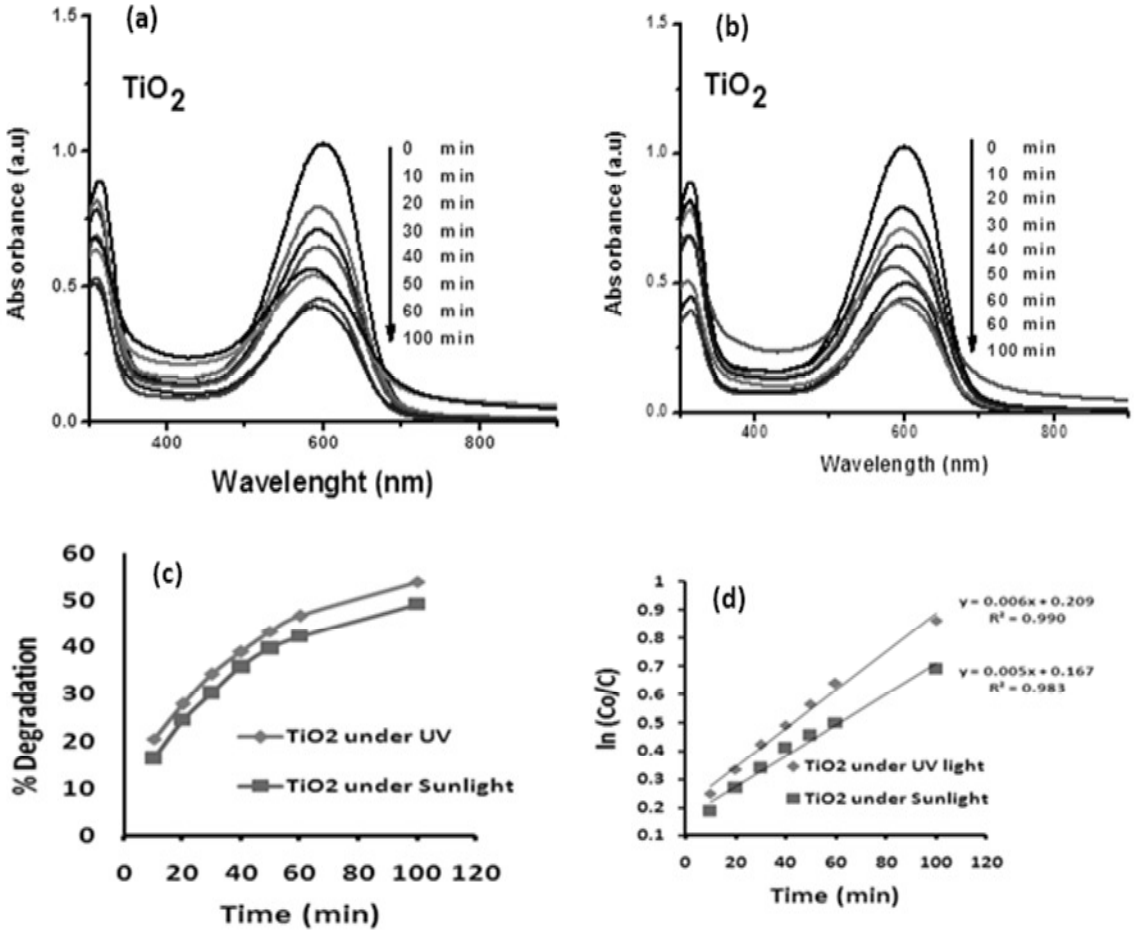

Figure 9. Graphical presentation of TiO_2 based degradation of Textile dye (Direct sky blue5B Dye).

Table 1. Comparisons between degradation rates of Direct sky blue5B Dye by TiO_2 and synthesized novel nano catalyst (CuO-Al_2O_3-ZrO_2-TiO_2) under UV & Sunlight.

Catalyst	Degradation rate (%) under UV light (100 min)	Degradation rate (%) under solar light (100 min)
TiO_2	65	58
CuO-Al_2O_3- ZrO_2-TiO_2	82.1	96.8

decreases by 58% (Figure 9b). This is due to the fact that the band gap of TiO_2 (3.2 eV) lies in the UV region (Table. 1).

It is clear from Table 1, the degradation rate of TiO_2 is 65% under UV light for 100 min duration, but the degradation rate of TiO_2 is 58% for the same duration of time. The less degradation rate under sunlight is due to band gap of TiO_2 (3.25 eV) which lies in the UV region. But when the TiO_2 is modified by CuO-Al_2O_3-ZrO_2 the band gap was reduced from 3.25 eV to 1.38 eV, which lies in the visible spectrum. From the result in Table 1, it is clear that the catalytic degradation efficiency enhanced up to 96.8% under solar irradiation, rather than 82.1% under UV light (8W lamp) (Figure. 10).

The comparison of degradation profiles of direct sky blue5B in the presence of TiO_2 and the synthesized catalyst CuO-Al_2O_3-ZrO_2-TiO_2 shows that as the dye direct sky blue5B is an azo dye with two absorption bands at λ = 598 nm and λ = 313 nm. The high intensity band with λ_{max} = 598 nm wraps a region of 700 - 500 nm while the low intensity band at λ_{max} = 313 nm covers a region of 370 - 260 nm. The slow response of TiO_2 under solar irradiation is mainly due to its ability to utilize only 5% of solar spectrum ability with additional hindrance due to the low intensity band of dye in 370 - 260 nm, which absorbs a significant number of photons making theses

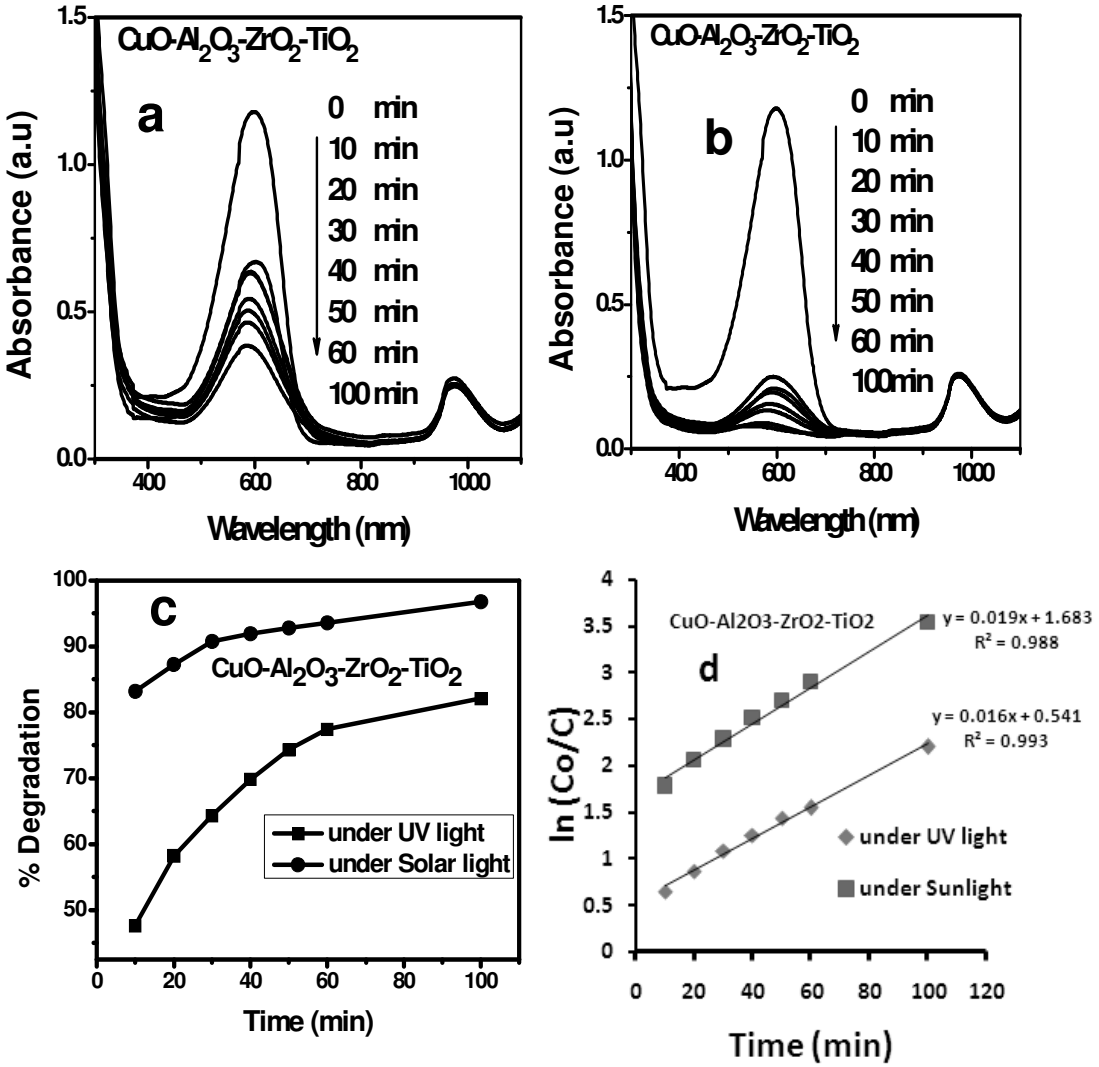

Figure 10. Graphical presentation of nano photocatalyst ($CuO-Al_2O_3-ZrO_2-TiO_2$) based degradation of textile dye (direct sky blue 5B dye).

inaccessible to TiO_2 thus causing a significant decrease in the degrading ability. As presented in Figure 9d, the kinetics of dye removal both in UV and under sunlight irradiation was evaluated by plotting ln (Co/C) against time. It is clear from the plots, the degradation of direct sky blue5B follows the pseudo-first order kinetics and the degradation rate depends on the concentration of dye with time.

Conclusion

From this study it is concluded that photocatalytic activity of TiO_2 can be enhanced by its suitable modification of the absorbing surface. However the best possible efficiency of the multiple photocatalyst can be obtained by selecting a suitable modifier with well-matched structure, morphological phase and chemical characteristics. It is also possible the photon initiated interfacial electron transfer between the allowed states of the semiconductors involved in the modified catalyst. Analysis of the synthesized catalyst pointed out that the dopants are very well dispersed in the anatase TiO_2. Optical properties enhancement, greater surface area and high quantum efficiency resulted due to adopted methodology TiO_2 modification. The highly efficient $CuO-Al_2O_3-ZrO_2-TiO_2$ nanoparticles of photocatalyst have extraordinary high activity in the degradation of direct sky blue5B under visible light irradiation. The use of visible light receptive nano photocatalysts are appropriate novel technique for the degradation of toxic organic pollutants and a cost effective way by using sunlight which is free of cost. Among other appropriate visible light active photocatalysts, CuO based systems are found to be a

better choice for the modification of TiO_2 along with Al_2O_3 and ZrO_2. Nano photocatalysts, due to their low-price, simple synthesis process, high stability, high activity towards photo-induced redox reactions and reducing power are the best choice for degradation of environmental pollutants.

ACKNOWLEDGEMENTS

Author would like to acknowledge and extend his heartfelt gratitude to the persons who helped me for this research work. I also acknowledge Nanoscience and Catalysis Division, National Centre for Physics, Quaid-i-Azam University Islamabad, for providing me technical and analytical facilities.

ABBREVIATIONS

XRD, X-Rays Diffraction; **XRF,** X-Rays Fluorescent; **TGA,** Thermo Gravimetric Analysis; **DRS,** Diffuse Reflectance Spectroscopy; **SEM,** Scanning Electron Microscope; **EDX,** Energy-Dispersive X-Ray Spectroscopy; **RBS,** Rutherford Back Scattering Ultra-Violet/Visible/Near-Infra Red Spectrophotometer) UV/Vis/NIR.

REFERENCES

Adewuyi YG (2005). Sonochemistry in environmental remediation 2. Heterogeneous sonophotocatalytic oxidation process for the treatment of pollutants in water. Environ. Sci. Technol. 39(22):8557–8570.

Bao N, Feng X, Yang Z, Shen L, Lu X (2004). Highly efficient liquid-phase photooxidation of an azo dye methyl orange over novel nanostructured porous titanate-based fiber of self-supported radially aligned $H_2Ti_8O_{17}$ x $1.5H_2O$ nanorods.Environ. Sci. Technol. 38(9):2729-36.

Bianco-Prevot AB, Baiocchi C, Brussino MC, Pramauro E, Savarino P, Augugliaro V, Marcì G, Palmisano L (2001). Photocatalytic degradation of acid blue 80 in aqueous solutions containing TiO_2 suspensions. Environ. Sci. Technol. 35(5):971-976.

Davydov L, Reddy EP, France P, Smirniotis PG (2001). Sonophotocatalytic destruction of organic contaminants in aqueous systems on TiO_2 powders, Appl. Catal. B: Environ. 32(1):95-105(11).

Herrmann JM (1999). Heterogeneous photocatalysis: fundamentals and applications to the removal of various types of aqueous pollutants, Catal. Today 53:115–129.

Hoffmann MR, Martin ST, Choi W, Bahemannt DW (1995). Environmental Applications of Semiconductor Photocatalysis, Chem. Rev. 95(1):69-96.

Houas A, Lachheb H, Ksibi M, Elaloiu E, Guillard C, Herrmann JM (2001). Photocatalytic degradation pathway of methylene blue in water, Appl. Catal. B: Environ. 31:145-157.

Kansal SK, Kaur N, Sing S (2009). Photocatalytic degradation of commercial reactive dyes in aqueous phase using Nanophotocatalysts, Nanoscale Res. Lett. 4:709-716.

Mahmood T (2011). Metallic Phytoremediation and Nanobiotechnology of water hyacinth, PhD Thesis, Department of Biochemistry, Quid-i-Azam University Islamabad Pakistan.

Malato S, Blanco J, Caceres J, Fernandez AR, Aguera A, Rodriguez A (2002). Photocatalytic treatment of water soluble pesticides by photo-Fenton and TiO_2 using solar energy. Catalysis Today 76(2):209-220. ISSN 0920-5861.

Malato S, Blanco J, Campos A, Ca´eres J, Guillard C, Herrmann JM, Ferna´dez-Alba AR (2003). Effect of operating parameters on the testing of new industrial titania catalysts at solar pilot plant scale, Appl. Catal. B: Environ. 42(4):349–357.

Meena RC, Pachwarya RB (2009). Photo catalytic degradation of model textile azo dyes in textile wastewater using methylene blue immobilized resin dowex-11, J. Sci. Ind. Res. 68:730-734.

Neppolian B, Choi HC, Sakthivel S, Arabindoo B, Murugesan V (2002). Solar light induced and TiO_2 assisted degradation of textile dye reactive blue 4, Chemosphere, 46(8): 1173–1181.

Pagga U, Brown D (1986).The degradation of dyestuffs: Part II Behaviour of dyestuffs in aerobic biodegradation tests, Chemosphere 15(4):479–491.

Pirkanniemi K, Sillanpaa M (2002). Heterogeneous water phase catalysis as an environmental application: a review,Chemosphere, 48(10):1047–1060.

Poulios I, Aetopoulou I (2013). Photocatalytic degradation of the textile dye reactive Orange 16 in the presence of TiO_2 suspensions, Environ. Technol. 20:479-487.

Rafols C, Barcelo D (1997). Determination of mono- and disulphonated azo dyes by liquid chromatography–atmospheric pressure ionization mass spectrometry, J. Chromatogr. A. 777(1): 177–192.

Saquib M, Muneer M (2003). TiO_2-mediated photocatalytic degradation of a triphenylmethane dye (gentian violet), in aqueous suspensions, Dyes Pigments, 56(1):37–49.

Sonawane RS, Kale BB, Dongare MK (2004). Preparation and photo-catalytic activity of $FeTiO_2$ thin films prepared by sol–gel dip coating, Mater. Chem. Phys. 85(1):52–57.

Weber EJ, Stickney VC (1993). Hydrolysis kinetics of Reactive Blue 19-Vinyl Sulfone, Water Res. 27(1):63–67.

academicJournals

Vol. 8(22), pp. 1209-1217, 16 June, 2013
DOI: 10.5897/IJPS12.576
ISSN 1992-1950 © 2013 Academic Journals
http://www.academicjournals.org/IJPS

International Journal of Physical Sciences

Full Length Research Paper

Polyaniline/Fe_3O_4 coated on $MnFe_2O_4$ nanocomposite: Preparation, characterization, and applications in microwave absorption

Seyed Hossein Hosseini[1]* and A. Asadnia[2]

[1]Department of Chemistry, Faculty of Science, Islamshahr Branch, Islamic Azad University, Tehran-Iran.
[2]Young Researchers Club, Center Tehran Branch, Islamic Azad University, Tehran-Iran.

Accepted 3 June, 2013

Conductive polyaniline (PANi)/Fe_3O_4 is coated on the $MnFe_2O_4$ nanocomposite with multi core shell structure was synthesized by in-situ polymerization in the presence of dodecyl benzene sulfonic acid (DBSA) as the surfactant and dopant and ammonium persulfate (APS) as the oxidant. The structure and magnetic properties of Fe_3O_4 coated on the $MnFe_2O_4$ nanoparticles were studied by using powder X-ray diffraction (XRD) and vibrating sample magnetometer (VSM), respectively. The morphology, microstructure and DC conductivity of the nanocomposite were characterized by scanning electron Microscopy (SEM), fourier transform infrared spectroscopy (FTIR) and four-wire-technique, respectively. The microwave absorbing properties of the nanocomposite dispersed in resin acrylic with thickness of 1.4 mm were investigated by a HP 8720B vector network analyzer and standard horn antennas in Anechoic chamber in the frequency range of 8–12GHz. A minimum reflection loss of -18 dB was observed at 8.6 GHz.

Key words: Nano-structures, polymer-matrix composites (PMCs), magnetic properties, microwave absorption (nominated).

INTRODUCTION

Microwave absorbing material plays a great role in electromagnetic pollution, electromagnetic interference (EMI) shielding and stealth technology, to name but a few. An‘‘ideal’’microwave absorbing material owns such advantages as low thickness, low density, wide band width and flexibility simultaneously (Hosseini et al., 2011). In the past decades, the spinel ferrites have been utilized as the most frequent absorbing materials in various forms. Manganeseferrite ($MnFe_2O_4$) is a common spinel ferrite material and has been widely used in microwave and magnetic recording applications (Xiao et al., 2006). The absorbing characteristics of the materials depend on the frequency, layer thickness, complex permittivity (ε_r) and complex permeability (μ_r). Fe_3O_4 is a kind of microwave absorbers with complex permittivity and complex permeability (Li et al., 2008a). The core-shell structure composite nanoparticles often exhibit improved physical and chemical properties over their single-component counterpart and hence are very useful in a broader range of applications (Zhang and Li, 2009). Conducting polymer composites with micro/nanostructures have attracted significant academic and technological attention because of their unique physical properties and potential applications in

*Corresponding author. E-mail: shhosseini@iiau.ac.ir.

nanoelectronics, electromagnetics, and biomedical devices. Among these conducting polymers composites decorated with organic nanoparticles are of particular interest because possible interactions between the inorganic nanoparticles and the polymer matrices may generate some unique physical properties upon the formation of various micro/nanocomposites (Yang et al., 2009). Among conducting polymers, polyaniline (PANi) is perhaps the most versatile because of easier and inexpensive preparation methods. Also they have desirable properties, such as thermal and chemical stability, low specific mass, controllable conductivity and high conductivity at microwave frequencies (Phang et al., 2008). PANi is a conducting polymer so it has many potential applications in various fields such as electrical – magnetic shields, microwave absorbing materials, batteries, sensors and corrosion protections. The development of PANi properties has received considerable attention lately. The fabrication of PANi /ferrite nanocomposite has been reported by using different methods such as in situ polymerization of aniline in the presence of $Zn_{0.6}Cu_{0.4}Cr_{0.5}Fe_{1.5}O_4$ nanoparticles, micro emulsion process used to prepare PANi/NiZn ferrite nanocomposite and oxidative electro – polymerization of aniline in an aqueous solution in the presence of MnZn ferrite and NiMnZn ferrite. These studies created organic materials possessing both conducting and ferromagnetic functions. The electromagnetic measurements of the PANi/ferrites were improved and tailored by controlling the addition of the ferrite in the composite. Also, the contribution of ferrite to the PANi led to an increase in its thermal stability, however, it was decreased it electrical conductivity (Farghali et al., 2010). The preceding work, we have investigated microwave absorbing property of PANi–manganese ferrite nanocomposite in the frequency range of 8–12 GHz. We showed the PANi–manganese ferrite nanocomposites are good electromagnetic wave absorbent in the microwave range (Hosseini et al., 2011).

EXPERIMENTAL

Materials and instrumentals

Chemicals including metal salts, hexamethylene tetraamine (HMTA), potassium persulfate (KPS), ammonium persulfate (APS) and ethylene glycol (EG), $FeCl_3 .6H_2 O$, $FeSO_4.H_2 O$, $NH_3.H_2O$ (28%), Oleic acid (90%), are analytical grade (Merck) and were used without further purification. Water was deionized, doubly distilled, and deoxygenated prior to use. Styrene and methacrylic acid (analytical grade, Merck) were distilled to remove the inhibitor. Aniline monomer (analytical grade, Merck) was distilled twice under reduced pressure. DBSA and acrylic resin were of industrial grade.

The morphology of coated particles and nanocomposite was observed scanning electron microscopy (SEM) with a JSM-6301F (Japan) instrument operated at an accelerating voltage of 10 kV. X-ray powder diffraction (XRD) patterns of the nanoparticles assembles were collected on a Philips-PW 1800 with Cu-K radiation under Cu Kα radiation (λ=1.5406 Å). Fourier transform infrared spectroscopy (FTIR) spectra were recorded on a PerkinElmer spectrum FTIR using KBr pellets. The M–H hysteresis loops were measured by vibrating sample magnetometer (VSM) (RIKEN DENSHI Co. Ltd., Japan). Microwave absorbing properties were measured by a HP 8720B vector network analyzer and standard horn antennas in anechoic chamber.

Synthesis of manganese ferrite ($MnFe_2O_4$) nanoparticles

In a typical experiment, 10 ml styrene, 2 ml methacrylic acid and 0.054 g KPS were added to the flask with 100 ml deionized water. To eliminate oxygen effects the solution was purged with nitrogen before the process was initiated. The mixture was heated to 72°C and stirred with a magnetic stirrer. The polymerization was continued for 24 h and in the whole procedure the nitrogen was purged. Concentration of PS spheres in solution is 80 mg/ml, which was calculated by drying 5 ml colloid solution and weighing the remained solids (Hosseini et al., 2011).

Synthesis of coated particles

The coating procedure consisted of controlled hydrolysis of ferrous chloride aqueous solutions and other divalent metal salts in the presence of polystyrene latexes. In a typical preparation process, 2 ml PS colloid solution was diluted with 250 ml deoxygenated distilled water and then mixed with the metal salts solution, which contained 10 mmol $FeCl_2$ and 5 mmol $MnCl_2$. After it dispersed under ultrasonic for several minutes, the mixture was in corporate with 4 g HMTA and 0.5 g potassium nitrate and heated to 85°C under gentle stirring. After 3 h, the system was cooled to room temperature. The solution was poured in to excess distilled water, then magnetic particles were deposited using magnetic field. The precipitate was washed with distilled water for several times and then dried in oven at 80°C for 24 h. In addition, to modify the surface chemical properties of the magnetic spheres, 5 ml ethylene glycol (EG) was added in to the reaction solution before the incorporation of HMTA.

Iron Ferrite (Fe_3O_4)

$FeCl_3.6H_2O$ (24.3 g) and $FeSO_4.7H_2O$ (16.7 g) were dissolved in 100 ml de-ionized water under nitrogen gas while stirring vigorously at 80°C. Then 50 ml of ammonium hydroxide were added rapidly into the solution. The color of the solution turned to black instantly. Oleic acid (3.76 g) was added 30 min later. Then the suspension was kept at 80°C for 1.5 h. The magnetite nanoparticles were washed with de-ionized water until the pH value of the system reached neutral. The as-synthesized sample was dried in vacuum at room temperature.

Preparation of Fe_3O_4 -coated on the $MnFe_2O_4$ ($MnFe_2O_4/Fe_3O_4$)

0.1 g nano-sized particles of prepared $MnFe_2O_4$ were dispersed in 200 ml water solution of pH 6 under ultra sonification for 2 min. At this pH, the surface charge of $MnFe_2O_4$ in the solution is expected to be positive, and that of Fe_3O_4 be negative. The two solutions were mixed at 1/19 volumetric ratio (1/19 weight ratio of $MnFe_2O_4$/ Fe_3O_4) and subjected to sonification for 2 min so that $MnFe_2O_4$ particles were coated with Fe_3O_4 particles. The solution was then filtered using ultrafiltration membrane and dried at room temperature. We also prepared physically mixed Fe_3O_4 and $MnFe_2O_4$ by mixing the two solid Fe_3O_4 and $MnFe_2O_4$ samples with 1/19 weight ratio of $MnFe_2O_4$/ Fe_3O_4 for 1 h using a rotating machine.

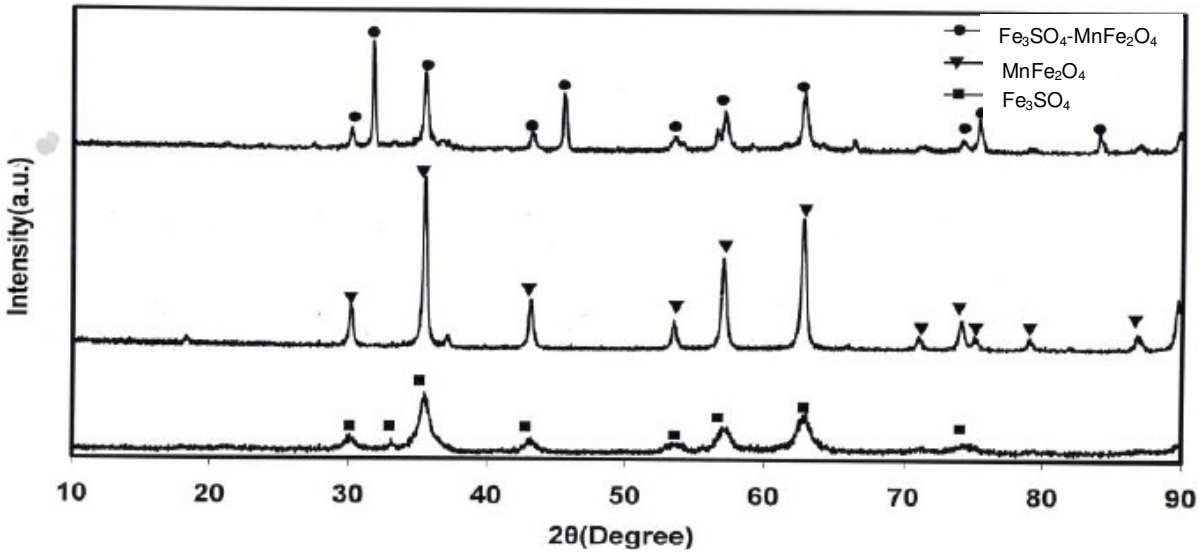

Figure 1. X-ray diffraction for Fe_3O_4, $MnFe_2O_4$ and $MnFe_2O_4/Fe_3O_4$ nanoparticles.

Synthesis of $MnFe_2O_4/Fe_3O_4$/PANi nanocomposite with multi core–shell structure

$MnFe_2O_4/Fe_3O_4$/PANi multi core–shell nanocomposites were prepared by in situ polymerization in the presence of DBSA as the surfactant and dopant and APS as the oxidant. The DBSA was dissolved in distilled water with vigorous stirring for about 20 min. The $MnFe_2O_4/Fe_3O_4$ nanoparticles (1.22 g) were added to the DBSA solution under stirring condition for approximately 1 h. Then 8 ml of aniline monomer was added to the suspension and stirred for 30 min. $MnFe_2O_4/Fe_3O_4$ nanoparticles were dispersed well in the mixture of aniline/DBSA under ultra sonicaction for 2 h. 20 g APS in 60 ml deionized water was gradually added drop wise to the stirred reaction mixture. Polymerization was allowed to proceed while stirring in an ice-water bath for 6 h. The nanocomposite was obtained by filtering and washing the suspension with deionized water and ethanol, respectively. The obtained green-black powder containing 15% $MnFe_2O_4/Fe_3O_4$ was dried under vacuum for 24 h.

RESULTS AND DISCUSSION

X-ray diffraction analysis

Figure 1 shows the XRD pattern of Fe_3O_4, $MnFe_2O_4$ and $MnFe_2O_4/Fe_3O_4$. According to the Figure, cubic ferrite Fe_3O_4 and $MnFe_2O_4$ nanoparticles have been obtained. However, it should be noted that there are some peaks of α-Fe_2O_3 in the XRD pattern for Fe_3O_4 (2θ=33,54) and $MnFe_2O_4$ (2θ=54) nanoparticles. All peaks correspond to the characteristic peaks of cubic type lattice for $MnFe_2O_4$ (JCPDS file no. 88-1965) and Fe_3O_4 (JCPDS file no. 19-0629). The obtained peak width from XRD patterns addresses to the sizes of nanoparticles. By using Debye–Scherrer equation, the sizes of $MnFe_2O_4$, Fe_3O_4 and $MnFe_2O_4/Fe_3O_4$ nanoparticles are calculated as 24.27, 7.38 and 31.65 nm, respectively. The XRD pattern indicates that $MnFe_2O_4/Fe_3O_4$ nanocomposites have formed. And compared with $MnFe_2O_4$ and Fe_3O_4 nanoparticles, the intensity of the characteristic peaks of α-Fe_2O_3 decreased in the $MnFe_2O_4/Fe_3O_4$ nanocomposites. This may be attributed to the coating of Fe_3O_4 nanoparticles on the surface of $MnFe_2O_4$ nanoparticles.

Magnetic properties

Magnetic properties of the samples were measured at room temperature with a VSM. The hysteresis loops are illustrated in Figure 2a-d. This Figure shows the magnetization (M) versus the applied magnetic field (H) for Fe_3O_4, $MnFe_2O_4$, $MnFe_2O_4/Fe_3O_4$ nanoparticles and d) $MnFe_2O_4/Fe_3O_4$/PANi nanocomposite (15 wt%) respectively. It can be inferred from the hysteresis loops that all the composite magnetic spheres are magnetically soft at room temperature with an applied field -10 kOe≤H≤10 kOe. Figure 2a shows the hysteresis loop of Fe_3O_4 (Hosseini et al., 2011). The value of saturation magnetization (M_s) is about 66.7 emu/g, the remnant magnetization (M_r) and the coercivity field are 17.81 emu/g and 110 Oe respectively. Figure 2b shows clear saturation magnetization (M_s) about 60 emu/g and remnant magnetization (M_r) and the coercivity field for $MnFe_2O_4$ nanocomposite are about 18 emu/g and 140 Oe respectively. The *Ms*, *Mr* and *Hc* are 37 emu/g, 11 emu/g and 155 Oe for $MnFe_2O_4/Fe_3O_4$ nanocomposite that have been shown in Figure 2c, respectively. It is lower than the pure ferrite manganese ferrite (Xiao et al., 2006) nanoparticles.

Although the $MnFe_2O_4/Fe_3O_4$ nanocomposites consist of two magnetic phases, the hysteresis loop shows a single-phase-like behavior, and the magnetization

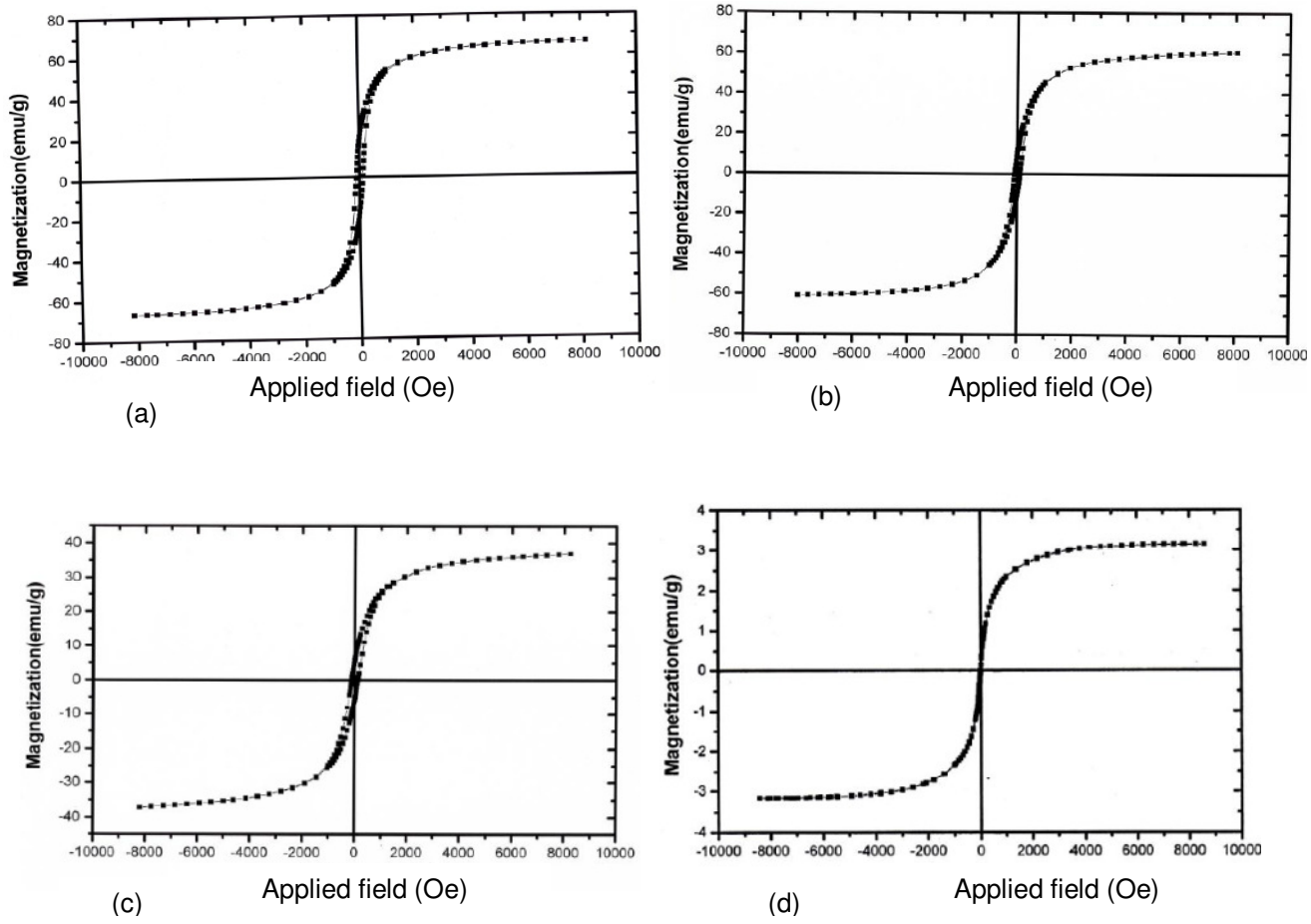

Figure 2. Magnetic hysteresis loop of a) Fe_3O_4 nanoparticle, b) $MnFe_2O_4$ nanoparticle, c) $MnFe_2O_4/Fe_3O_4$ and d) $MnFe_2O_4/Fe_3O_4$-PANi nanocomposites.

changes smoothly with the applied field. This indicates that the $MnFe_2O_4$ core and Fe_3O_4 first shell contact intimately. They are also clearly seen that the value of *Ms* decreases from 66.7 emu/g for Fe_3O_4 to 37emu/g and 60 emu/g for $MnFe_2O_4$ to 37 emu/g for the core-shell structure nanocomposites. And the *Hc* of $MnFe_2O_4/Fe_3O_4$ nanocomposites (155 Oe) is near to Fe_3O_4 (110 Oe) and higher than Fe_3O_4 (110 Oe) and $MnFe_2O_4$ (140 Oe) respectively. The changes in saturation magnetization and the coercivity can be attributed to the existence of Fe_3O_4 on the surface of $MnFe_2O_4$ nanoparticles which can result in the interparticle interaction at the interface of two phases. As saturation magnetization, the interphase interaction leads to the non-collinearity of the magnetic moments at the interface of two phases, and then results in there saturation magnetization (Chen et al., 2007). For coercivity, when the particles contact closely the interphase exchange coupling occurs, with which the rotation of the domains on one particle as the field is reversed, induces domains in contiguous particles to rotate, and thereby decreasing the coercivity (Zhang and Li, 2009; Zeng et al., 2004).

Figure 2d shows clear M_s about 3.15 emu/g, M_r about 0.35 emu/g and *Hc* Oe about 0 for $MnFe_2O_4/Fe_3O_4$/PANi nanocomposite (15 wt%) which is lower than pure ferrite and manganese ferrite nanoparticles. The magnetization curve of the sample shows weak ferromagnetic behavior, with slender hysteresis. Magnetic properties of nanocomposites containing magnetite or ferrite particles have been believed to be highly dependent on the sample shape, crystallinity, and the value of magnetic particles, so that they can be adjusted to obtain optimum property.

Morphology investigation

Figure 3a-c shows the SEM images for a) $MnFe_2O_4$ and b) Fe_3O_4 nanoparticles and $MnFe_2O_4/Fe_3O_4$/PANi nanocomposite. As shown in Figure 3a, the spongy-shaped $MnFe_2O_4$ was seen with a small quantity of amorphous phase. The range of average diameter of spongy-shape is 40 to 50 nm. Figure 3b shows the SEM image for Fe_3O_4 nanoparticles. The range of average

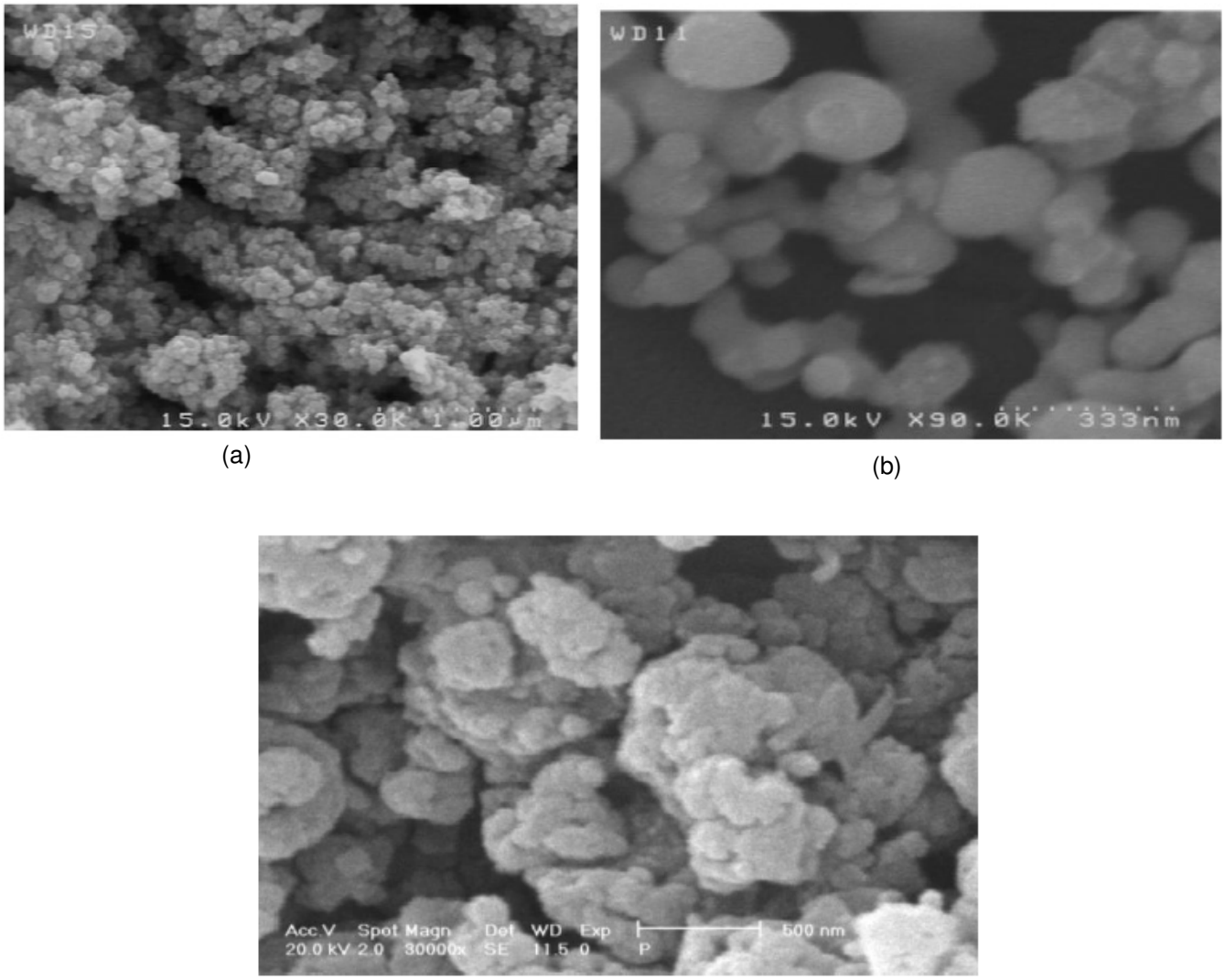

Figure 3. SEM microphotographs of a) Fe_3O_4 nanoparticle, b) $MnFe_2O_4$ nanoparticle and c) $MnFe_2O_4/Fe_3O_4$/PANi nanocomposite.

diameter is 30 to 40 nm. In Figure 3c, it is found that the $MnFe_2O_4/Fe_3O_4$/PANi nanocomposite (15 wt%) still retains the morphology of PANi shape. It is much unknown how to form spongy-shaped composite in the polymerization process. The SEM image clearly shows that the $MnFe_2O_4/Fe_3O_4$ was distributed rather homogeneously, and ultrasonication is effective for dispersing nanoferrite in the polymer matrix.

FTIR spectra analysis

Figure 4a-d shows the FTIR spectra of $MnFe_2O_4$, Fe_3O_4 $MnFe_2O_4/Fe_3O_4$ and $MnFe_2O_4/Fe_3O_4$/PANi nanocomposite, respectively. In ferrites, the metal ions are usually situated in two different sublattices, designated as tetrahedral and octahedral sites according to the geometrical configuration of the oxygen nearest neighbors (Hosseini et al., 2011). It was observed from Figure 4(a,b) that the peak at 578 cm^{-1} is intrinsic vibrations of Fe-O in $MnFe_2O_4$ and peaks at 586 and 411 cm^{-1} are intrinsic vibrations of Fe-O in Fe_3O_4. The peaks at 651 and 562 cm^{-1} are intrinsic vibrations of Fe-O in Fe_3O_4 and $MnFe_2O_4$ have been shown in Figure 4c. The characteristic peaks of styrene occur at 1559, 1338-1067 and 851 cm^{-1}. The peak at 1559 is attributed to the styrene ring. The peak at 1338 cm^{-1} is attributed to the characteristic C=C stretching ring. The peak at 851 cm^{-1} is related to the C–H outer bending vibrations. As shown in Figure 4d, the characteristic peaks of $MnFe_2O_4/Fe_3O_4$/PANi nanocomposite occur at 1555, 1483, 1302, 1241, 1122, 1028, 1002, 876, 800, 675 and 580 cm^{-1}. The peaks at 1555 and 1483 $cm^{-1}$are attributed to the characteristic C=C and C-N stretching of the

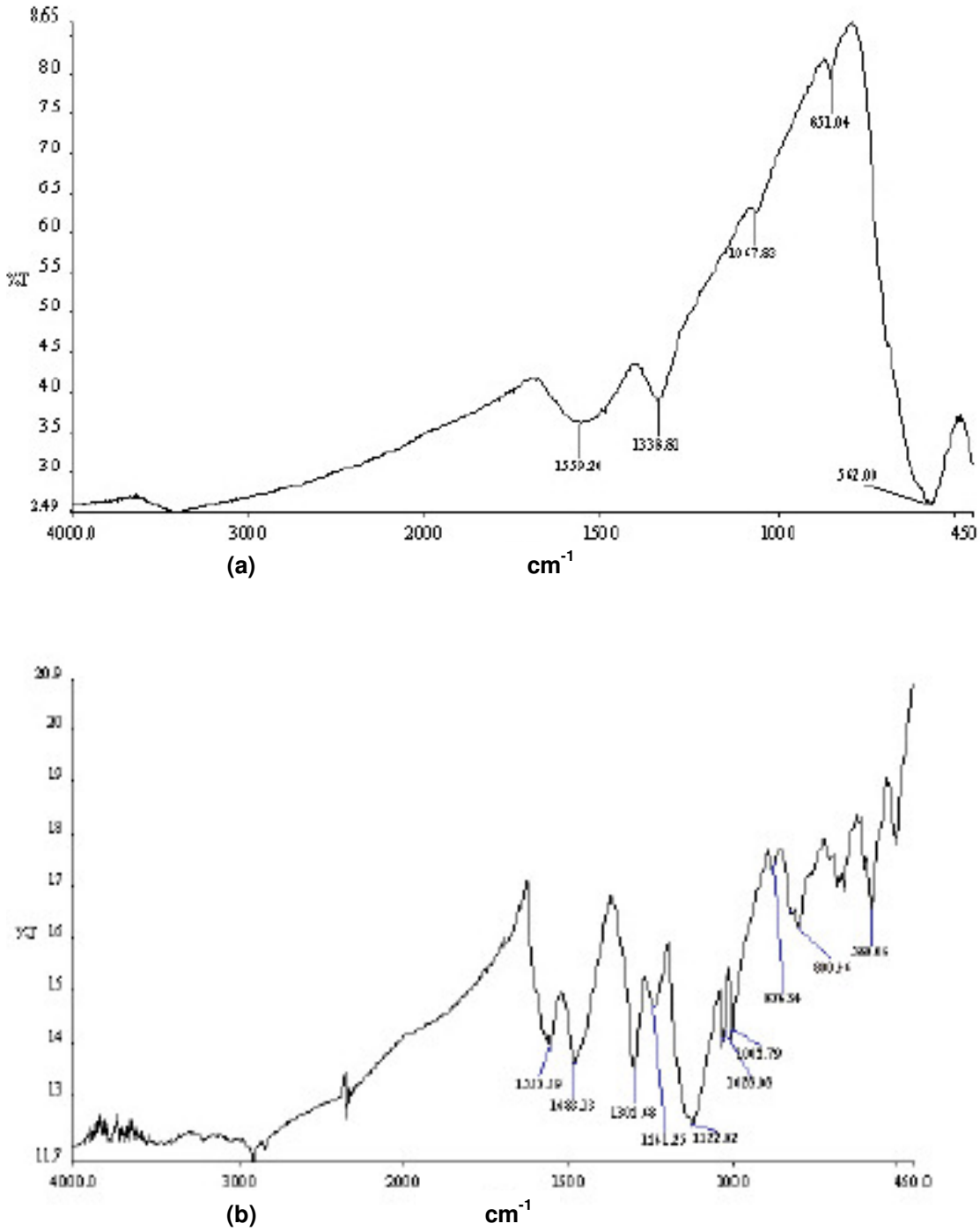

Figure 4. FTIR spectra: a) Fe_3O_4 nanoparticle, b) $MnFe_2O_4$ nanoparticle c) $MnFe_2O_4/Fe_3O_4$ nanoparticle and d) $MnFe_2O_4/Fe_3O_4$/PANi nanocomposite.

quinoid and benzenoid rings of polyaniline; the peaks at 1302 and 1241 cm^{-1} correspond to N–H bending and asymmetric C–N stretching modes of the benzenoid ring. The peak around 1122 cm^{-1} is associated with vibrational modes of N=Q=N (Q refers to the quinonic type rings), indicating that PANi is formed in our sample. The peak at 1028 cm^{-1} attributed to the symmetric and anti-symmetric stretching vibration of SO_3 group of dopant (DBSA). The peaks at1002, 876 and 800 cm^{-1} are attributed to the p-disubstituted aromatic ring C–H out-of-plane bending. However, the characteristic peaks of Fe_3O_4 and $MnFe_2O_4$ can be observed at higher wavenumbers (675 and 580 cm^{-1}) indicating that there is an interaction between $MnFe_2O_4/Fe_3O_4$ nanoparticles and PANi chain.

DC conductivity

DC conductivity of samples at room temperature is shown in Table 1. When the PANi is doped by DBSA, the conductivity was improved to 26 S/cm, which means that doping H^+ increase conductivity of PANi. When 15% mass content of $MnFe_2O_4/Fe_3O_4$ nanoparticles was incorporated, the conductivity of $MnFe_2O_4/Fe_3O_4$/PANi nanocomposite was sharply reduced from 26 to 0.9 S/cm. The decrease in conductivity of $MnFe_2O_4/Fe_3O_4$/PANi composites may be attributed to the insulting behavior of the ferrite and partial blockage of the conductive path by $MnFe_2O_4/Fe_3O_4$ in the core of the nanoparticles (Li et al., 2008b).

Reflection loss analysis

According to transmission line theory, the reflection loss (RL) of electromagnetic radiation, under normal wave incidence at the surface of a single-layer material backed by a perfect conductor can be given by:

$$RL = 20 \log \left| \frac{Z_{in} - Z_0}{Z_{in} + Z_0} \right| \quad (1)$$

where Z_0 is the characteristic impedance of free space,

$$Z_0 = \sqrt{\frac{\mu_0}{\varepsilon_0}} \quad (2)$$

Z_{in} is the input impedance at free space and materials interface:

$$Z_{in} = \sqrt{\frac{\mu_r}{\varepsilon_r}} \tanh \left[j \frac{2\pi f t}{c} \sqrt{\mu_r \varepsilon_r} \right] \quad (3)$$

where μ_r and ε_r are the complex permeability and permittivity of the composite medium respectively, which can be calculated from the complex scatter parameters, c is the light velocity, f is the frequency of the incidence electromagnetic wave and t is the thickness of composites. The impedance matching condition is given by $Z_{in} = Z_0$ to represent the perfect absorbing properties (Chen et al., 2007). There are two different concepts to satisfy the zero reflection condition. The first concept is the ‘‘matched characteristic impedance’’. The intrinsic impedance characteristic of material is made equal to the impedance characteristic of the free space. The second is the ‘‘matched-wave-impedance’’ concept. The wave impedance at the surface of the metallic substrate layer is made equal to the intrinsic impedance of the free space. In this work, the second concept was applied. The condition of maximal absorption is satisfied at a particular point where thickness and frequency match each other. Ferrites are the only materials that present two matching frequencies and thicknesses. The first matching at low-frequency is associated with the mechanisms of magnetic resonance and shows a dependence on the chemical composition. The second matching at high-frequency is associated with the thickness of absorbent material. To satisfy the zero-reflection condition where maximum absorption would occur, Z_{in} should be 1 to prevent reflection. This can be ideally achieved when the material presents $|\mu_r| = |\varepsilon_r|$. In this case, the performance of electromagnetic wave-absorbing material increases linearly with the increase in thickness. In practical terms, however, this is rarely achieved because the values of complex permeability and complex permittivity are very different in the frequency range of interest. When $|\mu_r| \neq |\varepsilon_r|$, we should consider two other cases. For materials with intrinsic impedances greater than unity, $|\mu_r| > |\varepsilon_r|$, the minimum reflection loss occurs at around a half-wavelength thickness of the material, and for materials with intrinsic impedances lower than unity, $|\mu_r| < |\varepsilon_r|$, the minimum reflection loss occurs at around a quarterwavelength thickness of the material. Within the microwave region, ferrites usually present electromagnetic characteristics of $|\mu_r| < |\varepsilon_r|$, giving rise to the term ‘‘quarter-wavelength absorbent’’. Minimum loss occurs when the thickness is about an odd multiple of one quarter of the wavelength of the incident frequency. It measured inside the absorbing material, and the material has the proper loss factor for this particular thickness .The thickness, d, can be written as Equation (4), where c is the speed of light and f is the frequency of interest (Bueno et al., 2008).

$$d = \frac{c}{4f\sqrt{|\mu_r||\varepsilon_r|}} \quad (4)$$

Investigation of microwave absorbing properties

Nanocomposite dispersed in acrylic resins then the mixture was pasted on metal plate with the area of 100 ×100 mm as the test plate. The microwave absorbing properties of the nanocomposite with the coating thickness of 1 mm were investigated by using a HP 8720B vector network analyzer and standard horn antennas in anechoic chamber in the frequency range of 8–12 GHz. Figure 5 shows the microwave absorption behavior of the $MnFe_2O_4/Fe_3O_4$/PANi nanocomposite. For PANi with the coating thickness of 1 mm, the minimum reflection loss is -8 dB at the frequency of 8-12 GHz. For $MnFe_2O_4/Fe_3O_4$/PANi nanocomposites with the coating thickness of 1 mm, the reflection loss values were obtained less than -10 dB in the frequency of 8–12 GHz and its value of minimum reflection loss are -18 and -17 dB at the frequency of 8.6 and 9.2 GHz, respectively. Compared with the core-shell $MnFe_2O_4$/PANi (-15.3 dB at 10.4 GHz) (Hosseini et al., 2011) and the new multi core-

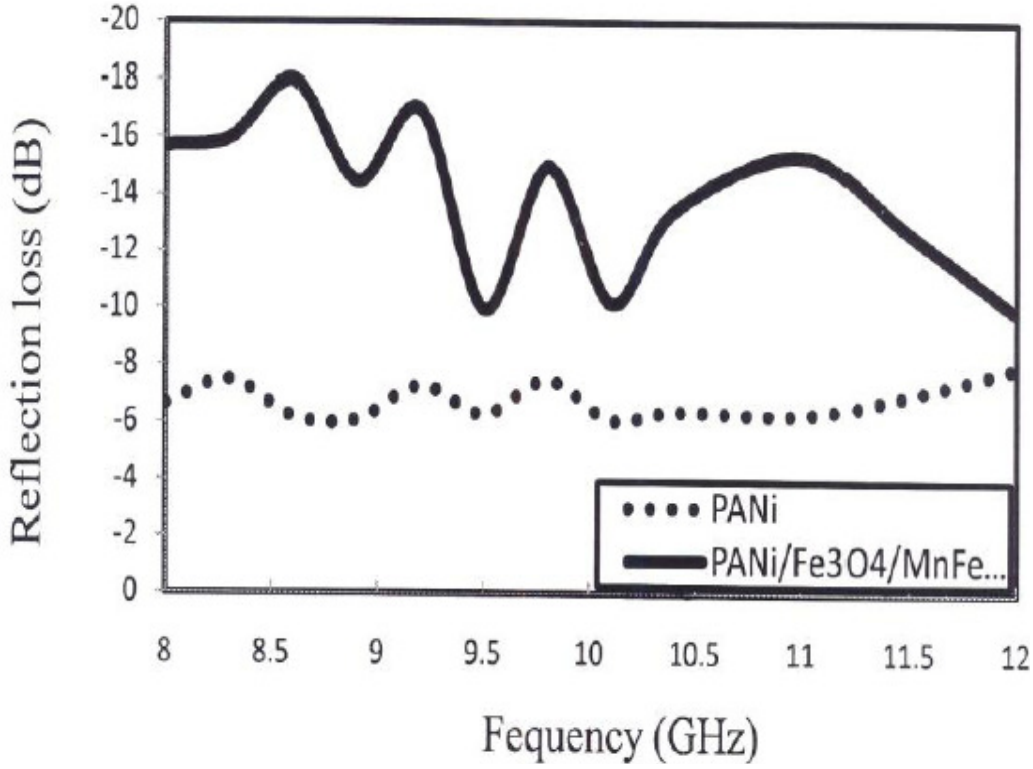

Figure 5. Frequency dependence of RL for the $MnFe_2O_4$/PANi nanocomposite.

shell $MnFe_2O_4/Fe_3O_4$/PANi nanocomposite (-18 dB at 8.6 GHz and -17 dB at 0.2 GHz), the microwave absorption properties of multi core-shell structure nanocomposite have been improved effectively. The reason for this improvement may be due to the interphase interaction between the cubic $MnFe_2O_4$ and cubic ferrite Fe_3O_4. These two kinds of ferrite combine intimately with the two step co-precipitation synthetic method, so they can couple to each other by an exchange through interface of ferrite particles. The interphase interaction which can cause the interphase exchange coupling and the non-collinearity of the magnetic moments at the interface of two phases exists between cubic ferrite materials. The interphase interaction can affect the microwave absorption properties of the two-phase composites had been shown in previous study (Zhang and Li, 2009). As mentioned above, the results of this work are consistent with these previous reports.

Conclusion

The obtained magnetic nanoparticles are of a diameter of 24.27, 7.38 and 31.65 nm for $MnFe_2O_4$, Fe_3O_4 and $MnFe_2O_4/Fe_3O_4$, respectively. $MnFe_2O_4/Fe_3O_4$/PANi ferrite nanocomposite with the magnetic behavior is successfully synthesized by *in situ* polymerization of aniline in the presence of $MnFe_2O_4/Fe_3O_4$ nanoparticles. The results of spectro-analysis indicate that there is an interaction between PANi chain and ferrite particles. Furthermore; for 1 mm thickness of nanocomposite used, a minimum reflection loss of -18 and -17 dB were observed at 8.6 and 9.2 GHz, respectively. Journal of Nanomaterials, Vol. 2012, 1687-4110 (2012).

REFERENCES

Bueno AR, Gregori M, No´brega MCS (2008). Microwave-absorbing properties of $Ni_{0.50-x}Zn_{0.50-x}Me_{2x}Fe_2O_4$ (Me=Cu, Mn, Mg) ferrite–wax composite in X-band frequencies, J. Magn. Magn. Mat. 320:864-870.

Chen N, Mu GH, Pan XF, Gan KK, Gu MY (2007). Microwave absorption properties of $SrFe_{12}O_{19}/ZnFe_2O_4$ composite powders, Mater. Sci. Eng. B 139:256-260.

Farghali AA, Moussa M, Khedr MH (2010). Synthesis and characterization of novel conductive and magnetic nanocomposites, J. Alloys Comp. 499:98–103.

Hosseini SH, Mohseni SH, Asadnia A, Kerdari K. (2011). Synthesis; characterization and microwave absorbing properties of polyaniline/$MnFe_2O_4$ nanocomposite, J. Alloys Comps. 509:4682-4687.

Li X, Han X, Tan Y, Xu P (2008a). Preparation and microwave absorption properties of Ni–Balloy-coated Fe_3O_4 particles, J. Alloys Comp. 464:352–356.

Li Y, Zhang H, Liu Y, Wen Q, Li J (2008b). Rod-shaped polyaniline–barium ferrite nanocomposite: preparation, characterization and properties, Nanotechnology, 19:105605-105610.

Phang SW, Tadokoro M, Watanabe J, Kuramoto N (2008). Microwave absorption behaviors of polyaniline nanocomposites containing TiO_2 nanoparticles, Cur. Appl. Phys. 8:391–394.

Xiao HM, Liu XM, Fu SY (2006). Synthesis, magnetic and microwave

absorbing properties of core-shell structured $MnFe_2O_4/TiO_2$ nanocomposites, Comp. Sci. Tech. 66:2003-2008.
Yang C, Li H, Xiong D, Cao Z (2009). Hollow polyaniline/Fe_3O_4 microsphere composites: Preparation, characterization, and applications in microwave absorption, Reactive Functional Polym. 69:137–144.
Zeng H, Sun S, Li J, Wang ZL, Liu JP (2004). Tailoring magnetic properties of core/shell nanoparticles, Appl. Phys. Lett. 85:792-794.
Zhang L, Li Z (2009). Synthesis and characterization of $SrFe_{12}O_{19}/CoFe_2O_4$ nanocomposites with core-shell structure, J. Alloys Comp. 469:422–426.

academicJournals

Vol. 8(22), pp. 1218-1227, 16 June, 2013
DOI: 10.5897/IJPS12.594
ISSN 1992-1950 © 2013 Academic Journals
http://www.academicjournals.org/IJPS

International Journal of Physical Sciences

Full Length Research Paper

Electrical characterization of conducting poly(2-ethanolaniline) under electric field

Seyed Hossein Hosseini[1]*, Ghasem Asadi[2] and S. Jamal Gohari[3]

[1]Department of Chemistry, Faculty of Science, IslamShahr Branch Islamic Azad University, Tehran-Iran.
[2]Department of Chemistry, Faculty of Science and Engineering, Shar-e-Rey Branch, Islamic Azad University, Tehran-Ghom Express Way, Tehran-Iran.
[3]Department of Chemistry, Faculty of Science, Imam Hossein University, Babaee Express Way, Tehran – Iran.

Accepted 23 May, 2013

We have studied conductivity and molecular weight obtained poly(2-ethanolaniline), P2EANi. P2EANi synthesized according to the best ratio of obtained molar of initiator to monomer at different reaction times. Then we measured the mass and conductivity of the obtained polymers in the best time of polymerization. Next, we repeated these reactions under different electric fields in the most appropriate time and measured the mass and conductivity of obtained polymers. As a result, intensity of the required electric field for polymerization was determined. After which the polymerization was carried out at the best electric field at different times. Finally, the best time and amount of the electric field for polymerization were determined. Moreover, we studied the doping of polymerization in the presence of an electric field by applying different dopants and other initiators. Then compared the obtained results to the results of a similar condition; but without the electric field. As a result we found the best condition for the reaction was determined as follows; the P2EANi with a high molecular weight was synthesized under the electric field, Mw=193749 g/mol, with Mw/Mn=2.3. The conductivity of the black films oxidized by ammonium peroxydisulfate and doped with dodecylbenzene sulfonic acid cast from NMP was higher than 0.118 S/cm under 10 KV/Cm^2 electric field and showed an enhanced resistance to aging. It can be concluded that polymers synthesized under electric field probably have better physical properties as a result of less branching and high electrical conductivity.

Key words: Polymers, chemical synthesis, electrical conductivities, electric field.

INTRODUCTION

Conducting polymers constitute an emerging class of materials. Among the organic conducting polymers, polyaniline is the only conducting polymer whose properties depend on the oxidation state, its protonation state/doping level as well as the nature of dopants. Among conducting polymers, polyainilne has received greater attention due to its advantages over other conducting polymers. Simplicity of its preparation from cheap materials, superior resistance to air oxidation, and controllable electrical conductivity by doping and de-doping (Pron and Ranou, 2002), makes it very useful in preparing light-weight batteries (Senadeera and Pathirathne, 2004), liquid crystalline polymers (Gato et.al., 2001; Hosseini and Mohammadi, 2009), optical activities (Li et al., 2004), ion exchange materials (Hosseini and Noor, 2005) and sensors (Hosseini et al., 2005, 2006; Hosseini, 2006).

A number of mechanisms for the electric field effects in the chemical reactions have been suggested, well documented, and undergone a proper theoretical

*Corresponding author. E-mail: shhosseini@iiau.ac.ir

analysis (Buchachenko, 2000). Any polar molecule is composed of at least two atoms. Furthermore, a molecule, has an inherent dipole moment with random direction, at room temperature, dipoles and hence the bulk materials are not polarized. An external electric field, applies two equal and opposite forces of any dipole and tries to adjust them with itself. If the field is sufficiently intense and there is no other effective factor, like thermal energy, polarization reaches its saturation value, $P_s=NP_m$. In which P_m is the molecular dipole moment and N is the number of molecules per unit volume. Polarization is between zero and saturation value that can be calculated using a statistical mechanism. From this point of view, the polarizability is (Reits et al., 1979): $\alpha = P_0^2/3kT$ and we have: $P=\alpha E_m$. If we show a monomer molecular dipole moment, by P_0, for a dimmer $P_m=2P_0$, and for a polymer string that is composed of n monomers, $P_m=nP_0$. So as the polymer grows, its polarizability increases as the following: $\alpha= n^2P_0^2/3kT$. This order will increase the electrical conductivity of conductive polymers. Therefore, effects of electric field on doping of conductive polymers can be investigated (MacDiarmid, 2001; Manoha et al., 2002).

Polyaniline and poly2-ethanol aniline are the most of the promising conducting polymers because of its chemical stability and high conductivity. The addition of substituent into the side chain of polyaniline enhances its solubility and processability. On the other hand, there has been no report on polymerization of poly2-ethanol aniline under electric or magnetic fields. Therefore, we think polymerization of poly2-ethanol aniline under electric field can be modified in terms of all its properties. Considering molecular weight, orientation and future applications such as liquid crystalline and optical activities, modified poly2-ethanol aniline can be used. Here, we present the syntheses and properties of poly2-ethanol aniline with a side chain group under an electric field. Therefore, the effect of applying the electric field on polymerization with specific amount of electrical conductivity and molecular weight is rather limited.

EXPERIMENTAL

Chemicals used in this study were American Chemical Society (ACS) grade. 2-Ethanol aniline (Merck) was dried with NaOH, fractionally distillated under reduced pressure from CaH_2. Other chemicals such as, ammonium peroxodisulfate (APS), dodecylbenzene sulfonic acid (DBSA), champhor sulfonic acid (CSA), methane sulfonic acid (MSA), p-toluene sulfonic acid (PTSA), acetic acid (AA), $FeCl_3.6H_2O$, KI and other reagents were purified as per standard procedure before use.

Instrumentals

Conductivity changes were measured with a four probe device (made to the, ASTM Standards, F 43-93). An Electric field device was applied by Hipotronics S.O. No. 004390-00, HV power supply, model 830.50 made in USA. A fourier-transform infrared spectrometer, FT-IR, (Bruker) was used in the spectral measurements of the polymer and graft copolymer and reported (sh=sharp, w=weak, m=medium, b=broad). Proton and carbon nuclear magnetic resonance (FT-^{1}H and ^{13}C NMR) spectra were recorded at 250 MHz on a BruKer WP 200 SY spectrometer. NMR data are reported in the following order: chemical shift (ppm), spin multiplicity (as singlet, doublet, triplet, quartet, multiplet, and broad peak), integration UV-Visible spectra were obtained by Perkin Elmer Lambda 15 spectrophotometer. Molecular weight was measured at 30°C with a gel permeation chromatography (GPC), (Waters Associates, model 150-C). Three styragel packed columns with different pore sizes ($10^4 – 10^6$ A°) were used. The mobile phase was m-cresol with flow rate of 1.5 ml/min. The thermal properties (thermo gravimetric analysis (TGA)) and differential scanning calorimetry (DSC)) of polymer were performed by STA 625-PL Thermal Science and heating rate of 10 °C min^{-1}. Scanning electron microscopy (SEM) was used to study the type of surface morphology of polymer. A Cambridge S-360 SEM was used for this purpose.

Preparation of P2EANi in the absence of electric field

Project participants followed the same instructions to oxidize 0.001 mol 2-ethanol aniline hydrochloride with 0.001 mol ammonium peroxydisulfate, $(NH_4)_2S_2O_8$, in aqueous medium. 2-Ethanol aniline hydrochloride (purum; 0.1 g) was dissolved in 10 ml HCl 1 M in a 50 ml volumetric flask. Ammonium peroxydisulfate (purum; 0.228 g) was dissolved in 10 ml HCl 1 M, and then added. Both solutions were kept for different times (5, 10, 15, 20, 30, 40, 50, 60 and 120 min) at room temperature (~18 to 24°C). The P2EANi precipitate was collected on a filter, and washed with three 10 ml portions of 0.1 M HCl, and acetone. P2EANi hydrochloride powders were dried air and then in a vacuum at 60°C. Weighed and also their electrical conductivities were measured by four probe method (Hosseini et al., 2005, 2006).

The P2EANi powders with $FeSO_4$, KI, $FeCl_3.6H_2O$ as initiators and $HClO_4$, H_2SO_4, AA, PTSA, MSA, DBSA and CSA as dopants were synthesized in similar manner. UV (DMSO); λ_{max}= 320 nm (2.45 intensity). FT-IR (KBr): 3550-3100(b), 3015(w), 2930(w), 1615(m), 1450(w), 1515(sh), 1349(m), 1250(m), 1130(sh), 830(m) cm^{-1}. ^{1}H-NMR (DMSO); δ 2.45 (2H, s), 3.50 (2H, t), 3.70 (2H, t), 4.50 (broad), 7.20 (1H, s), 7.35 (1H, s), 7.55 (1H, d), 7.70 (2H, s) ppm. ^{13}CNMR (DMSO); δ 51.5, 54.5, 119.8, 126.5, 127.7, 128.7, 135.1 ppm.

Preparation of P2EANi under electric field

P2EANi was prepared under the same chemical circumstances but with different electric fields (5, 10, 15 and 20 KV/Cm^2), in 60 min, at room temperature. Then, P2EANi was prepared by the same reaction but, in various times (30, 45, 60, 90 and 120 min) intervals at the best amount of electric field. UV (DMSO); λ_{max} = 340 nm (2.80 intensity), 450 nm (0.5 intensity), 590 nm (0.3 intensity). FT-IR (KBr): 3550-3100(b), 3010(w), 2923(w), 1604(m), 1503(sh), 1341(m), 1247(m), 1156(sh), 822(m) cm^{-1}. ^{1}H-NMR (DMSO); δ 2.51 (2H, s), 3.34 (2H, t), 3.67 (2H, t), 4.61 (broad), 7.10 (1H, s), 7.30 (1H, s), 7.34 (1H, d), 7.51 (2H, s) ppm. ^{13}CNMR (DMSO); δ 52.0, 55.4, 121.9, 127.4, 128.9, 129.1, 136.2 ppm.

RESULTS AND DISCUSSION

Spectrometric studies

Figure 1 shows the FT-IR spectrum of P2EANi under the

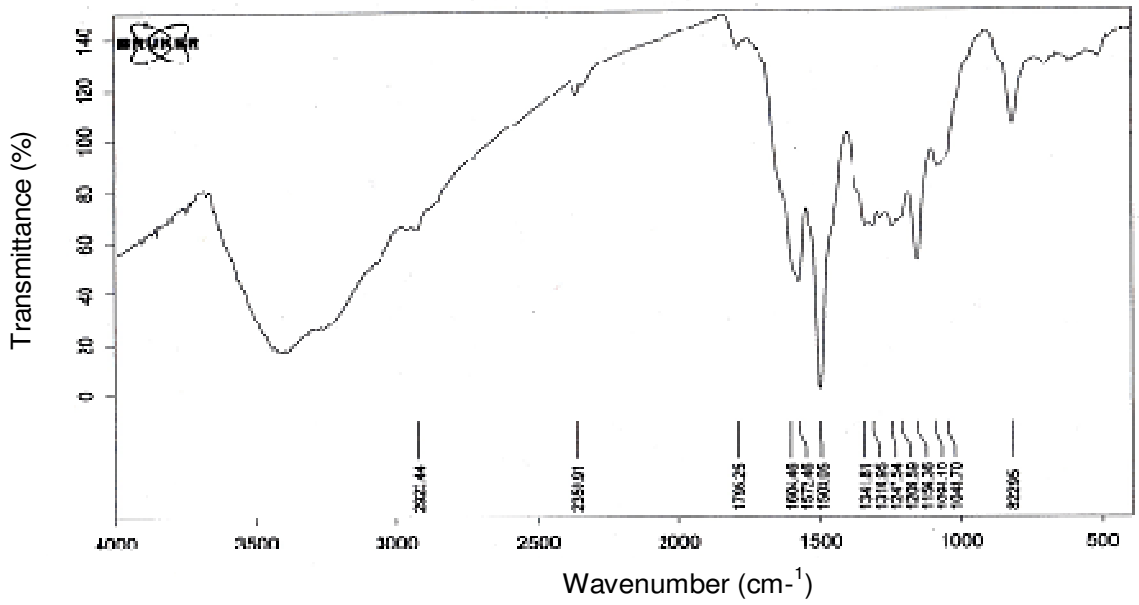

Figure 1. FT-IR spectrum of P2EANi after electric field.

electric field. The special peaks of this spectrum are 3330 cm^{-1} (O-H Stretching H-bonding), 2923 cm^{-1} (C-H stretching aliphatic), 1604 and 1503 cm^{-1}(C=C stretching aromatic) and 1156 cm^{-1} (C-O stretching) and you can see C-H stretching aromatic overlapped with OH stretching.

Figure 2a shows the UV-Vis spectrum of P2EANi prepared without an electric field at the DMSO solvent. In this spectrum the 298 nm peak relates to benzenoid diamine forms. At this spectrum the quinoid diimine from the peak cannot be seen because the polymer is lattice matrix. The UV-visible spectrum of P2EANi under electric field is shown in Figure 2b. This figure shows three peaks, 340, 450 and 590 nm, of which two last ones are related to quinoic form of P2EANi. The two last peaks are not in Figure 2a which relates to P2EANi prepared without an electric field. As we know, by increasing the length of chain and subsequently rising the number of conjugated double bonds, a decrease in energy difference $\pi \rightarrow \pi^*$ occurs, so that it causes an increase in the wavelength. The spectrum of 340 nm region is for the second peak of aniline groups and the $\pi \rightarrow \pi^*$ is a conjugated couple system for the benzoic states and wide peak in 590 nm comes from the transfer of $\pi \rightarrow \pi^*$ quinion of aniline groups (for the polaron and bipolaron transfers).

The ^{1}HNMR spectrum of P2EANi under an electric field in d^{6}-DMSO as solvent is shown in Figure 3. The peaks observed in 7.1 to 7.5 ppm related to different aromatic protons in polymer. The peak of 4.5ppm is related to OH group of ethanol on the polymeric string. The 3.3 and 3.6 ppm regions are related to ethylenic protons and 2.5 ppm signal as well as protons of DMSO impurity. Figure 4 shows the ^{13}CNMR spectrum of P2EANi. At this spectrum, peaks of 52.3 and 55.4 regions are related to aliphatic carbons of the ethanol group. The signals of 121.9, 127.4, 128.9, 129.1 and 136.2 ppm regions are related to aromatic carbons of ring.

Thermal properties studies

Figure 5a and b shows the TGA thermograms of P2EANi before and after electric field, respectively. In comparison of figures shows that P2EANi produced under electric field is more stable than P2EANi produced in the absence of an electric field. In Figure 5b, we see that the polymer is stable up to 170°Cb, and loses it's weight at region 170 to 280°C slightly which relates to evaporation of solvent and probable water , and ethanol groups of P2EANi begins to be destroyed and reaches its maximum value at 280°C. The 33.8% loss of molecular weight is the special characteristic of this temperature. At 390°C the lost weight is 59.5% and the polymer will be destroyed completely at 700°C, and 27.7% of initial weight remains to form the ash. Also, the peaks at 250 and 350°C, are related to exothermic states and the peaks at 280 and 390°C, are related to endothermic states of thermal treatment of the polymer that is due to weight loss of the polymer.

Scanning electron microscopic studies

Figure 6a and b shows SEM images of P2EANi synthesized in absence and presence of an electric field,

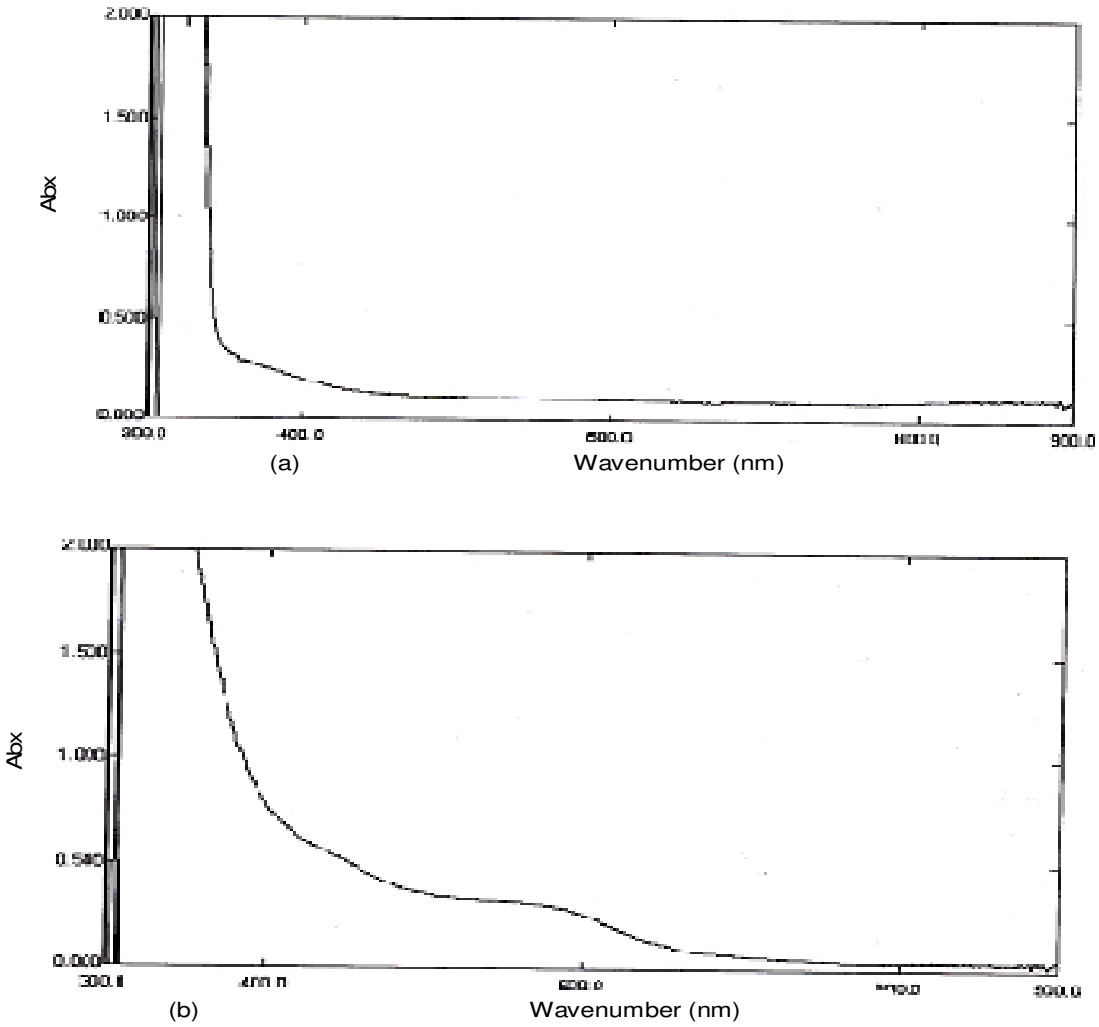

Figure 2. UV-visible of P2EANi prepared in a) absence and b) presence of electrical field in DMSO.

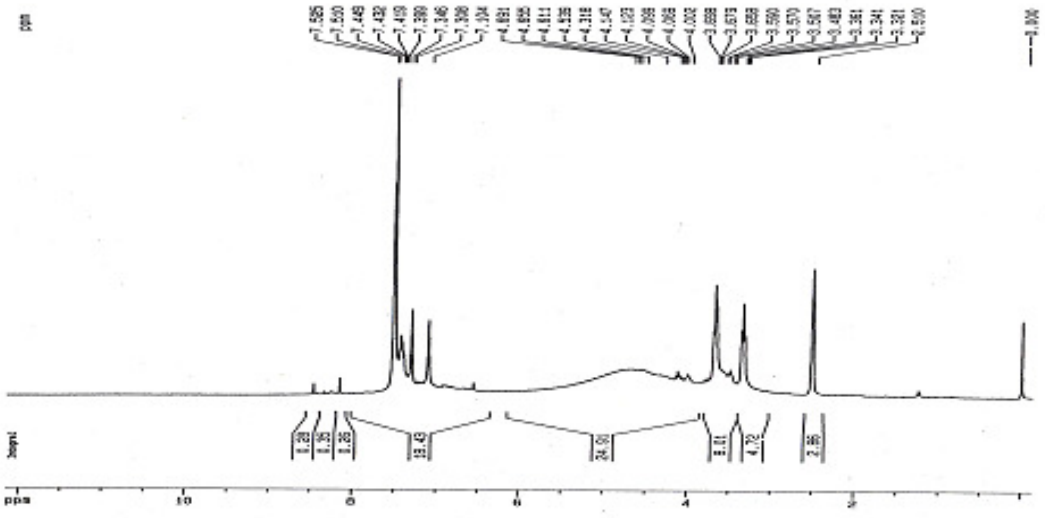

Figure 3. [1]HNMR spectrum of P2EANi after electric field.

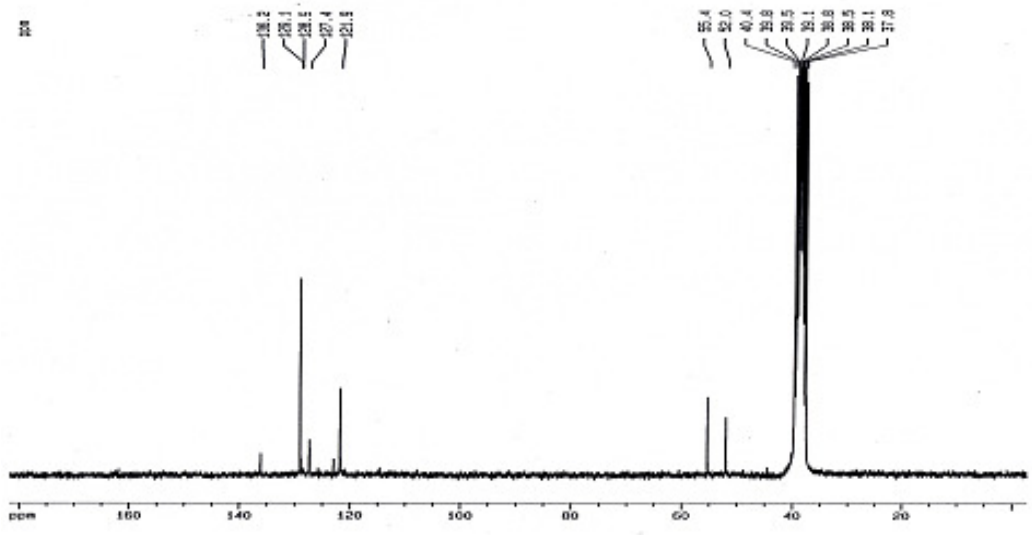

Figure 4. ^{13}CNMR spectrum of P2EANi after the electric field applied.

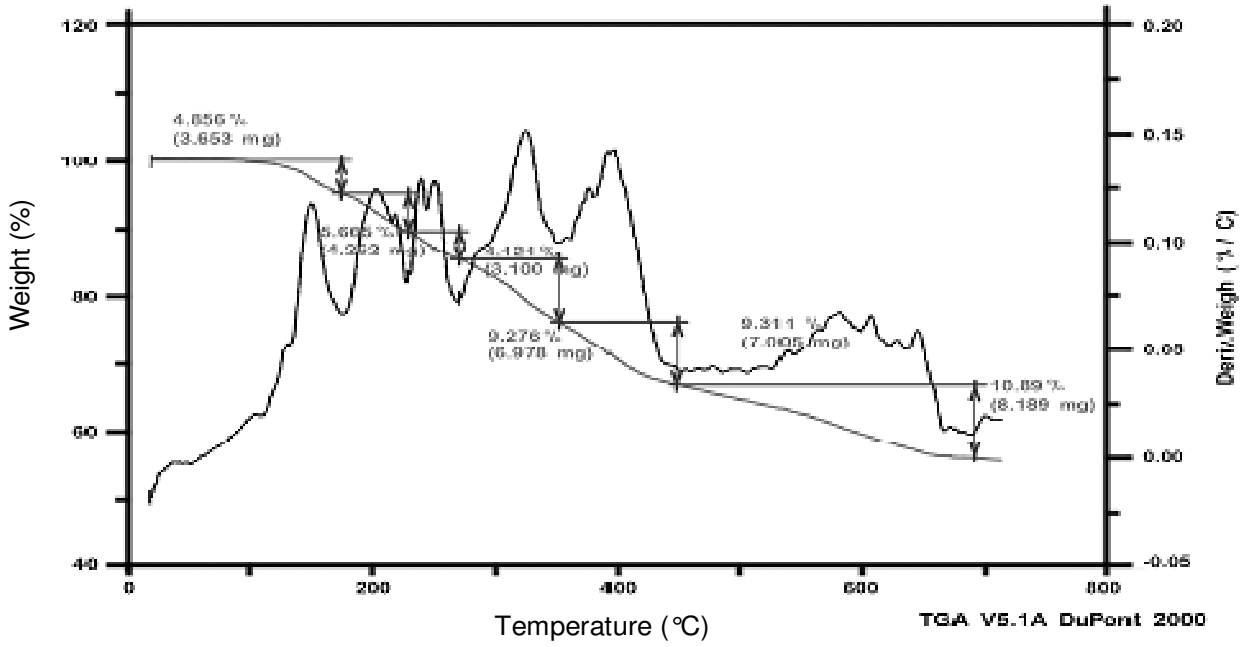

Figure 5. TGA thermograms of P2EANi prepared in a) absence of an electrical field and b) the presence of an electrical field.

respectively. The Figure 6a shows spherical masses of P2EANi chains that are grown on the form of bulk polymerization. But Figure 6b shows the SEM of synthesized P2EANi in the presence of an electric field. Figure 6b shows that P2EANi has a smooth form and relatively homogeneous surface. This is caused by growing more polymer chains with gathering and developing an order in the polymer morphology under an electric field.

Molecular weight distribution studies

To obtain the molecular weight distribution, we used GPC method. In this way, we found that for the prepared polymer in absence of the electric field state, the mean molecular weight is 35440 g/mol, and the scattering is 3.7. Also, the mean weight of molecular mass is 131128 g/mol while for the polymer prepared at the electric field, the mean molecular weight is 84239 g/mol, the scattering

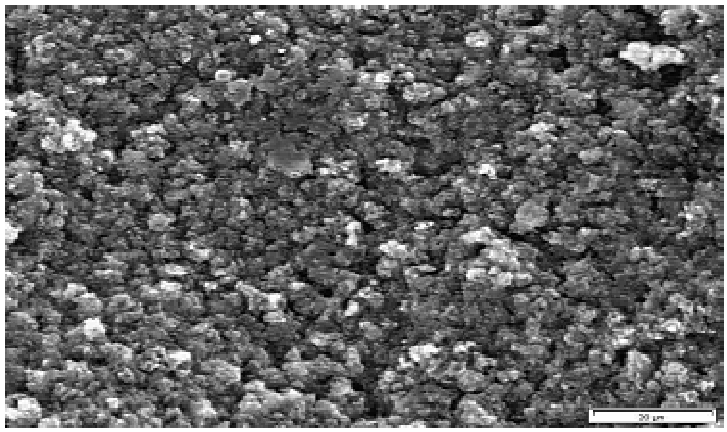

(a) Absent of an electrical field

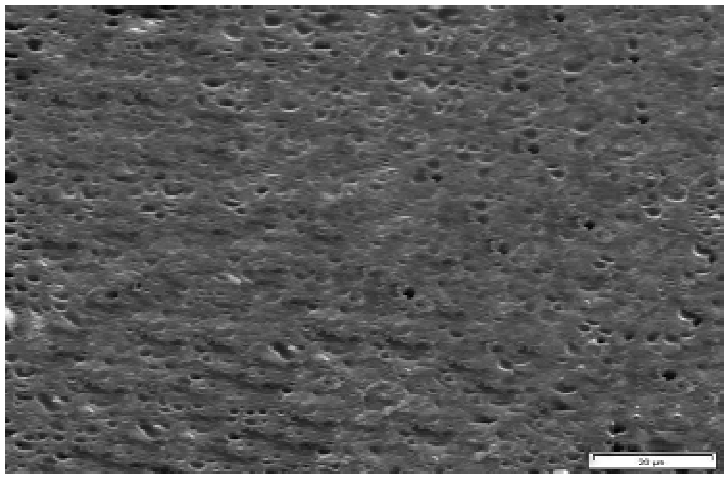

(b) Electrical field present

Figure 6. SEM images of P2EANi prepared in (a) absence and (b) presence electrical field.

is 2.3 and the mean weight of molecular mass is 193749 g/mol. This shows that the electric field has increased the molecular mass by a factor 2.3.

Electrical conductivity studies

The obtained polymer has a high purity because the excess initiator was readily washed with acetone. The purity was confirmed by elemental analysis. Conductivity of all samples were measured at room temperature by a four-probe method on pellets compressed at 700 MPa, 13 mm in diameter and 1 to 1.5 mm thick (Hosseini and Entezami, 2003; Hosseini et al., 2005, 2006). The 2-ethanol aniline was polymerized by using the four different initiators, such as APS, $FeCl_3.6H_2O$, KI and $FeSO_4$. For each initiator, the different dopants like HCl, $HClO_4$, H_2SO_4, AA, PTSA, MSA, DBSA and CSA were studied. Then the polymerization time for any initiator-dopant combination was changed from 30 to 120 min. In the next step, all experiments were repeated at different electric fields. The best molar ratio (monomer/initiator) experimentally was defined as 1/1. We used this ratio in all experiments. In all experiments, we focused on the obtained mass of polymer, m, electrical conduction of the obtained polymer in the absence of an electric field, σ, electrical conduction of the obtained polymer in the presence of an electric field, σ_E, and their ratio $r=\sigma_E/\sigma$. To identify the best molar ratio of APS initiator to monomer, values 1/0.5, 1/1 and 1/2 were examined by using HCl solution as dopant. The best electrical conduction was $\sigma=6\times10^{-3}$ S/cm for 1/1 ratio. Then to identify the best time of experiment, the polymerization was done for 1/1 molar ratio at different times such as 30, 45, 60, 90 and 120 min, and the best electrical conduction was $\sigma=9.5\times10^{-3}$ S/cm in 60 min. In this condition, the most obtained product mass was m=0.24 g too. Increasing the time does not affect the product mass, but it decreases the electrical conduction (Table 1 and Figure 7).

Table 1. Electrical conductivity of P2EANi produced by APS (HCl 1M) as initiator (1/1 mol ratio) in different times and absence of electric field.

Sample	Time of polymerization (min)	Color change time (min)	Weight of produced polymer (g)	Electrical conductivity ($\delta \times 10^{-3}$ S/cm)
1	30	5	0.21	2.4
2	45	5	0.23	5.9
3	60	5	0.24	9.5
4	90	5	0.24	9.1
5	120	5	0.25	8.8

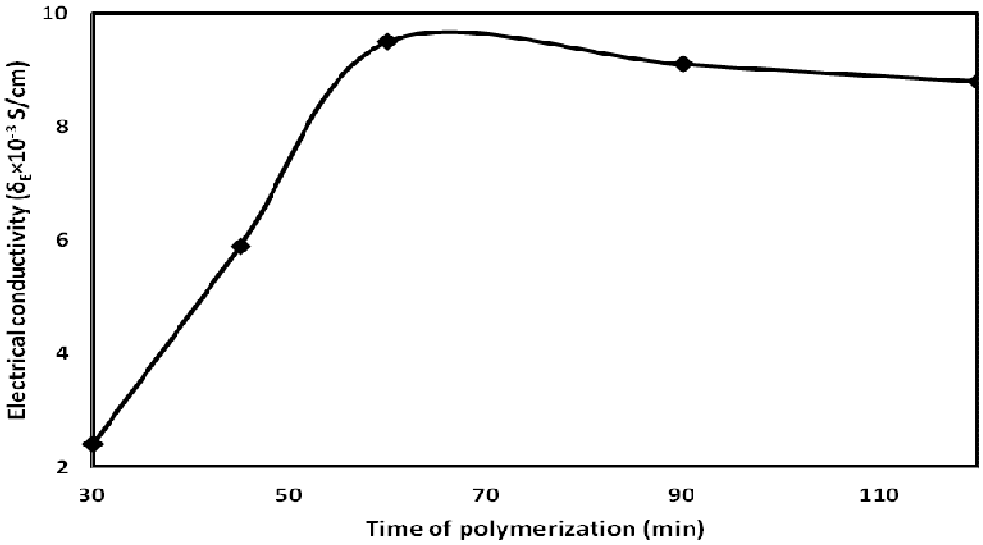

Figure 7. Electrical conductivity of P2EANi in different times and absence of electric field.

Table 2. Electrical conductivity of P2EANi produced by APS (HCl 1M) as initiator (1/1 mol ratio) in different electric field after 60 min.

Sample	Electric field (KN/C)	Color change time (min)	Weight of produced polymer (g)	Electrical conductivity ($\delta_E \times 10^{-3}$ S/cm)
1	35	6	0.21	22
2	69	7	0.28	87
3	104	7	0.29	85
4	138	8	0.28	74

In other experiments APS initiator and different dopants were used done with molar ratio of initiator to monomer, 1/1, in the 60 min, and the optimized condition under a uniform electric field with different intensities such as 5, 10, 15 and 20 KV/Cm^2. The most effective electric field intensity was 10 KV/Cm^2 in which we gained 0.28 g of product with $\sigma_E=87\times10^{-3}$ S/cm at Table 2 and Figure 8. On the other hand, we repeated the electrical conductivity of P2EANi produced by APS as an initiator and different dopants in the absence of the electric field and under 10 KV/Cm^2 one after 60 min. These results were summarized in Table 3.

In Table 3, we see that for all dopants without an electric field, the electrical conductivities are low while they are increased under electric field conductivities. Therefore, we also see that for APS initiator, the most effective dopants is DBSA with m=0.35 g, σ_E= 0.118 S/cm and r=7.87. So imposing the polymerization by a uniform electric field causes the electrical conduction improve by a factor 7.87. Then polymerization of 2-ethanol aniline at the optimized time (60 min) and with the best molar ratio initiator to monomer, (1/1), by using $FeCl_3.6H_2O$ as initiator, was done with different dopants in different electric field intensities. These results were compared with the ones obtained from incorporating polymer without applying electric field conditions. The results are

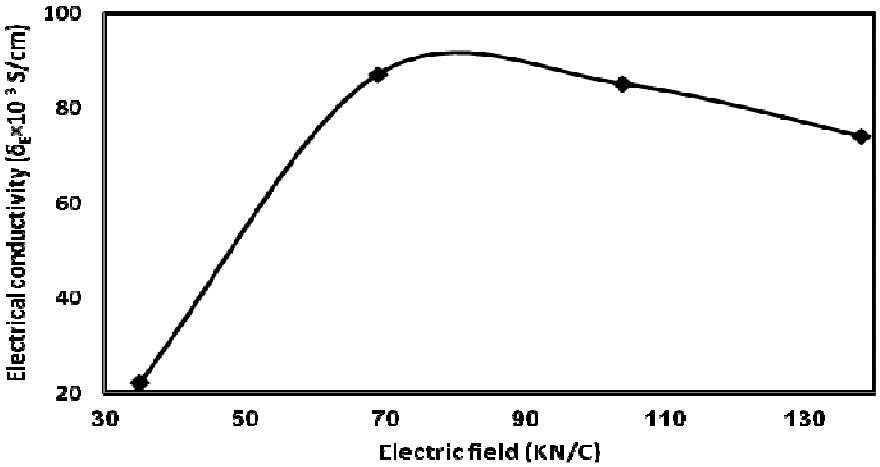

Figure 8. Electrical conductivity of P2EANi in different electric field after 60 min.

Table 3. Electrical conductivity of P2EANi produced by APS (HCl 1M) as initiator (1/1 mol ratio) with different dopants in absence and under 69 KN/C electric field after 60 min.

	Absence electric field		Under E=69 N/C		
Dopant (1M)	**Weight of produced polymer (g)**	**Electrical conductivity ($\delta \times 10^{-3}$ S/cm)**	**Weight of produced polymer (g)**	**Electrical conductivity ($\delta_E \times 10^{-3}$ S/cm)**	**r= δ_E/δ**
HCl	0.24	9.5	0.28	87	9.16
$HClO_4$	0.24	11	0.26	89	8.09
H_2SO_4	0.20	8.5	0.22	85	10.0
AA	0.18	2.1	0.21	15	7.14
MSA	0.24	4.5	0.24	42	9.33
PTSA	0.26	5.5	0.31	53	9.64
DBSA	0.29	15	0.35	118	7.87
CSA	0.27	11	0.31	105	9.54

Table 4. Electrical conductivity of P2EANi produced by $FeCl_3.6H_2O$ as initiator (1/1 mol ratio) different dopants in absence and under 69 KN/C electric field after 60 min.

	Absence electric field		Under E=69 N/C		
Dopant (1M)	**Weight of produced polymer (g)**	**Electrical conductivity ($\delta \times 10^{-3}$ S/cm)**	**Weight of produced polymer (g)**	**Electrical conductivity ($\delta_E \times 10^{-3}$ S/cm)**	**r= δ_E/δ**
HCl	0.22	4.5	0.23	22	4.88
$HClO_4$	0.22	5.5	0.24	25	4.54
H_2SO_4	0.21	3.0	0.23	22	7.33
AA	0.17	0.3	0.19	1.5	5.0
MSA	0.22	0.9	0.22	12	13.3
PTSA	0.23	6.0	0.23	21	3.50
DBSA	0.26	7.5	0.28	35	4.67
CSA	0.24	6.5	0.26	30	4.62

summarized in Table 4. Here we see that for $FeCl_3.6H_2O$ initiator, the best dopant is DBSA of which the best results are m=0.28g, $\sigma_E = 30 \times 10^{-3}$ S/cm and r=4.62. In addition, all described polymerizations were repeated by using KI as an initiator. The findings can be seen at Table 5. This table shows that for KI initiator, the best

Table 5. Electrical conductivity of P2EANi produced by KI as initiator (1/1 mol ratio) different dopants in absence and under 69 KN/C electric field after 60 min.

	Absence electric field		Under E=69 N/C		
Dopant (1M)	**Weight of produced polymer (g)**	**Electrical conductivity ($\delta\times10^{-3}$ S/cm)**	**Weight of produced polymer (g)**	**Electrical conductivity ($\delta_E\times10^{-3}$ S/cm)**	**r= δ_E/δ**
HCl	0.23	6.5	0.24	34	5.23
$HClO_4$	0.24	12	0.24	38	3.17
H_2SO_4	0.22	9.0	0.24	55	6.11
AA	0.19	2.5	0.21	3.0	1.20
MSA	0.23	6.5	0.24	18	2.77
PTSA	0.23	8.8	0.25	27	3.07
DBSA	0.27	19	0.30	55	2.89
CSA	0.27	25	0.31	60	2.4

Table 6. Electrical conductivity of P2EANi produced by $FeSO_4$ as initiator (1/1 mol ratio) different dopants in absence and under 69 KN/C electric field after 60 min.

	Absence electric field		Under E=69 N/C		
Dopant (1M)	**Weight of produced polymer (g)**	**Electrical conductivity ($\delta\times10^{-3}$ S/cm)**	**Weight of produced polymer (g)**	**Electrical conductivity ($\delta_E\times10^{-3}$ S/cm)**	**r= δ_E/δ**
HCl	0.21	2.5	0.22	15	6.0
$HClO_4$	0.22	5.5	0.24	25	4.54
H_2SO_4	0.23	5.5	0.24	25	4.54
AA	0.17	0.3	0.18	1.5	5.0
MSA	0.21	0.8	0.22	10	12.5
PTSA	0.22	5.5	0.23	13	2.36
DBSA	0.23	6.5	0.24	23	3.54
CSA	0.22	6.5	0.24	23	3.54

dopants are $HClO_4$, DBSA and CSA. The results of CSA are m=0.31 g, $\sigma_E=60\times10^{-3}$ S/cm and r=2.4. Finally, all above-described experiments were repeated by using $FeSO_4$ as an initiator. The results can be seen in Table 6. Table 6 shows $FeSO_4$ as initiator, and the best dopants are H_2SO_4, $HClO_4$ and DBSA. The results of DBSA are m=0.24g, $\sigma_E=23\times10^{-3}$ S/cm and r=3.54. In the experiments, we had 24 initiator–dopant combinations with widely different results. To compare the results, we collected all the best results (for initiator and dopant combination) in Table 7. This table shows all combinations in which conduction occurs, imposing electric field causes the electrical conduction to be improved. This also, shows that the best combination is APS-DBSA in which σ_E= 0.118 S/cm.

Conclusion

A molecule of 2-ethanol aniline is an electroactive monomer. It can be well polymerized through connecting the head to tail, and formed conductive polymer. They are head to head, tail to tail, or secondary connections. In this work, the electroactive monomers are arranged by using the electric field, and the head to tail connections are increased. Therefore, obtained polymer have a larger length chain, higher electrical conductivity, better space order and more appropriate physical resistance in comparison with the obtained one in the absence of electric field. The results of the experiments show that the electrical conductivity of produced P2EANi in different electric fields and the most constant time (60 min), increased with increasing intensity of electric field. But after 10 KV/Cm^2, the electrical conductivity has been decreased steadily.

Furthermore, the findings shows that the electrical conductivity of produced P2EANi in constant intensity of electric field – bout 10 KV/Cm^2– increases with increasing the amount of time. But after about 60 min, the electrical conductivity has been decreased steadily too.

On the other hand, considering the results of applying the various types of dopants and different initiators, the best initiator was APS, and the best dopant was dodecylbenzene sulfonic acid. It seems that by increasing

Table 7. Final results for any initiator–dopant combination.

Initiator	APS		$FeCl_3.6H_2O$		KI		$FeSO_4$	
Dopant	$\delta\times10^{-3}$	$\delta_E\times10^{-3}$	$\delta\times10^{-3}$	$\delta_E\times10^{-3}$	$\delta\times10^{-3}$	$\delta_E\times10^{-3}$	$\delta\times10^{-3}$	$\delta_E\times10^{-3}$
HCl	9.5	87	4.5	22	6.5	34	2.5	15
$HClO_4$	11	89	5.5	25	12	38	5.5	25
H_2SO_4	8.5	85	3.0	22	9.0	55	5.5	25
AA	2.1	15	0.3	1.5	2.5	3.0	0.3	1.5
MSA	4.5	42	0.9	12	6.5	18	0.8	10
PTSA	5.5	53	6.0	21	8.8	27	5.5	13
DBSA	15	118	7.5	35	19	55	6.5	23
CSA	11	105	6.5	30	25	60	6.5	23

the amount of time and intensity of the electric field after passing a special amount, the destructive processes in the polymer chain began as a result of increasing the length of polymer chain and dipolar moment forces. And also, due to polymeric confusion in the reaction solution, polymers involve defect reactions such as producing secondary branches on the polymer chain. Finally, mass and conductivity measurements of polymers showed that molecular weight and electric conductivity of the polymers were increased under electric field about 2 and 100 times, respectively.

REFERENCES

Buchachenko AL (2000). Mechanism of $Fe(OH)_2$ (aq) photolysis in aqueous solution, Pure Appl. Chem., 72:2243-2248.

Gato H, Akagi K, Itoh K (2001). Synthesis of liquid crystalline polyaniline derivatives and their orientational behaviors under magnetic field, Synth. Met., 117:91-93.

Hosseini SH (2006). Investigation of sensing effects of polystyrene-graft-polyaniline for cyanide compounds, J. Appl. Polym. Sci. 101(6):3920-3926.

Hosseini SH, Abdi Oskooe SH, Entezami AA (2005). Toxic Gas and Vapour Detection with Polyaniline Gas Sensors. Iranian Polym. J. 14(4):333-344.

Hosseini SH, Dabiri M, Ashrafi M (2006). Chemical and electrochemical synthesis of conducting graft copolymer of acrylonitrile with aniline, Polym. Int. 55(9):1081-1089.

Hosseini SH, Entezami AA (2003). Chemical and electrochemical synthesis of conducting poly di-heteroaromatics from pyrrole, indole, carbazole and their mixed containing hydroxamic acid groups and studies of its metal complexes, J. Appl. Polym. Sci., 90:63-71.

Hosseini SH, Mohammadi M (2009). Preparation and characterization of new poly-pyrrole having side chain liquid crystalline moieties, Mater. Sci. Eng. C, 29:1503-1509.

Hosseini SH, Noor P (2005). Ion exchange properties and kinetic behaviour of polyaniline-coated silica gel for p-toluenesulphonic acid and methanesulphonic acid, Iranian Polym. J. 14(1):55-60.

Li G, Zheng P, Wang NL, Long YZ, Chen ZJ, Li JC, Wan MX (2004). Optical study on doped polyaniline composite films, J. Phys. Condens. Matter., 16:6195–6204.

MacDiarmid AG (2001). A Conducting Composite of Polyaniline and Wood, Angew. Chem. Inst. Ed., 40:2581-2587.

Manoha SK, MacDiarmid AG, Epstein AJ (2002). Dependency of conductivity of selected doped conducting polymers on an unusual "Through space" electric field effect, Polymeric Materials: Sci. Eng. 86:1-5.

Pron A, Ranou P (2002). Processible conjugated polymers: from organic semiconductors organic metals and superconductors, Prog. Polym. Sci., 27:135-190.

Reits JR, Milford J, Christy RW (1979). Foundations of Electro Magnetic Theory, Third Edition Addison, Wesley.

Senadeera GKR, Pathirathne WMTC (2004). Utilization of conducting polymer as a sensitizer in solid-state photocells, Res. Communications-Current Sci. 87(3):339-342.

academicJournals

Vol. 8(22), pp. 1228-1245, 16 June, 2013
DOI: 10.5897/IJPS2013.3879
ISSN 1992-1950 © 2013 Academic Journals
http://www.academicjournals.org/IJPS

International Journal of Physical Sciences

Full Length Research Paper

A Mode-I crack problem for two-dimensional problem of a fiber-reinforced thermoelastic with normal mode analysis

Kh. Lotfy[1] and Wafaa Hassan[2,3]*

[1]Department of Mathematics, Faculty of Science, Zagazig University, Zagazig P. O. Box 44519 Egypt.
[2]Department of Mathematics and Physics, Faculty of Engineering, Port Said Branch of Suez Canal University, Port Said, Egypt.
[3]Department of Mathematics, Faculty of Science and Arts, Al-mithnab, Qassim University, P.O. Box 931, Buridah 51931, Al-mithnab, Kingdom of Saudi Arabia.

Accepted 12 April, 2013

The aim of the present work is to investigate the influence of the Mode-I crack on the plane waves in a linearly fiber-reinforced. A general model of the equations of coupled theory (CD) and Lord-Shulman (L-S) theory with one relaxation time are applied to study the influence of reinforcement on the total deformation for an infinite space weakened by a finite linear opening Mode-I crack is solving. The material is homogeneous isotropic elastic half space. The crack is subjected to prescribed temperature and stress distribution. The normal mode analysis is used to obtain the exact expressions for the displacement components, force stresses and temperature. The variations of the considered variables with the horizontal distance are illustrated graphically. Comparisons are made with the results in two theories. A comparison also is made between the two theories for different depths.

Key words: Fiber-reinforced, Lord-Shulman theory, Mode-I crack, normal mode analysis, thermoelasticity.

INTRODUCTION

Fiber-reinforced composites are widely used in engineering structures, due to their superiority over the structural materials in applications requiring high strength and stiffness in lightweight components. A continuum model is used to explain the mechanical properties of such materials. A reinforced concrete member should be designed for all conditions of stresses that may occur and in accordance with principles of mechanics. The characteristic property of a reinforced concrete member is that its components, namely concrete and steel, act together as a single unit as long as they remain in the elastic condition that is, the two components are bounded together so that there can be no relative displacement between them. In the case of an elastic solid reinforced by a series of parallel fibers, it is usual to assume transverse isotropy. In the linear case, the associated constitutive relations, relating infinitesimal stress and strain components have five material constants. In the last three decades, the analysis of stress and deformation of fibre-reinforced composite materials has been an important research area of solid mechanics. A reinforced concrete member shall be designed for all conditions of stresses that may occur and accordance with principle of mechanics. Fiber-reinforced composites are used in a variety of structures due to their low weight and high strength. The characteristic property of a reinforced composite is that its components act together as single anisotropic units as long as they remain in the

*Corresponding author. E-mail: khlotfy_1@yahoo.com.

elastic condition. The waves propagation in a reinforced media plays a very interesting role in civil engineering and geophysics. The studies of propagation, reflection and transmission of waves are of great interest to seismologists. Such studies help them to obtain knowledge about the rock structures as well as their elastic properties and at the same time information regarding minerals and fluids present inside the earth. The idea of introducing a continuous self reinforcement at every point of an elastic solid was given by Belfield et al. (1983). The model was later applied to the rotation of a tube by Verma (1986), who has also discussed the magneto elastic shear waves in self-reinforced bodies. Singh (2002) showed that, for wave propagation in fibre-reinforced anisotropic media, this decoupling cannot be achieved by the introduction of the displacement potential. Sengupta and Nath (2001) discussed the problem of the surface waves in fibre-reinforced anisotropic elastic media. Hashin and Rosen (1964) gave the elastic moduli for fibre-reinforced materials. The problem of reflection of plane waves at the free surface of a fibre-reinforced elastic half-space was discussed by Singh and Singh (2004). Chattopadhyay and Choudhury (1990) have discussed the problem of propagation, reflection and transmission of magneto elastic shear waves in a self–reinforced medium. The reflection and transmission of plane SH wave through a self-reinforced elastic layer sandwiched between two homogeneous visco-elastic solid half-spaces has been studied by Chaudhary et al. (2004). Chattopadhyay and Choudhury (1995) studied the propagation of magneto-elastic shear waves in an infinite self-reinforced plate. Pradhan et al. (2003) studied the dispersion of Loves waves in a self-reinforced layer over an elastic non-homogenous half space. The propagation of plane waves in fibre-reinforced media is discussed by Chattopadhyay et al. (2002). The theory of couple thermo-elasticity was extended by Lord and Şhulman (1967) and Green and Lindsay (1972) by including the thermal relaxation time in constitutive relations.

Othman and Song (2007) showed the effect of initial stress, thermoelastic parameter and thermal boundary condition upon the reflection amplitude ratios. The problem of magneto-elastic transverse surfaces waves in self-reinforced elastic solid was studied by Verma et al. (1988). The problem of wave propagation in thermally conducting linear fibre-reinforced composite materials was discussed by Singh (2006).

Othman and Lotfy (2009) studied two-dimensional problem of generalized magneto-thermoelasticity under the effect of temperature dependent properties. Othman et al. (2009) studied transient disturbance in a half-space under generalized magneto-thermoelasticity with moving internal heat source. Othman and Lotfy (2010) studied the plane waves in generalized thermo -microstretch elastic half-space by using a general model of the equations of generalized thermo-microstretch for a homogeneous isotropic elastic half space. Othman and Lotfy (2009) studied the generalized thermo-microstretch elastic medium with temperature dependent properties for different theories. Othman and Lotfy (2010) studied the effect of magnetic field and inclined load in micropolar thermoelastic medium possessing cubic symmetry under three theories. The normal mode analysis was used to obtain the exact expression for the temperature distribution, thermal stresses, and the displacement components.

The investigation of interaction between a magnetic field, stress, and strain in a thermoelastic solid is very important due to its many applications in diverse field, such as geophysics (for understanding the effect of the Earth's magnetic field on seismic waves), damping of acoustic waves in a magnetic field, designing machine elements like heat exchangers, boiler tubes where the temperature induced elastic deformation occurs, biomedical engineering (problems involving thermal stress), emissions of the electromagnetic radiations from nuclear devices, development of a highly sensitive super conducting magnetometer, electrical power engineering plasma physics etc. (Lotfy, 2012a, b). The problem has been solved numerically using the normal mode analysis and many works in generalized magneto-thermo elasticity with effect of rotation and other fields can be found in (Othman and Saied, 2012a, b; 2013a, b; Othman and Atwa, 2012) for a half space fiber-reinforced. Numerical results for the conductive temperature, thermodynamic temperature, displacement components and the stresses are represented graphically and the results are analyzed.

In the recent years, considerable efforts have been devoted the study of failure and cracks in solids. This is due to the application of the latter generally in industry and particularly in the fabrication of electronic components. Most of the studies of dynamical crack problem are done using the equations of coupled or even uncoupled theories of thermoelasticity (Dhaliwal, 1980; Hasanyan et al., 2005; Ueda, 2003; Elfalaky and Abdel-Halim, 2006). This is suitable for most situations where long time effects are sought. However, when short time are important, as in many practical situations, the full system of generalized thermoelastic equations must be used (Lord and Şhulman, 1967).

In the present work we shall formulate the fiber-reinforced two-dimensional problem of thermally for an infinite space weakened by a finite linear opening Mode-I crack is solving for the considered variables. The normal mode method is used to obtain the exact expressions for the considered variables. The distributions of the considered variables are represented graphically. A comparison is carried out between the temperature, stresses and displacements as calculated from the generalized thermoelasticity L-S and coupled theories for half space fiber-reinforced in two problems. A comparison also is made between the two theories for different depths.

FORMULATION OF THE PROBLEM AND BASIC EQUATIONS

We shall consider the problem of a homogeneous, isotropic and linearly fiber-reinforced thermoelastic half-space ($x \geq 0$). The constitutive equations for a fibre-reinforced linearly elastic anisotropic medium with respect to the reinforcement direction 'a' are (Belfield et al., 1983):

$$\sigma_{ij} = \lambda e_{kk}\delta_{ij} + 2\mu_T e_{ij} + \alpha(a_k a_m e_{km}\delta ij + a_i a_j e_{kk}) + 2(\mu_L - \mu_T)(a_i a_k e_{kj} + a_j a_k e_{ki}) + \beta a_k a_m e_{km} a_i a_j - \gamma(T - T_0)\delta_{ij}. \quad (1)$$

Where σ_{ij} are components of stress; e_{ij} are the components of strain; λ, μ_T are elastic constants; $\alpha, \beta, (\mu_L - \mu_T)$ are reinforcement parameters, $\gamma = (3\lambda + 2\mu)\alpha_t$, α_t thermal expansion coefficient and $\underline{a} \equiv (a_1, a_2, a_3), \quad a_1^2 + a_2^2 + a_3^2 = 1.$ We choose the fiber-direction as $\underline{a} \equiv (1,0,0).$ The strains can be expressed in terms of the displacement u_i as:

$$e_{ij} = \frac{1}{2}(u_{i,j} + u_{j,i}). \quad (2)$$

For plane strain deformation in the xy-plane [displacement $\underline{u} = (u, v, 0)$] $\frac{\partial}{\partial z} = 0$, $w = 0$ .Equation (1) then yields

$$\sigma_{xx} = A_{11}u_{,x} + A_{12}v_{,y} - \gamma(T - T_0), \quad (3)$$

$$\sigma_{yy} = A_{22}v_{,y} + A_{12}u_{,x} - \gamma(T - T_0), \quad (4)$$

$$\sigma_{zz} = A_{12}u_{,x} + \lambda v_{,y} - \gamma(T - T_0), \quad (5)$$

$$\sigma_{xy} = \mu_L(u_{,y} + v_{,x}), \qquad \sigma_{zx} = \sigma_{zy} = 0. \quad (6)$$

Where

$$A_{11} = \lambda + 2(\alpha + \mu_T) + 4(\mu_L - \mu_T) + \beta, \qquad A_{12} = \alpha + \lambda,$$
$$A_{22} = \lambda + 2\mu_T. \quad (7)$$

The equation of motion in a rotating frame of reference in the context of Lord-Shulman's(LS) theory is

$$\rho\ddot{u}_i = \sigma_{ij,j}, \quad (i, j = 1,2,3). \quad (8)$$

The heat conduction equation

$$kT_{,ii} = \left(\frac{\partial}{\partial t} + \tau_0 \frac{\partial^2}{\partial t^2}\right)(\rho C_E T + \gamma T_0 u_{i,i}). \quad (9)$$

Where ρ is the density, k is the thermal conductivity, C_E is specific heat at constant strain and T is temperature above reference temperature T_0.

Using the summation convection. From Equations (3) to (6), we note that the third equation of motion in Equation (8) identically satisfied and first two equations become:

$$\rho\left(\frac{\partial^2 u}{\partial t^2}\right) = A_{11}\frac{\partial^2 u}{\partial x^2} + B_2\frac{\partial^2 v}{\partial x \partial y} + B_1\frac{\partial^2 u}{\partial y^2} - \gamma\frac{\partial T}{\partial x}, \quad (10)$$

$$\rho\left(\frac{\partial^2 v}{\partial t^2}\right) = A_{22}\frac{\partial^2 v}{\partial y^2} + B_2\frac{\partial^2 u}{\partial x \partial y} + B_1\frac{\partial^2 v}{\partial x^2} - \gamma\frac{\partial T}{\partial y}. \quad (11)$$

Where $B_1 = \mu_L, \qquad B_2 = \alpha + \lambda + \mu_L.$

For convenience, the following non-dimensional variables are used:

$$x' = c_1\eta x, \quad y' = c_1\eta y, \quad u' = c_1\eta u, \quad v' = c_1\eta v, \quad t' = c_1^2\eta t, \quad \tau_0' = c_1^2\eta\tau_0,$$
$$\Omega' = \frac{\Omega}{c_1^2\eta}, \quad \theta = \gamma\frac{(T - T_0)}{\lambda + 2\mu_T}, \quad \sigma_{ij}' = \frac{\sigma_{ij}}{\mu_T}. \quad i, j = 1,2. \quad (12)$$

Where $\eta = \frac{\rho C_E}{k}, \qquad c_1^2 = \frac{\lambda + 2\mu_T}{\rho}.$

In terms of non-dimensional quantities defined in Equation (12), the above governing equations reduce to (dropping the dashed for convenience)

$$\frac{\partial^2 u}{\partial t^2} = h_{11}\frac{\partial^2 u}{\partial x^2} + h_2\frac{\partial^2 v}{\partial x \partial y} + h_1\frac{\partial^2 u}{\partial y^2} - \frac{\partial \theta}{\partial x}, \quad (13)$$

$$\frac{\partial^2 v}{\partial t^2} = h_{22}\frac{\partial^2 v}{\partial y^2} + h_2\frac{\partial^2 u}{\partial x \partial y} + h_1\frac{\partial^2 v}{\partial x^2} - \frac{\partial \theta}{\partial y}, \quad (14)$$

$$\frac{\partial^2 \theta}{\partial x^2} + \frac{\partial^2 \theta}{\partial y^2} = \left(\frac{\partial}{\partial t} + \tau_0\frac{\partial^2}{\partial t^2}\right)\left(\theta + \varepsilon\left(\frac{\partial u}{\partial x} + \frac{\partial v}{\partial y}\right)\right). \quad (15)$$

Where

$$(h_{11}, h_{22}, h_1, h_2) = \frac{(A_{11}, A_{22}, B_1, B_2)}{(\lambda + 2\mu_T)}, \qquad \varepsilon = \frac{\gamma^2 T_0}{\rho C_E(\lambda + 2\mu_T)}.$$

$$\mu_T\sigma_{xx} = A_{11}u_{,x} + A_{12}v_{,y} - (\lambda + 2\mu_T)\theta, \quad (16)$$

$$\mu_T\sigma_{yy} = A_{22}v_{,y} + A_{12}u_{,x} - (\lambda + 2\mu_T)\theta, \quad (17)$$

$$\mu_T\sigma_{zz} = A_{12}u_{,x} + \lambda v_{,y} - (\lambda + 2\mu_T)\theta, \quad (18)$$

$$\mu_T\sigma_{xy} = \mu_L(u_{,y} + v_{,x}), \qquad \sigma_{zx} = \sigma_{zy} = 0. \quad (19)$$

NORMAL MODE ANALYSIS

The normal mode analysis gives exact solutions without any assumed restrictions on temperature, displacement and stress distributions. It is applied to a wide range of problems in different branches. It can be applied to boundary-layer problems, which are described by the linearized Navier-Stokes equations in electro hydrodynamics. The normal mode analysis is, in fact, to look for the solution in Fourier transformed domain. Assuming that all the field quantities are sufficiently smooth on the real line such that normal mode analysis of these functions exists. The solution of the considered physical variable can be decomposed in terms of normal modes as the following form:

$$[u,v,\theta,\sigma_{ij}](x,y,t)=[u^*(x),v^*(x),\theta^*(x),\sigma^*_{ij}(x)]\exp(\omega t+iay). \tag{20}$$

Where ω is the (complex) time constant. $i=\sqrt{-1}$, a is the wave number in the $y-$ direction and $u^*(x),v^*(x),\theta^*(x)$ and $\sigma^*_{ij}(x)$ are the amplitude of the field quantities. Using Equation (20), then Equations (13) to (19) take the form

$$[h_{11}D^2-A_1]u^*+[iah_2D]v^*=D\theta^*, \tag{21}$$

$$[h_1D^2-A_2]v^*+[iah_2D]u^*=ia\theta^*, \tag{22}$$

$$A_4Du^*+iaA_4]v^*=[D^2-A_3]\theta^*, \tag{23}$$

$$\mu_T\sigma^*_{xx}=A_{11}Du^*+iaA_{12}v^*-(\lambda+2\mu_T)\theta^*, \tag{24}$$

$$\mu_T\sigma^*_{yy}=A_{12}Du^*+iaA_{22}v^*+-(\lambda+2\mu_T)\theta^*, \tag{25}$$

$$\mu_T\sigma^*_{zz}=A_{12}Du^*+ia\lambda v^*-(\lambda+2\mu_T)\theta^*, \tag{26}$$

$$\mu_T\sigma^*_{xy}=\mu_L(iau^*+Dv^*), \qquad \sigma^*_{zx}=\sigma^*_{zy}=0. \tag{27}$$

Where

$$A_1=\omega^2+h_1a^2, \qquad A_2=\omega^2+h_{22}a^2,$$

$$A_3=a^2+\omega+\omega^2\tau_0, \qquad A_4=\omega\varepsilon+\varepsilon\omega^2\tau_0, \qquad D=\frac{d}{dx}$$

Eliminating $\theta^*(x)$ and $v^*(x)$ between Equations (21) to (23), we obtain the ordinary differential equation satisfied by $u^*(x)$.

$$[D^6-AD^4+BD^2-C]u^*(x)=0. \tag{28}$$

where

$$A=\frac{1}{h_1h_{11}}\{h_{11}A_2+h_1A_1+h_1A_4+h_1h_{11}A_3-h_2^2a^2\}, \tag{29}$$

$$B=\frac{1}{h_1h_{11}}\{A_1A_2+h_{11}A_2A_3+h_1A_1A_3+h_{11}a^2A_4+A_2A_4-h_2^2a^2A_3-2h_2a^2A_4\}, \tag{30}$$

$$C=\frac{1}{h_1h_{11}}\{A_1A_2A_3+A_1A_4a^2\}. \tag{31}$$

In a similar manner, we get

$$[D^6-AD^4+BD^2-C]\{v^*(x),\theta^*(x)\}=0. \tag{32}$$

The above equation can be factorized as

$$(D^2-k_1^2)(D^2-k_2^2)(D^2-k_3^2)u^*(x)=0, \tag{33}$$

where, $k_n^2\,(n=1,2,3)$ are the roots of the following characteristic equation

$$k^6-Ak^4+Bk^2-C=0.. \tag{34}$$

The solution of Equation (33) which is bounded as $x\to\infty$, is given by

$$u^*(x)=\sum_{n=1}^{3}M_n(a,\omega)\exp(-k_nx) \tag{35}$$

Similarly

$$v^*(x)=\sum_{n=1}^{3}M'_n(a,\omega)\exp(-k_nx) \tag{36}$$

$$\theta^*(x)=\sum_{n=1}^{3}M''_n(a,\omega)\exp(-k_nx) \tag{37}$$

Where M_n, M'_n and M''_n are some parameters depending on a and ω.

Substituting from Equations (35) to (37) into Equations (21) to (23), we have

$$M'_n(a,\omega)=H_{1n}M_n(a,\omega), \qquad n=1,2,3. \tag{38}$$

$$M''_n(a,\omega)=H_{2n}M_n(a,\omega), \qquad n=1,2,3. \tag{39}$$

Where

$$H_{1n}=\frac{-iah_{11}k_n^2+iaA_1+iah_2k_n^2}{h_2k_na^2+h_1k_n^3-A_2k_n}, \qquad n=1,2,3. \tag{40}$$

$$H_{2n}=\frac{-A_4k_n+iaA_4H_{1n}}{k_n^2-A_3}, \qquad n=1,2,3. \tag{41}$$

Thus, we have

$$v^*(x) = \sum_{n=1}^{3} H_{1n} M_n(a,\omega) \exp(-k_n x) \tag{42}$$

$$\theta^*(x) = \sum_{n=1}^{3} H_{2n} M_n(a,\omega) \exp(-k_n x) \tag{43}$$

Substitution of Equations (35), (42) and (43) into Equations (24) to(27), we get

$$\mu_T \sigma_{xx}^* = \sum_{n=1}^{3} H_{3n} M_n(a,\omega) \exp(-k_n x), \tag{44}$$

$$\mu_T \sigma_{yy}^* = \sum_{n=1}^{3} H_{4n} M_n(a,\omega) \exp(-k_n x), \tag{45}$$

$$\mu_T \sigma_{zz}^* = \sum_{n=1}^{3} H_{5n} M_n(a,\omega) \exp(-k_n x), \tag{46}$$

$$\mu_T \sigma_{xy}^* = \sum_{n=1}^{3} H_{6n} M_n(a,\omega) \exp(-k_n x), \tag{47}$$

where

$$H_{3n} = -A_{11} k_n + ia A_{12} H_{1n} - (\lambda + 2\mu_T) H_{2n} \qquad n = 1,2,3. \tag{48}$$

$$H_{4n} = -A_{12} k_n + ia A_{22} H_{1n} - (\lambda + 2\mu_T) H_{2n} \qquad n = 1,2,3. \tag{49}$$

$$H_{5n} = -A_{12} k_n + ia\lambda H_{1n} - (\lambda + 2\mu_T) H_{2n} \qquad n = 1,2,3. \tag{50}$$

$$H_{6n} = \mu_L (ia - k_n H_{1n}) \qquad n = 1,2,3. \tag{51}$$

The normal mode analysis is, in fact, to look for the solution in Fourier transformed domain. Assuming that all the field quantities are sufficiently smooth on the real line such that normal mode analysis of these functions exists.

APPLICATION

Problem 1 (A Mode-I crack)

The plane boundary subjects to an instantaneous normal point force and the boundary surface is isothermal, the boundary conditions (Figure 1) at the vertical plan $y = 0$ and in the beginning of the crack at $x = 0$ are

$$\sigma_{yy}(x,y,t) = -p(y,t), \quad |x| < a \tag{52}$$

$$\theta(x,y,t) = f(y,t) \qquad |x| < a \text{ and } \frac{\partial \theta}{\partial y} = 0 \qquad |x| > a \tag{53}$$

$$\sigma_{xy}(x,y,t) = 0 \qquad -\infty < x < \infty \tag{54}$$

Substituting the expressions of the variables considered into the above boundary conditions, we get

$$\sum_{n=1}^{3} H_{3n} M_n(a,\omega) = -p^*(y,t) \tag{55}$$

$$\sum_{n=1}^{3} H_{2n} M_n(a,\omega) = f^*(y,t) \tag{56}$$

$$\sum_{n=1}^{3} H_{6n} M_n(a,\omega) = 0 \tag{57}$$

Invoking the boundary conditions (55) to (57) at the surface $x = 0$ of the plate, we obtain a system of three equations. After applying the inverse of matrix method, we have the values of the three constants $M_j,\ j = 1,2,3$. Hence, we obtain the expressions of displacements, temperature distribution and another physical quantities of the plate the muscles.

$$\begin{pmatrix} M_1 \\ M_2 \\ M_3 \end{pmatrix} = \begin{pmatrix} H_{41} & H_{42} & H_{43} \\ H_{21} & H_{22} & H_{23} \\ H_{61} & H_{62} & H_{63} \end{pmatrix}^{-1} \begin{pmatrix} -p^* \\ f^* \\ 0 \end{pmatrix} \tag{58}$$

Problem 2

A time-dependent heat punches across the surface of semi-infinite thermo-elastic half space. In the physical problem, we should suppress the positive exponential that are unbounded at infinity. The constants $M_1, M_2 \text{ and } M_3$ have to be chosen such that the boundary conditions on the surface x = 0 take the form

(1) Thermal boundary condition that the surface of the half-space subjected to a

$$\theta(0,y,t) = 0 \quad \text{on} \quad x = 0, \tag{59}$$

(2) Thermal boundary condition that the surface of the half-space subjected to a

$$\sigma_{xx}(0,y,t) = -p_1(y,t) \quad \text{on} \quad x = 0, \tag{60}$$

$$\sigma_{xy}(0,y,t) = 0 \quad \text{on} \quad x = 0. \tag{61}$$

where p is given function of y and t. Invoking the boundary conditions (59 to 61) at the surface $x = 0$ of the plate, we obtain a system of three equations. After applying the inverse of matrix method, we have the values of the three constants $M_j,\ j = 1,2,3$.

$$\begin{pmatrix} M_1 \\ M_2 \\ M_3 \end{pmatrix} = \begin{pmatrix} H_{31} & H_{32} & H_{33} \\ H_{21} & H_{22} & H_{23} \\ H_{61} & H_{62} & H_{63} \end{pmatrix}^{-1} \begin{pmatrix} 0 \\ -p_1 \\ 0 \end{pmatrix} \tag{62}$$

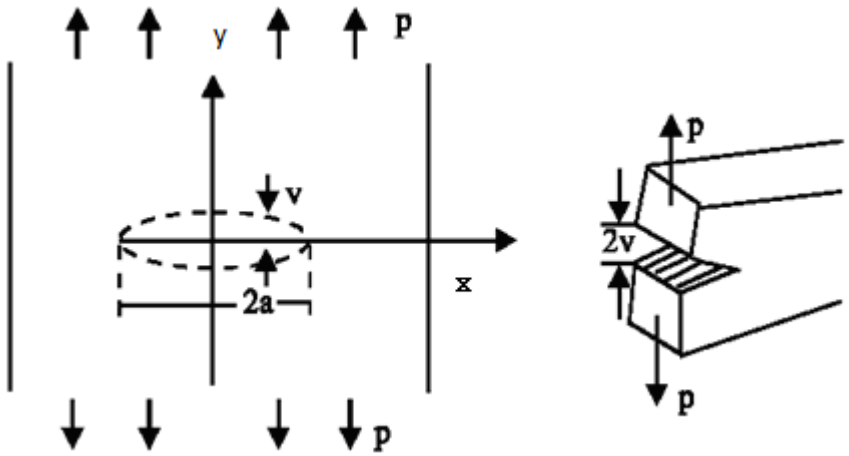

Figure 1. Displacement of an external Mode-I crack.

From this matrix we obtain the values of the three constants M_1, M_2 and M_3. Hence, we obtain the expressions of displacements, force stress, coupled stress and temperature distribution for generalized thermoelastic medium.

NUMERICAL RESULTS

In order to illustrate the theoretical results obtained in preceding section, to compare these in the context of various theories of thermoelasticity and reinforcement on wave propagation. We now present some numerical results for the physical constants. We now present some numerical results for the physical constants (Singh and Singh, 2004).

$\lambda = 7.59\text{x}10^9\ N/m^2$, $\mu_T = 1.89\text{x}10^9\ N/m^2$, $\mu_L = 2.45\text{x}10^9\ N/m^2$,
$\alpha = -1.28\text{x}10^9\ N/m^2$, $\beta = 0.32\text{x}10^9\ N/m^2$, $\rho = 7800 kg/m^2$,
$\alpha_t = 1.78\ \text{x}10^{-5}\ N/m^2$, $k = 386$, $C_E = 383.1$, $\tau_0 = 0.02$,
$a = 1$
$T_0 = 293\text{k}$ $f^* = 1$, $p^* = 2$, $\omega = \omega_0 + i\xi$ $\omega_0 = 2$,
$\xi = 1$
$C_E = 383.1$ $J/(kgk)$, $\mu = 3.86\times10^{10}$ kg/ms^2

The computations were carried out for a value of time $t = 0.1$. The numerical technique, outlined above, was used for the distribution of the real part of the thermal temperature θ, the displacement u and v, the stresses σ_{xx}, σ_{yy}, σ_{zz} and σ_{xy} distribution for the problem. The field quantities, temperature, displacement components u, v and stress components σ_{xx}, σ_{yy}, σ_{zz} and σ_{xy} depend not only on space x and time t but also on the thermal relaxation time τ_0. Here all the variables are taken in non dimensional forms.

The results are shown in Figures 1 to 14. The graph shows the two curves predicted by different theories of thermoelasticity. In these figures, the solid lines represent the solution in the coupled theory; the dashed lines represent the solution in the generalized Lord and Shulman theory. We notice that the results for the temperature, the displacement and stresses distribution when the relaxation time is including in the heat equation are distinctly different from those when the relaxation time is not mentioned in heat equation, because the thermal waves in the Fourier's theory of heat equation travel with an infinite speed of propagation as opposed to finite speed in the non-Fourier case. This demonstrates clearly the difference between the coupled and the theory of thermoelasticity (LS).

Problem 1

For the value of y, namely y = -1, were substituted in performing the computation. It should be noted (Figure 2) that in this problem I, the crack's size, x is taken to be the length in this problem so that $0 \le x \le 1.2$, $y = 0$ represents the plane of the crack that is symmetric with respect to the y -plane. It is clear from the graph that θ has a maximum value at the beginning of the crack ($x = 0$), it begins to fall just near the crack edge ($\text{x} \approx 1.2$), where it experiences sharp decreases (with a maximum negative gradient at the crack's end). The value of temperature quantity converges to zero with increasing the distance x.

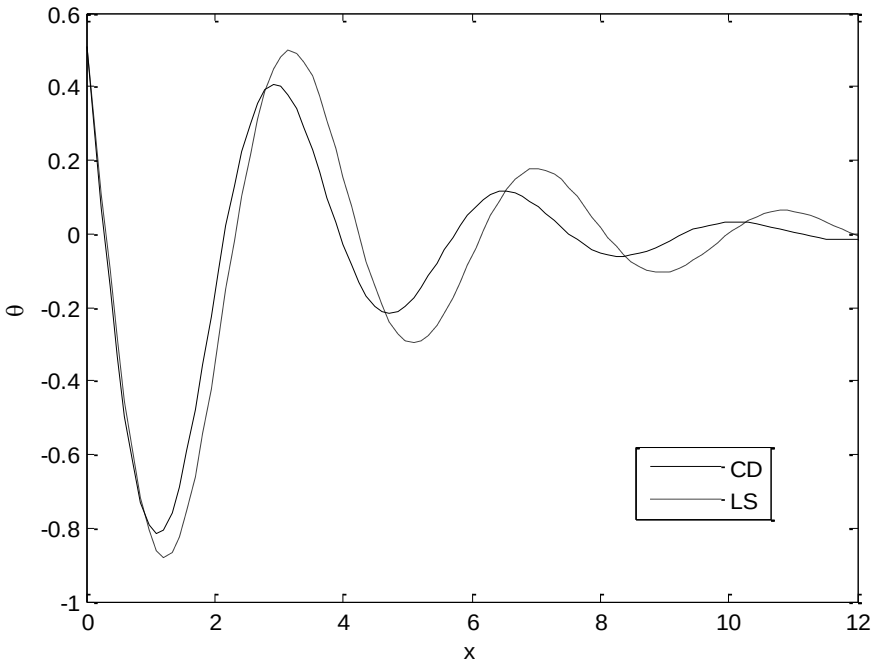

Figure 2. The temperature distribution for problem 1.

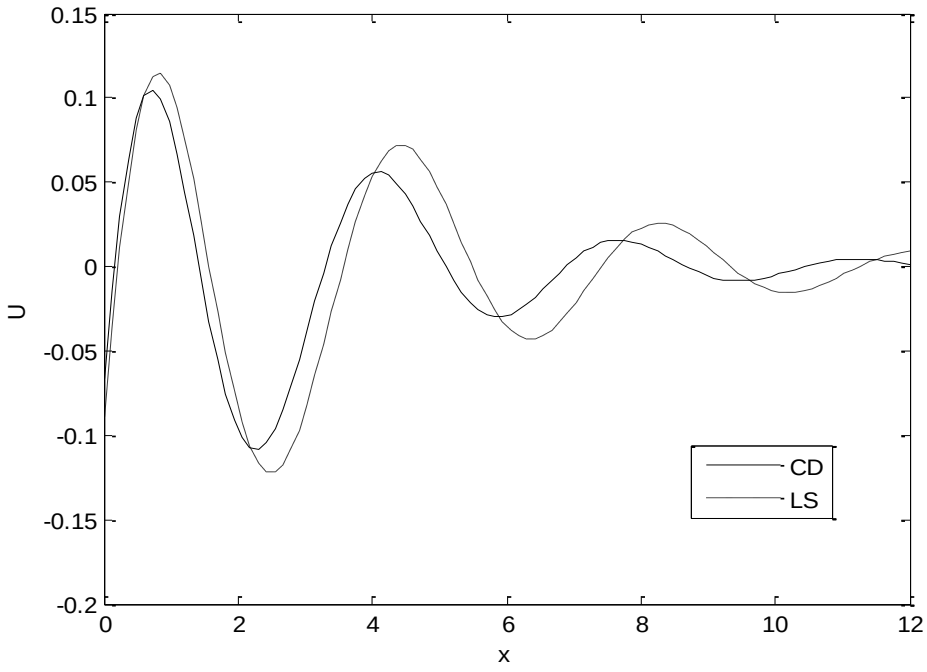

Figure 3. Horizontal displacement distribution u for problem 1.

Figure 3 the horizontal displacement, u begins with increases near the crack edge ($x \approx 1.2$), then smooth decreases again to reach its minimum magnitude just at the crack end. Beyond it u falls again to try to retain zero at infinity. Figure 4, the vertical displacement V, we see that the displacement component V always starts from the negative value and terminates at the zero value. Also, at the crack end to reach minimum value, beyond

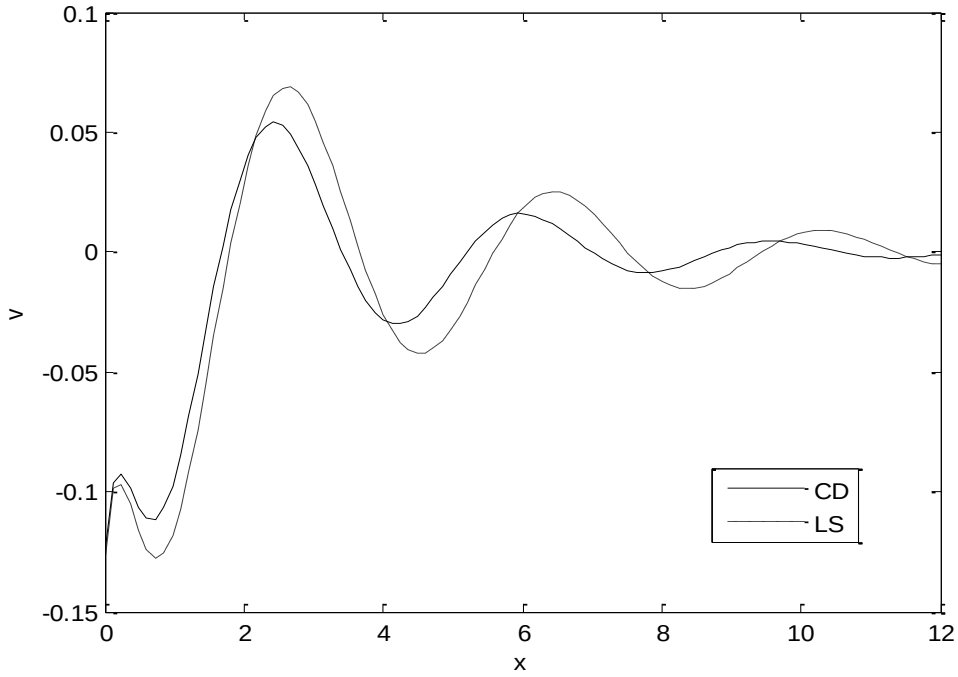

Figure 4. Vertical displacement distribution v for problem 1.

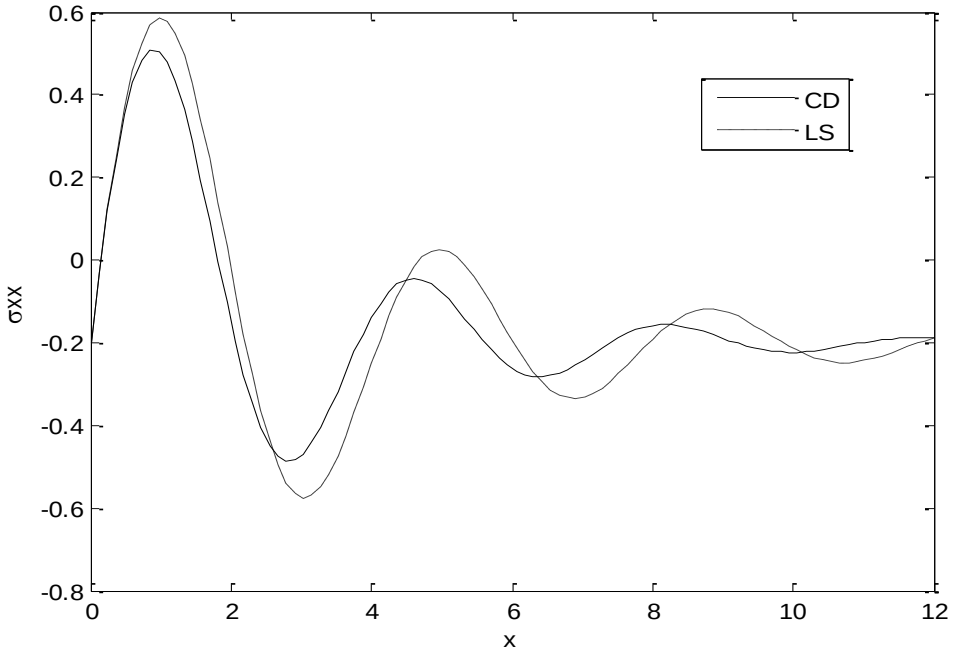

Figure 5. The distribution of stress component σ_{xx} for problem 1.

reaching zero at the three double of the crack size (state of particles equilibrium). The displacements u and v show different behaviours, because of the elasticity of the solid tends to resist vertical displacements in the problem under investigation. Both of the components show different behaviours, the former tends to increase to maximum just before the end of the crack. Then it falls to a minimum with a highly negative gradient. Afterwards it

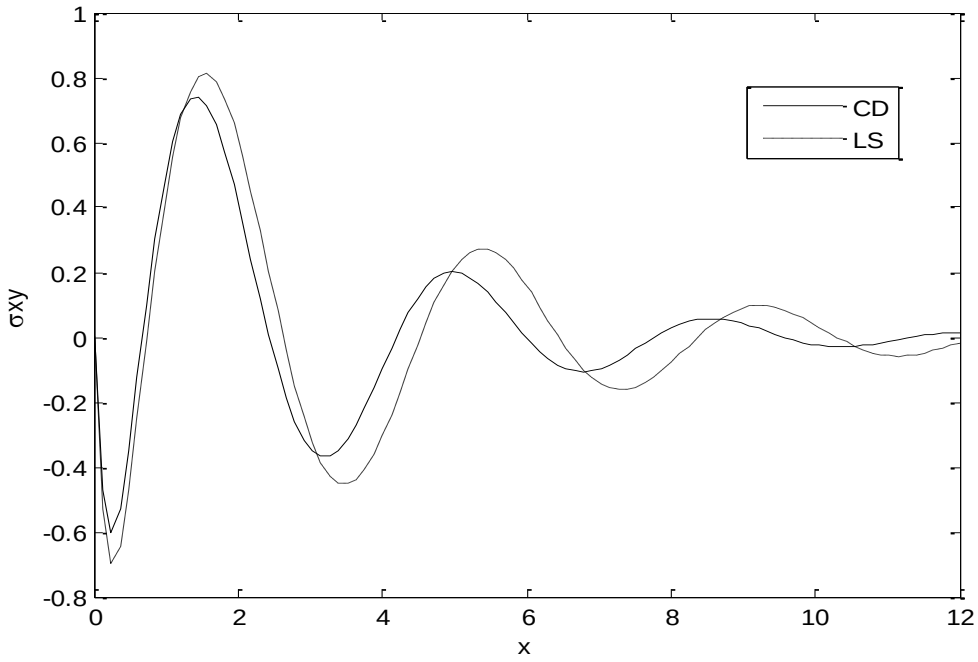

Figure 6. The distribution of stress component σ_{xy} for problem 1.

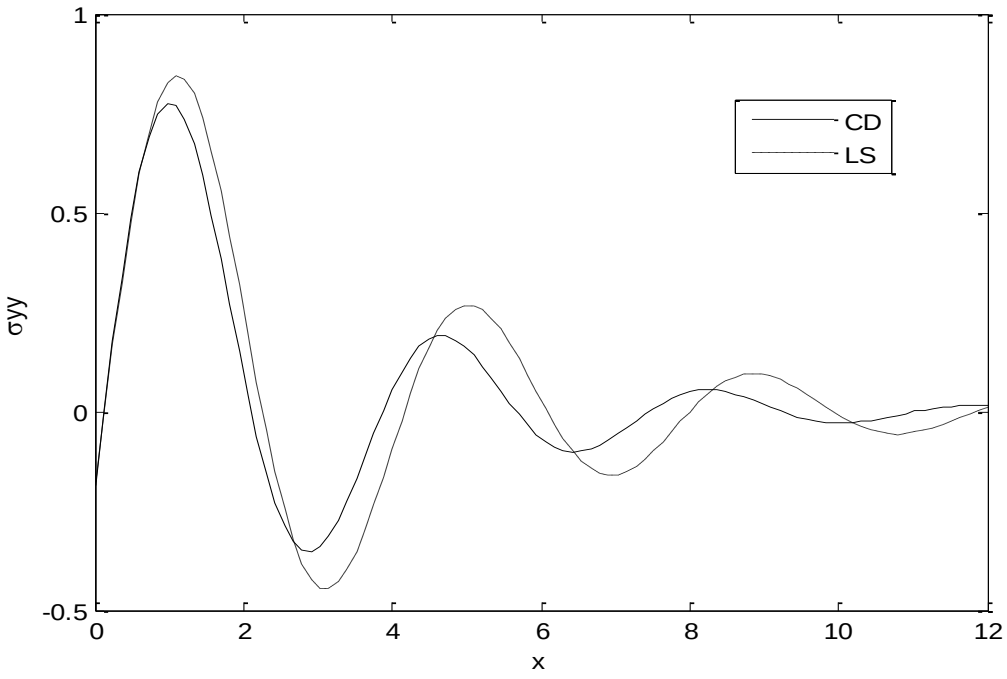

Figure 7. The distribution of stress component σ_{yy} for problem 1.

rises again to a maximum beyond about the crack end.

The stress component, σ_{xx} reach coincidence with negative value (Figure 5) and satisfy the boundary condition at $x=0$, reach the maximum value near the end of crack ($x \approx 1.2$) and converges to zero with increasing the distance x, also Figure 7 (satisfy the

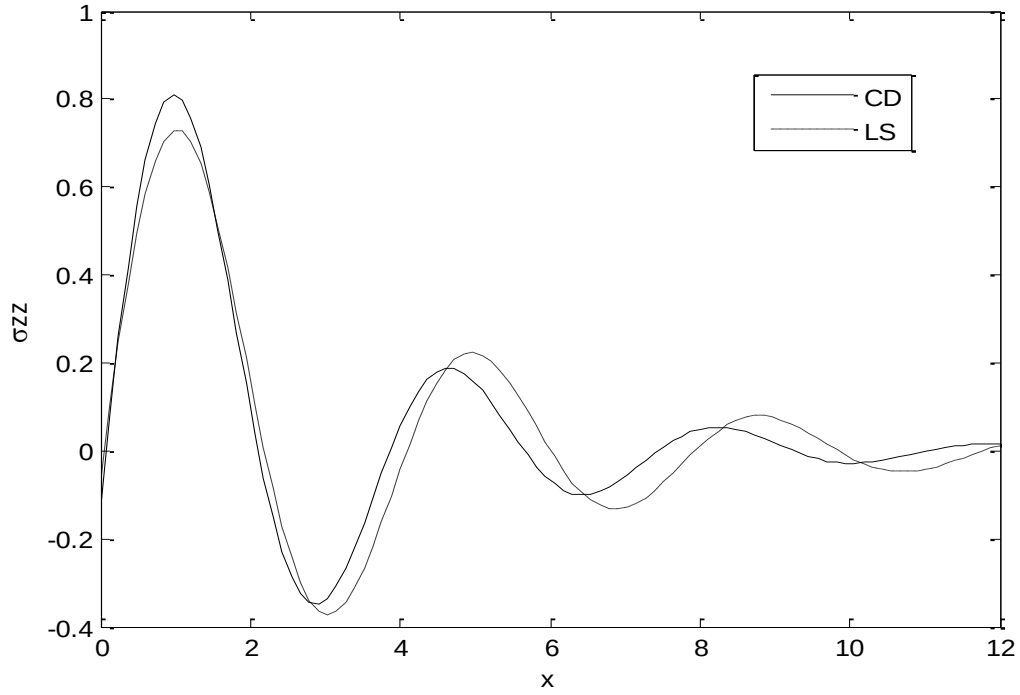

Figure 8. The distribution of stress component σ_{zz} for problem 1.

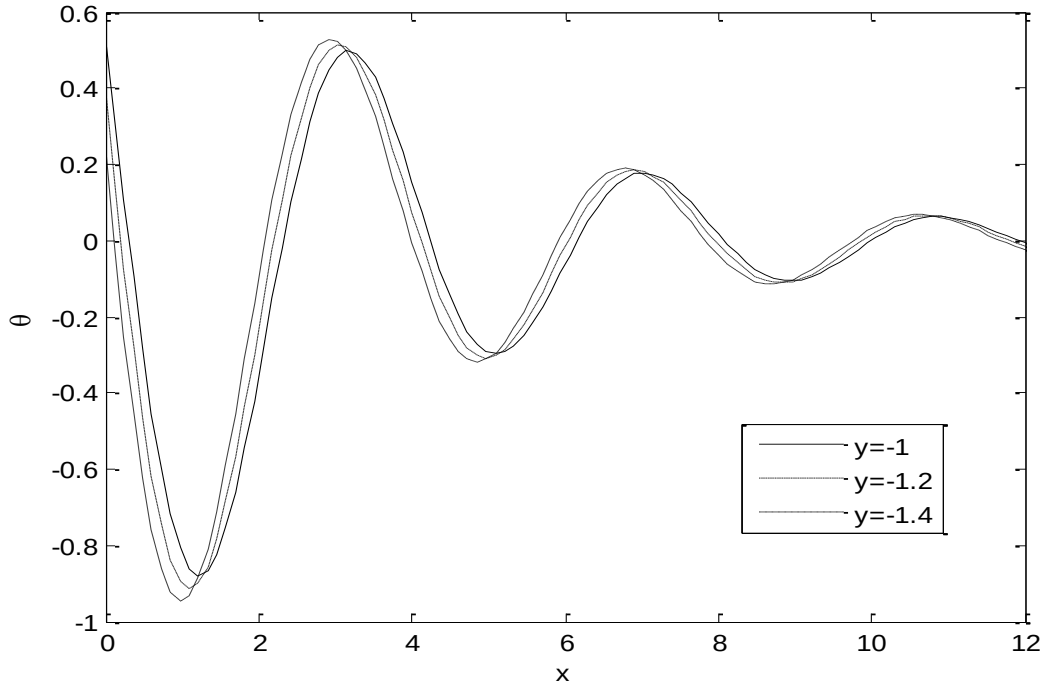

Figure 9. Temperature distribution with Variation of distances under LS theory (problem 1).

boundary condition at $x=0$) and 7, take the same behavior of Figure 5. Figure 6, shows that the stress component σ_{xy} satisfies the boundary condition at $x=0$ and had a different behaviour. It decreases in the start and start increases (maximum) in the context of the two theories until reaching the crack end. These trends

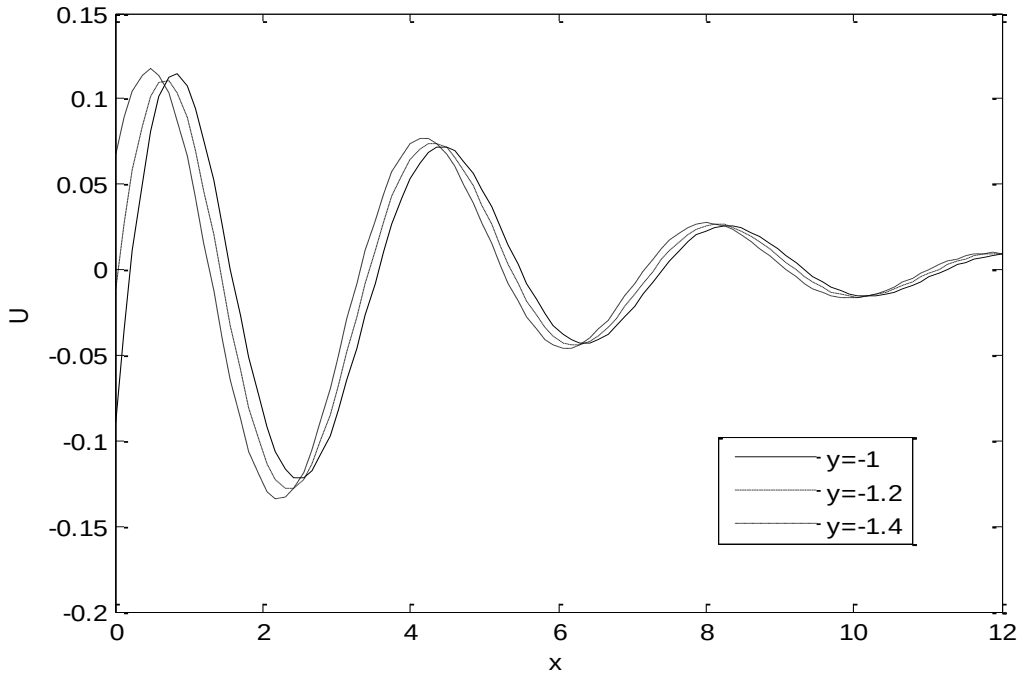

Figure 10. Displacement distribution u with variation of distance under L-S theory(problem 1).

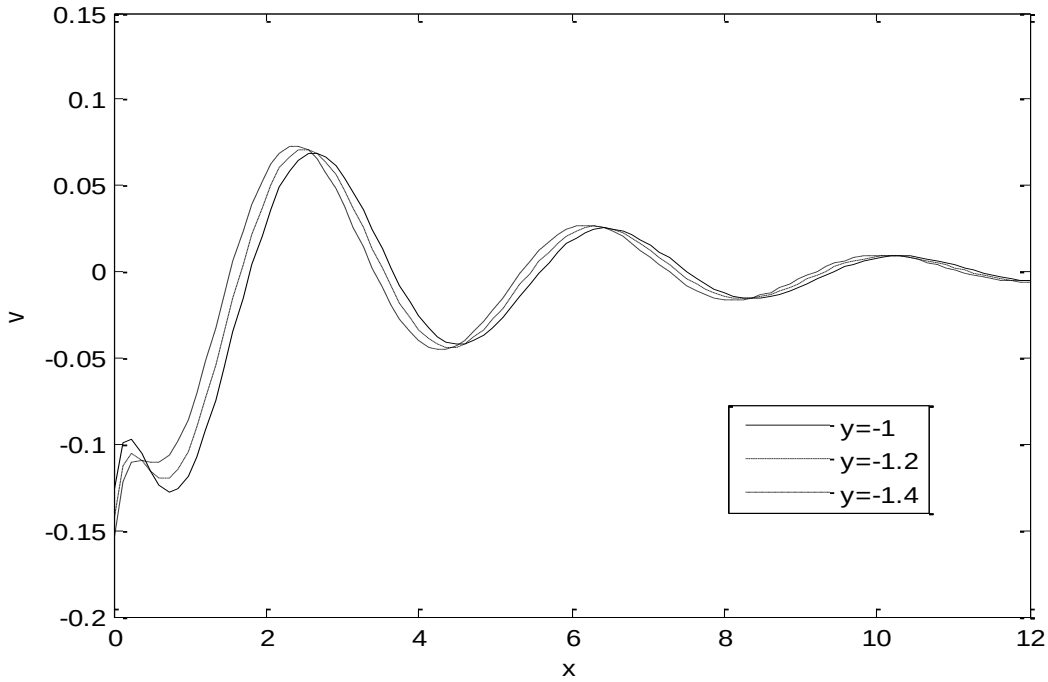

Figure 11. Displacement distribution v with variation of distance under LS theory(problem 1).

obey elastic and thermoelastic properties of the solid under investigation.

Figure 9-14 show the comparison between the temperature θ, displacement components u, v, the force stresses components σ_{xx}, σ_{yy} σ_{zz} and σ_{xz}, the case of different three values of y, (namely y= -1, y=-1.2 and y=-1.4) under (LS) theory. It should be noted (Figure 9) that in this problem. It is clear from the graph that θ

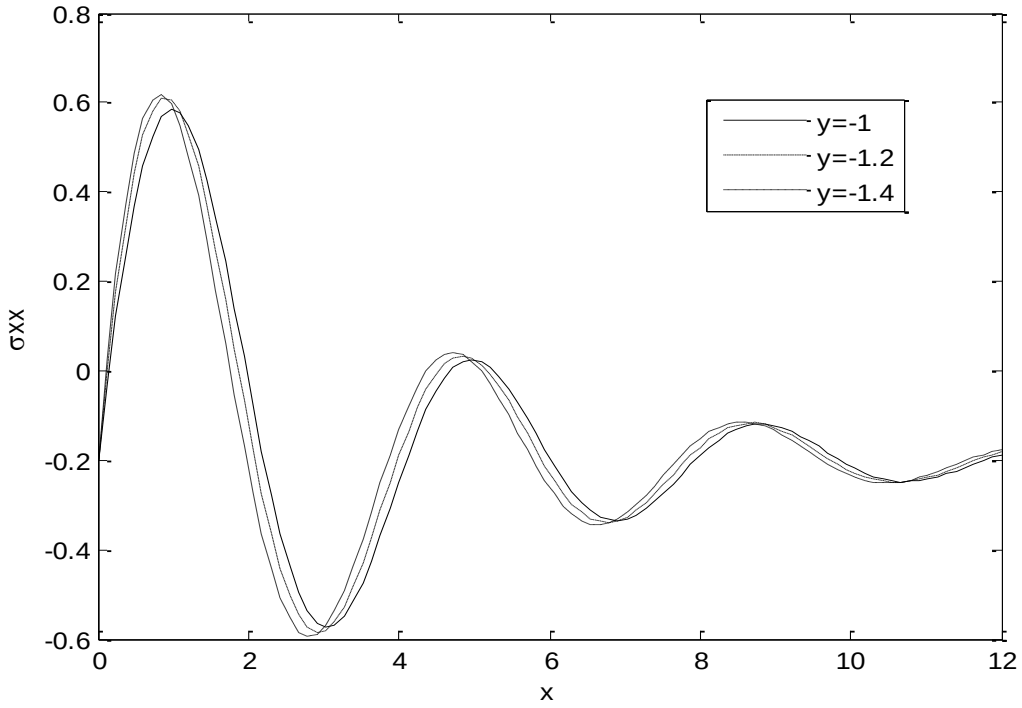

Figure 12. Stress distribution σ_{xx} with variation of distance under LS theory(problem 1).

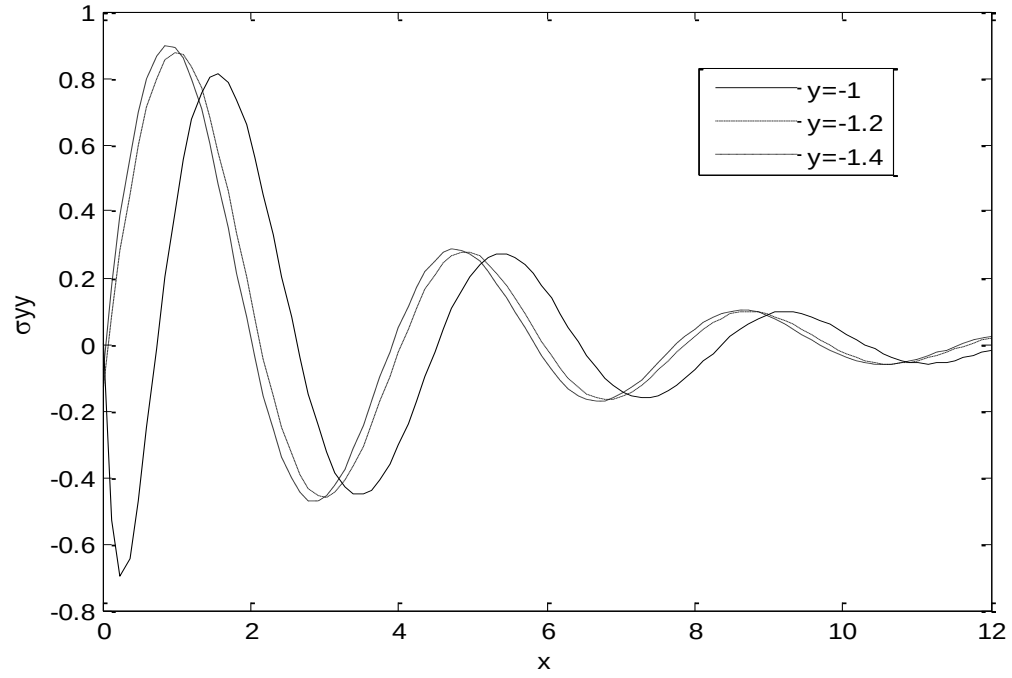

Figure 13. Stress distribution σ_{yy} with Variation of distance under LS theory (problem 1).

has minimum value at the beginning of the crack ($x=0$), it begins to fall just near the crack edge ($x\approx1.2$), where it experiences sharp increases (with maximum positive gradient at the crack's end). Graph

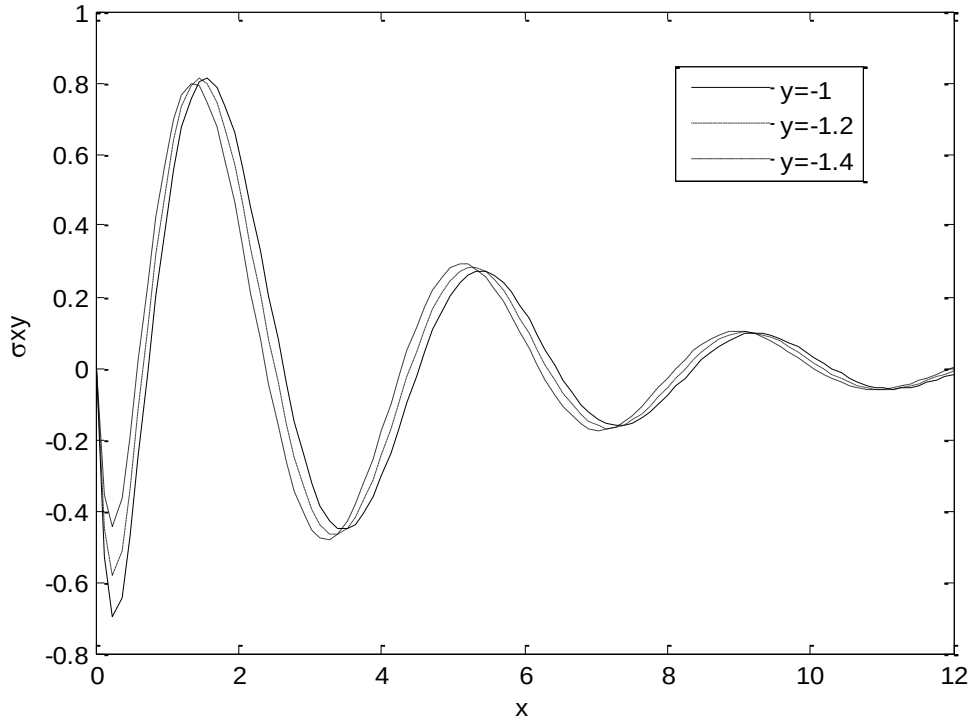

Figure 14. Stress distribution σ_{xy} with variation of distance under LS theory(problem 1).

lines for both values of y show different slopes at crack ends according to y-values. In other words, the temperature line for y =- 1 has the highest gradient when compared with that of y = -1.2 and y= -1.4 at the first of the range. In addition, all lines begin to coincide when the horizontal distance x is beyond the three double of the crack size to reach the reference temperature of the solid. These results obey physical reality for the behaviour of fiber as a polycrystalline solid.

Figure 10 the horizontal displacement u, despite the peaks (for different vertical distances y= -1, y=-1.2 and y=-1.4) occur at equal value of x, the magnitude of the maximum displacement peak strongly depends on the vertical distance y. it is also clear that the rate of change of u decreases with increasing y as we go farther apart from the crack. On the other hand, Figure 11 shows atonable increase of the vertical displacement v, near the crack end to reach minimum value beyond $x \approx 1.2$ reaching zero at the three double of the crack size (state of particles equilibrium). Figure 12, the horizontal stresses σ_{xx} Graph lines for both values of y show different slopes at crack ends according to y-values. In other words, the σ_{xx} component line for y = -1.4 has the highest gradient when compared with that of y = -1.2 and y= -1.4 at the edge of the crack. In addition, all lines begin to coincide when the horizontal distance x is beyond the three double of the crack size to reach zero after their relaxations at infinity. Variation of y has a serious effect on both magnitudes of mechanical stresses. These trends obey elastic and thermoelastic properties of the solid under investigation.

Figure 13, shows that the stress component σ_{yy} ,satisfy the boundary condition at $x = 0$, the line for y = -1.4 has the highest gradient when compared with that of y= -1 and y= -1.2 in the range $0 \le x \le 1.6$ (near the crack edge), the line for y = -1 has the highest gradient when compared with that of y=-1.2 and y=-1.4 in the range (near the crack end) $1.6 \le x \le 3$ and converge to zero when $x > 12$. These trends obey elastic and thermoelastic properties of the solid. Figure 14, shows that the stress component σ_{xy} satisfy the boundary condition, it decreases in the start and start increases (maximum) in the context of the three values of y until reaching the crack end, the line for y=-1.4 has the highest gradient when compared with that of y=-1.2 and y=-1 in the range $0 \le x \le 1.7$, the line for y=-1 has the highest gradient when compared with that of y=-1.2 and y=-1.4 in the range $1.7 \le x \le 3.5$ and converge to zero when $x > 12$. These trends obey elastic and thermoelastic properties of the solid.

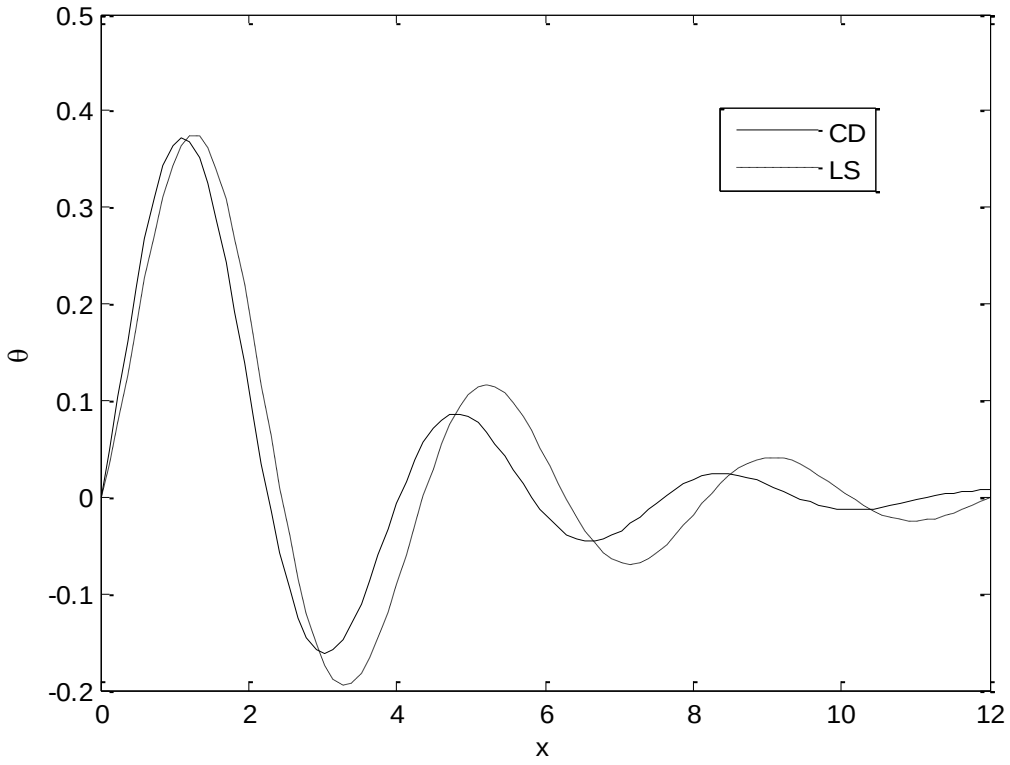

Figure 15. The temperature distribution for problem 2.

Problem 2

Figure 15 described the values of temperature θ under two theories. It indicts that the values of temperature θ increasing in the ranges $0 \le x \le 1.7$ and $3.2 \le x \le 5.2$ with fibre-reinforced and then decreases in the ranges $1.7 \le x \le 3.2$ and $5.2 \le x \le 6.5$. The values of temperature θ converge to zero with increasing the distance x.

In Figure 16, the horizontal displacement, u, begins with sharp decreases near the ($x \approx 1.4$), then smooth increases again to reach it's a maximum value just at near $x \approx 2.8$. Beyond it u falls again to try to retain zero at infinity. In Figure 17, the vertical displacement v, we see that the displacement component v always starts from the positive value and terminates at the zero value at the infinity (state of particles equilibrium). The displacements u and v show different behaviours, because of the elasticity of the solid tends to resist vertical displacements in the problem under investigation. Both of the components show different behaviours.

In Figure 18 the stress component, σ_{xx} reach coincidence with negative value and satisfy the boundary condition at $x = 0$, reach the maximum value near ($x \approx 3.3$) and converges to zero with increasing the distance x, also Figures 19-21 take the same behavior.

Figure 19, shows that the stress component σ_{xy} satisfy the boundary condition at $x = 0$ and had a different behaviour. It sharp increases in the start and start decreases (minimum) in the context of the two theories until reaching the crack end. These trends obey elastic and thermoelastic properties of the solid under investigation.

Conclusions

In the present study, the normal mode analysis is used to study the effect of the cracks of the problem under consideration at the free surface of a fiber-reinforced thermoelastic half-space based on the CD and L-S theory of thermoelasticity. According to the analysis above, we can conclude the following points:

(1) The curves in the context of the (CD) and (L-S) theories decrease exponentially with increasing x, this indicate that the thermoelastic waves are unattenuated and non dispersive, where purely thermoelastic waves undergo both attenuation and dispersion.

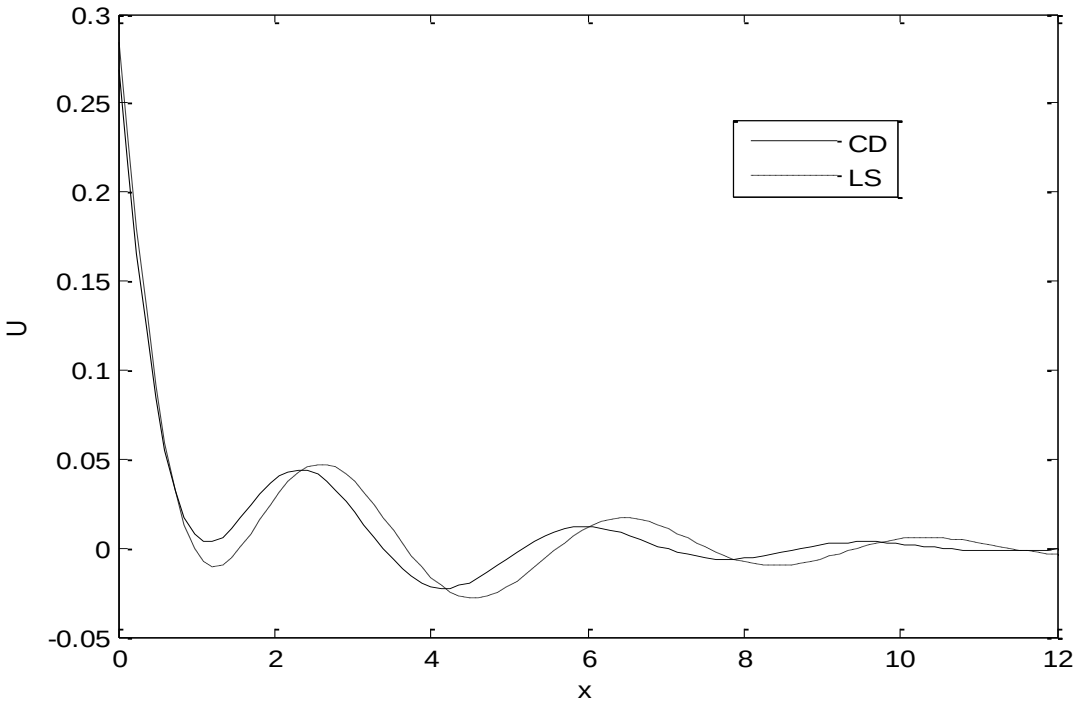

Figure 16. Horizontal displacement distribution u for problem 2.

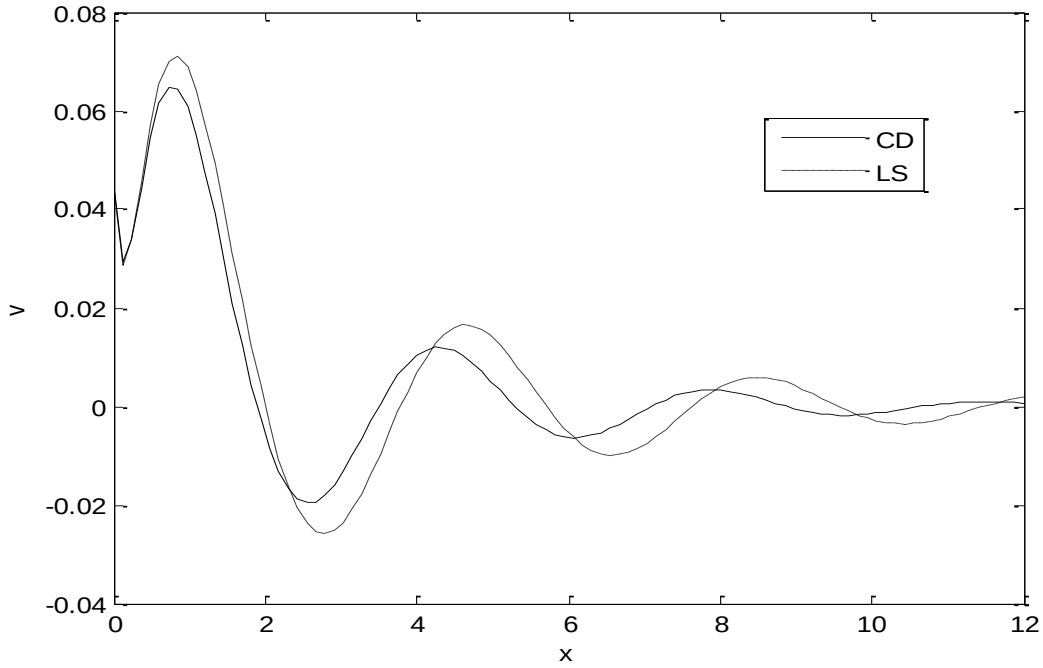

Figure 17. Vertical displacement distribution v for problem 2.

(2) The curves of the physical quantities with (CD) theory in most of figures are lower in comparison with those under (L-S) theory, due to the relaxation times.

(3) Analytical solutions based upon normal mode analysis for themoelastic problem in solids have been developed and utilized.

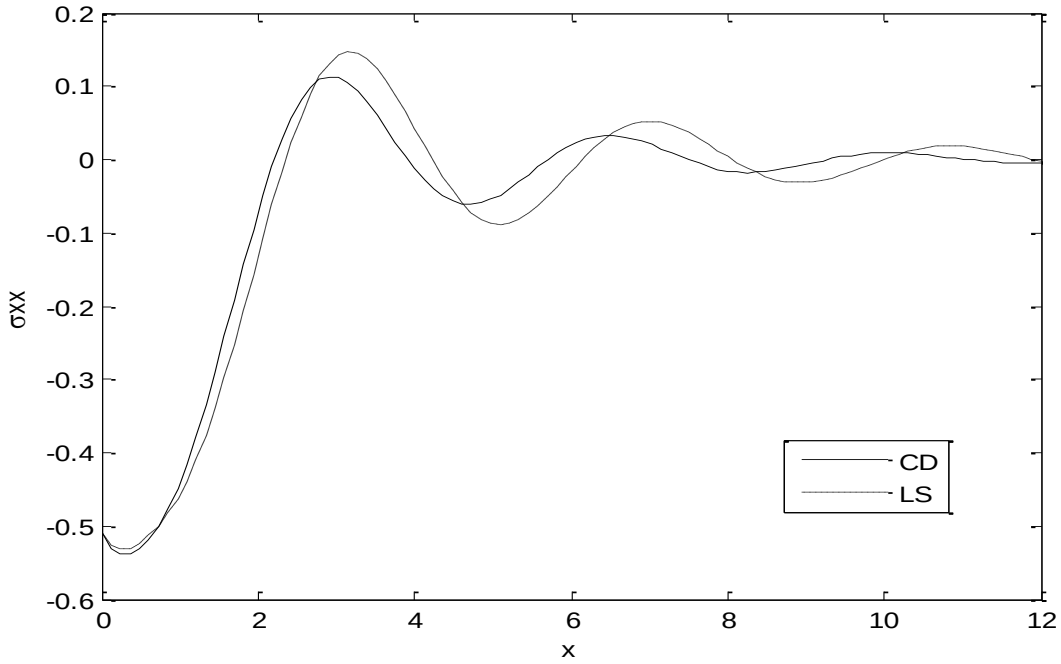

Figure 18. The distribution of stress component σ_{xx} for problem 2.

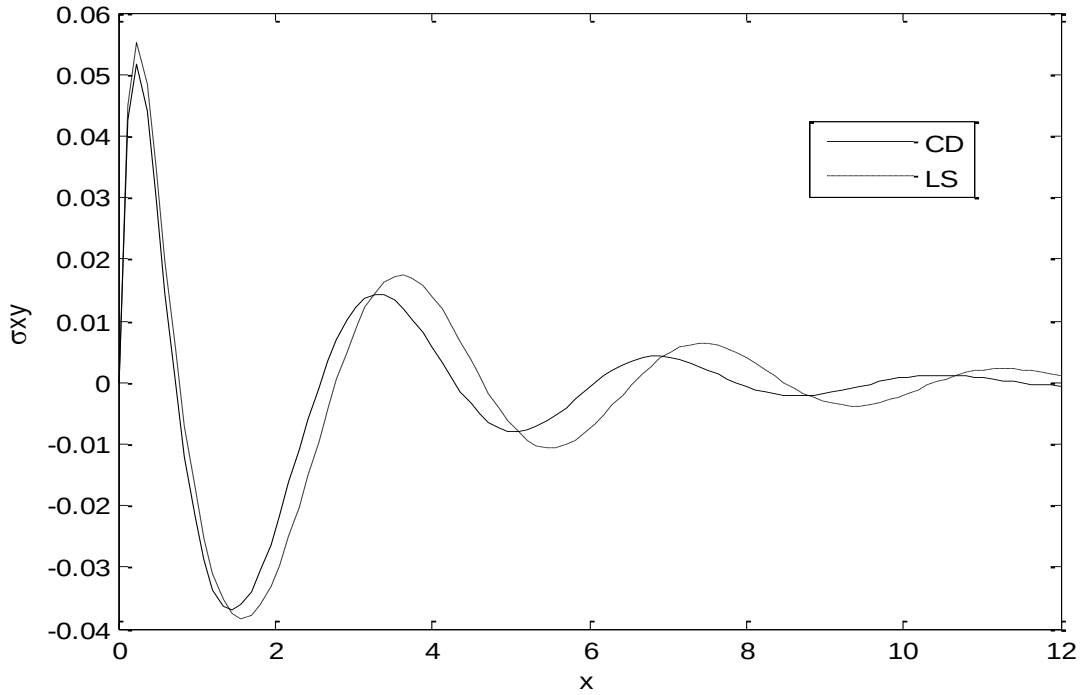

Figure 19. The distribution of stress component σ_{xy} for different problem 2.

(4) A linear opening mode-I crack has been investigated and studied for copper solid.

(5) Temperature, radial and axial distributions were estimated at different distances from the crack edge.

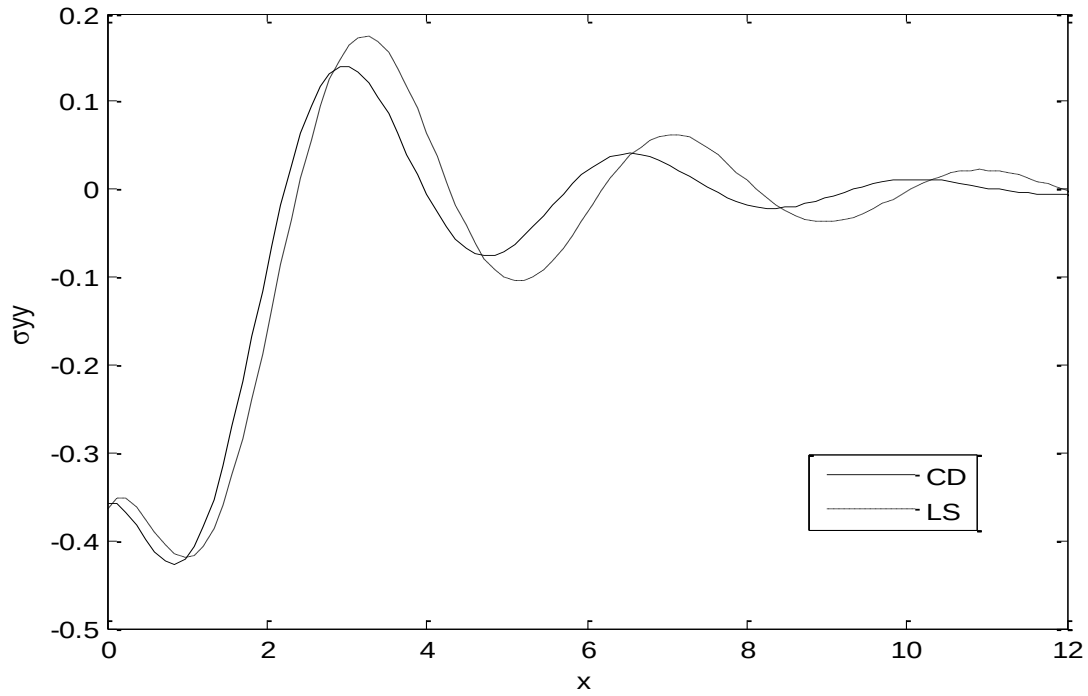

Figure 20. The distribution of stress component σ_{yy} for different problem 2.

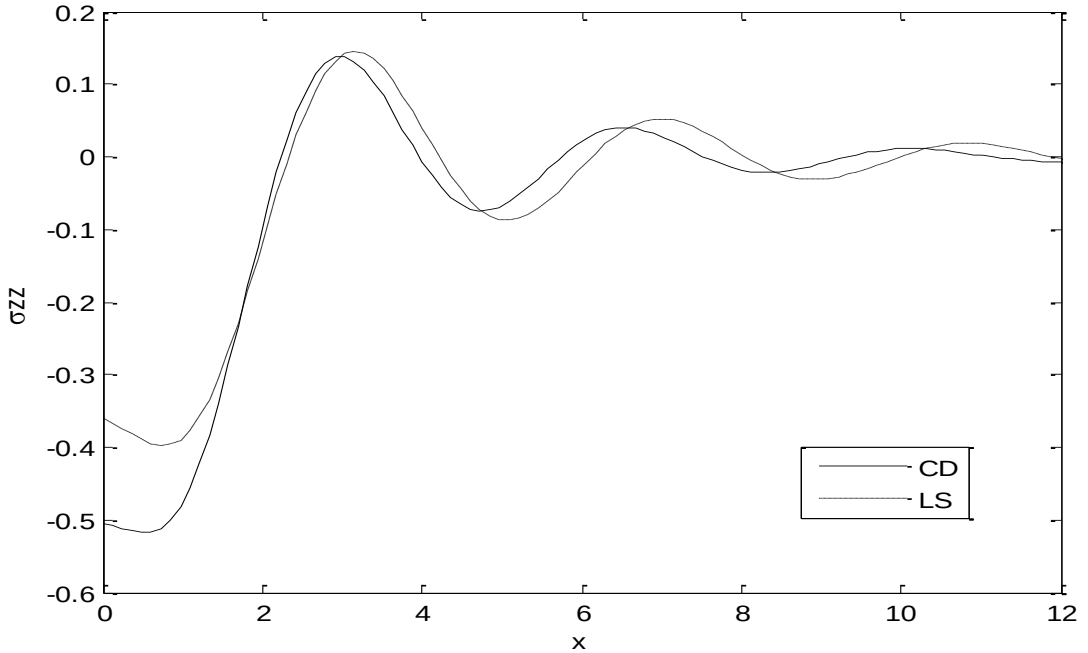

Figure 21. The distribution of stress component σ_{zz} for problem 2.

(6) The stresses distributions, and temperature were evaluated as functions of the distance from the crack edge.

(7) Crack dimensions are significant to elucidate the mechanical structure of the solid.

(8) Cracks are stationary and external stress is demanded

to propagate such cracks.
(9) It can be concluded that a change of volume is attended by a change of the temperature while the effect of the deformation upon the temperature distribution is the subject of the theory of thermoelasticity.
(10) The value of all the physical quantities converges to zero with an increase in distance y and All functions are continuous.
(11) The fibre-reinforced has an important role on the distribution of the field quantities.
(12) The method which used in the present article is applicable to a wide range of problems in thermodynamics and thermoelasticity.
(13) Deformation of a body depends on the nature of the applied force as well as the type of boundary conditions
(14) It is clear from all the figures that all the distributions considered have a non-zero value only in a bounded region of the half-space. Out side of this region, the values vanish identically and this means that the region has not felt thermal disturbance yet.
(15) The results presented in this paper should prove useful for researchers in material science, designers of new materials, low temperature physicists, as well as for those working on the development of a theory of hyperbolic thermoelasticity. The introduction of the crack to the generalized fiber-reinforced thermoelastic medium provides a more realistic model for these studies.

REFERENCES

Belfield AJ, Rogers TG, Spencer AJM (1983). Stress in elastic plates reinforced by fiber lying in concentric circles, J. Mech. Phys. Solids, 31:25-54.

Chattopadhyay A, Choudhury S (1990). Propagation, reflection and transmission of magneto-elastic shear waves in a self-reinforced medium, Int. J. Eng. Sci. 28:485-495.

Chattopadhyay A, Choudhury S (1995). Magnetoelastic shear waves in an infinite self-rein-forced plate, Int. J. Num. Anal. Methods Geomech. 19:289-304.

Chattopadhyay A, Venkateswarlu RLK, Saha S (2002). Reflection of quasi-P and quasi-SV waves at the free and rigid boundaries of a fibre-reinforced medium, Sãdhanã, 27:613-630.

Chaudhary S, Kaushik VP, Tomar SK (2004). Reflection/transmission of plane wave through a self-reinforced elastic layer between two half-spaces, Acta Geophysica Polonica. 52:219-235.

Dhaliwal R (1980). External Crack due to Thermal Effects in an Infinite Elastic Solid with a Cylindrical Inclusion. Thermal Stresses in Server Environments Plenum Press, New York and London, pp. 665-692.

Elfalaky A, Abdel-Halim AA (2006). A Mode-I Crack Problem for an Infinite Space in Thermoelasticity, J. Appl. Sci. 6:598-606.

Green AE, Lindsay KA (1972). Thermoelasticity. J. Elasticity 2:1-7.

Hasanyan D, Librescu L, Qin Z, Young R (2005). Thermoelastic Cracked Plates Carrying nonstationary Electrical Current. J. Thermal Stresses, 28:729-745.

Hashin Z, Rosen WB (1964). The elastic moduli of fibre-reinforced materials, J. Appl. Mech. 31:223-232.

Lord HW, Şhulman YA (1967). Generalized dynamical theory of thennoelasticity. J. Mech. Phys. Solid, 15:299-306.

Lotfy KH (2012a). Mode-I crack in a two-dimensional fibre-reinforced generalized thermoelastic problem, Chin. Phys. B, 21:1-014209.

Lotfy KH (2012b). The effect of a magnetic field on a 2D problem of fibre-reinforced thermoelasticity rotation under three theories, Chin. Phys. B; 21:6- 064214

Othman M, Atwa S (2012). Generalized Magneto-thermoelasticity in a Fibre- reinforced Anisotropic Half-space with Energy Dissipation, Int. J. Thermophys. 33(6):1126-1142.

Othman M, Lotfy KH (2009a). Effect of Magnetic Field and Inclined Load in Micropolar Thermoelastic Medium Possessing Cubic Symmetry, Int. J. Ind. Math. 1(2):87-104.

Othman M, Lotfy KH (2009b). Two-dimensional Problem of Generalized Magneto-thermoelasticity under the Effect of Temperature Dependent Properties for Different Theories, MMMS, 5:235-242.

Othman M, Lotfy KH (2010a). Generalized Thermo-microstretch Elastic Medium with Temperature Dependent Properties for Different Theories, Engineering Analysis with Boundary Elements, 34:229-237.

Othman M, Lotfy KH (2010b). On the Plane Waves in Generalized Thermo-microstretch Elastic Half-space, International Communication in Heat and Mass Transfer, 37:192-200.

Othman M, Lotfy KH (2013). The effect of magnetic field and rotation of the 2-D problem of a fiber-reinforced thermoelastic under three theories with influence of gravity, Mech. Mater. 60:120-143.

Othman M, Lotfy KH, Farouk RM (2009). Transient Disturbance in a Half-space under Generalized Magneto-thermoelasticity due to Moving Internal Heat Source, Acta Physica Polonica A, 116:186-192.

Othman M, Saied S (2012a). The Effect of Mechanical Force on Generalized Thermoelasticity in a Fiber-reinforced under Three Theories, Int. J. Thermophys. 33(6):1082-1099.

Othman M, Saied S (2012b). The Effect of Rotation on Two-dimensional Problem of a Fibre-reinforced Thermoelastic with One Relaxation Time, Int. J. Thermophys. 33(2):160-171.

Othman M, Saied S (2013). Two-Dimensional Problem of Thermally Conducting Fiber-reinforced under Green-Naghdi Theory, J. Thermoelasticity. 1 (1):13-20

Othman MIA, Song YQ (2007). Reflection of plane waves from an elastic solid half-space under hydrostatic initial stress without energy dissipation, Int. J. Sol. Struct. 44:5651-5664.

Pradhan A, Samal SK, Mahanti NC (2003). "Influence of anisotropy on the love waves in a self- reinforced medium", Tamkang J. Sci. Eng. 6(3):173-178.

Sengupta PR, Nath S (2001). Surface waves in fibre-reinforced anisotropic elastic media, Sãdhanã, 26:363-370.

Singh B (2006). Wave propagation in thermally conducting linear fibre-reinforced composite materials, Arch. Appl. Mech.75:513-520.

Singh B, Singh SJ (2004). "Reflection of planes waves at the free surface of a fibre- reinforced elastic half-space", Sãdhanã, 29:249-257.

Singh SJ (2002). Comments on "Surface waves in fibre-reinforced anisotropic elastic media" by Sengupta and Nath [Sãdhanã, 2001 26, 363-370]. Sãdhanã. 27:1-3.

Ueda S (2003). Thermally induced fracture of a piezoelectric Laminate with a crack Normal to Interfaces, J. Thermal Stresses, 26:311-323.

Verma PDS (1986). Magnetoelastic shear waves in self-reinforced bodies, Int. J. Eng. Sci. 24:1067-1073.

Verma PDS, Rana OH, Verma M (1988). Magnetoelastic transverse surfaces waves in self-reinforced elastic bodies, Ind. J. Pure Appl. Math. 19:713-716.

academicJournals

Vol. 8(22), pp. 1246-1255, 16 June, 2013
DOI: 10.5897/IJPS2013.3905
ISSN 1992-1950 © 2013 Academic Journals
http://www.academicjournals.org/IJPS

International Journal of Physical Sciences

Full Length Research Paper

The improved Riccati equation mapping method for constructing many families of exact solutions for a nonlinear partial differential equation of nanobiosciences

Elsayed M. E. Zayed, Yasser A. Amer and Reham M. A. Shohib

Department of Mathematics, Faculty of Sciences, Zagazig University, Zagazig, Egypt.

Accepted 30 May, 2013

In this paper we apply the improved Riccati equation mapping method to construct many families of general exact solutions of a nonlinear partial differential equation involving parameters of special significant for nanobiosciences and biophysics, namely, the equation of nano-ionic currents along microtublues. Comparison between our new results and the well-known results are given. The nonlinear equation elaborated here is quite original and proposed in the context of important nanosciences problems related with cell signaling. It could be even of basic importance for explanation of congnitive processes in neurons. We can successfully recover the previously known exact solutions that have been found by other methods. The proposed method in this article can be applied to many other nonlinear partial differential equations.

Key words: Improved Riccati equation mapping method, exact traveling wave solutions, nonlinear partial differential equation of nano-ionic currents along microtublues.

INTRODUCTION

In recent years, the exact traveling wave solutions of nonlinear partial differential equations (PDEs) have been investigated by many authors who are interested in nonlinear physical phenomena. Many powerful methods have been presented by those authors such as the inverse scattering transform method (Ablowitz and Clarkson, 1991), the Hirota's bilinear method (Hirota, 1971), the Painleve expansion method (Weiss et al., 1983; Kudryashov, 1988, 1990, 19991), the Backlund truncated method (Miura, 1978), the exp-function method (He and Wu, 2006; Yusufoglu, 2008; Bekir, 2009, 2010; Aslan, 2011), the tanh-function method (Abdou, 2007; Fan, 2000; Zhang and Xia, 2008; Yusufoglu and Bekir, 2008), the Jacobi elliptic function method (Chen and Wang, 2005; Liu et al., 2001; Lu, 2005), the (G'/G)-expansion method (Wang et al., 2008; Zhang et al., 2008; Zayed, 2009, 2010; Bekir, 2008; Ayhan and Bekir, 2012; Aslan, 2010, 2011, 2012a, b), the generalized Riccati equation mapping method (Zhu 2008; Zayed and Arnous, 2013), and so on.

In the present paper, we shall use the improved Riccati equation mapping method to find the exact solutions of a nonlinear PDE of special significant for nanobiosciences. The main idea of this method is that the traveling wave solutions of nonlinear equations can be expressed by

*Corresponding author. E-mail: e.m.e.zayed@hotmail.com.

PACS: 02.30.Jr, 05.45.Yv, 02.30.Ik.

polynomials in Q where $Q = Q(\xi)$ satisfies the generalized Riccati equation $Q' = r + pQ + qQ^2$ where $\xi = kx + \omega t$ where r, p, k, ω and *q* are constants. The degree of this polynomial can be determined by considering the homogeneous balance between the highest order derivatives and the nonlinear terms appearing in the given nonlinear equation, the coefficients of this polynomial can be obtained by solving a set of algebraic equations resulted from the process of using the proposed method.

The objective of this paper is to apply the improved Riccati equation mapping method for finding many families of exact traveling wave solutions of the following nonlinear PDE which describes the problem of transfer of ions along microtubules (Sekulic et al., 2011, Sataric et al., 2010):

$$\frac{L^2}{3}u_{xxx} + \frac{Z^{1/2}}{L}(\chi G_0 - 2\delta C_0)uu_t + 2u_x + \frac{ZC_0}{L}u_t + \frac{1}{L}(RZ^{-1} - G_0 Z)u = 0 \quad (1)$$

Here $R = 0.34 \times 10^9 \Omega$ is the resistance of the electric elementary unit (EEU), $L = 8 \times 10^{-9} m$ is the length of one tubulin heterodimer protein (EEU), $C_0 = 1.8 \times 10^{-15} F$ is the total maximal capacitance of the EEU. $G_0 = 1.1 \times 10^{-13} si$ is the conductance of pertaining the nano-pores (NPs) and $Z = 5.56 \times 10^{10} \Omega$ represents the characteristic impedance of the system. The parameters $\delta \text{ and } \chi$ describe the nonlinearity of the EEU's capacitance and conductance of existing between protofilaments of microtubule, respectively. The detailed consideration of microtubules in the context of nonlinear transmission lines is presented in (Sekulic et al., 2011, Sataric et al., 2009). The physical details of the derivation of Equation (1) describing the time-space voltage of ionic pulse is elaborated in (Sataric et al., 2010). Recently, Equation (1) has been discussed in (Sekulic et al., 2011) by using the modified extended tanh-function method, where its exact solutions have been found. Comparison between our new results in this article and the well - known results obtained in (Sataric et al., 2010) will be investigated later.

Description of the improved Riccati equation mapping method

We suppose that a nonlinear PDE in the following from:

$$P(u, u_x, u_t, u_{xx}, u_{tt}, ...) = o, \quad (2)$$

where $u = u(x,t)$ is an unknown function, *P* is a polynomial in $u = u(x,t)$ and its partial derivatives in which the highest order derivatives and nonlinear terms are involved, Let us now give the main steps for solving Equation (1) using the improved Riccati equation mapping method (Zhu, 2008; Zayed and Arnous, 2013):

Step 1: We look for its traveling wave solution in the form

$$u(x,t) = u(\xi), \quad \xi = kx + \omega t, \quad (3)$$

where k, ω are constants. Substituting Equation (3) into Equation (2) gives the nonlinear ordinary differential equation (ODE) for $u(\xi)$ as follows:

$$H(u, u', u'', ...) = 0, \quad (4)$$

Here H is a polynomial in $u(\xi)$ and its total derivatives $u', u'', u''', ...$ such that $u' = \frac{du}{d\xi}, u'' = \frac{d^2u}{d\xi^2}, ...$

Step 2: We suppose that the solution of the ODE (2.3) can be expressed as follows:

$$u(\xi) = \sum_{i=-m}^{m} a_i Q^i(\xi), \quad (5)$$

where $a_i (i = 0, \pm 1, \pm 2, ..., \pm m)$ are constants to be determined later such as $a_m \neq 0$ or $a_{-m} \neq 0$, and $Q = Q(\xi)$ is the solution of generalized Riccati equation:

$$Q' = r + pQ + qQ^2, \quad (6)$$

where *r, p* and *q* are constants , such that $q \neq 0$.

Step 3: We determine the positive integer *m* in Equation (5) by balancing the nonlinear terms and the highest order derivatives of $u(\xi)$ in Equation (4).

Step 4: Substituting Equation (5) and along with Equation (5) into Equation (4) and then equating all the coefficients of $Q^i (i = 0, \pm 1, \pm 2, ..., \pm m)$ to zero yield a system of algebraic equations which can be solved by using the Maple or Mathematica to find the values of the constants $a_i(-m, ..., m)$ and k, ω.

Step 5: It is well-known (Zhu, 2008; Zayed and Arnous, 2013) that Equation (6) has many families of solutions:

Type 1: When $\Delta = p^2 - 4qr > 0$ and $pq \neq 0$ or

$qr \neq 0$ we have

$$\Phi_1(\xi) = -\frac{1}{2q}[p + \sqrt{\Delta}\tanh(\frac{\sqrt{\Delta}}{2}\xi)],$$

$$\Phi_2(\xi) = -\frac{1}{2q}[p + \sqrt{\Delta}\coth(\frac{\sqrt{\Delta}}{2}\xi)],$$

$$\Phi_3(\xi) = -\frac{1}{2q}[p + \sqrt{\Delta}(\tanh(\sqrt{\Delta}\xi) \pm i\,\mathrm{sech}(\sqrt{\Delta}\xi))], \quad i\sqrt{-1}$$

$$\Phi_4(\xi) = -\frac{1}{2q}[p + \sqrt{\Delta}(\coth(\sqrt{\Delta}\xi) \pm \mathrm{csch}(\sqrt{\Delta}\xi))],$$

$$\Phi_5(\xi) = -\frac{1}{4q}[2p + \sqrt{\Delta}(\tanh(\frac{\sqrt{\Delta}}{4}\xi) \pm \coth(\frac{\sqrt{\Delta}}{4}\xi))],$$

$$\Phi_6(\xi) = \frac{1}{2q}[-p + \frac{\sqrt{\Delta(A^2+B^2)} - A\sqrt{\Delta}\cosh(\sqrt{\Delta}\xi)}{A\sinh(\sqrt{\Delta}\xi) + B}],$$

$$\Phi_7(\xi) = \frac{1}{2q}[-p - \frac{\sqrt{\Delta(B^2-A^2)} + A\sqrt{\Delta}\cosh(\sqrt{\Delta}\xi)}{A\sinh(\sqrt{\Delta}\xi) + B}],$$

where *A* and *B* are two non-zero real constants satisfying $B^2 - A^2 > 0$,

$$\Phi_8(\xi) = \frac{2r\cosh(\frac{\sqrt{\Delta}}{2}\xi)}{\sqrt{\Delta}\sinh(\frac{\sqrt{\Delta}}{2}\xi) - p\cos h(\frac{\sqrt{\Delta}}{2}\xi)},$$

$$\Phi_9(\xi) = \frac{-2r\sinh(\frac{\sqrt{\Delta}}{2}\xi)}{p\sinh(\frac{\sqrt{\Delta}}{2}\xi) - \sqrt{\Delta}\cosh(\frac{\sqrt{\Delta}}{2}\xi)},$$

$$\Phi_{10}(\xi) = \frac{2r\cosh(\frac{\sqrt{\Delta}}{2}\xi)}{\sqrt{\Delta}\sinh(\sqrt{\Delta}\xi) - p\cosh(\sqrt{\Delta}\xi) \pm i\sqrt{\Delta}}, \quad i = \sqrt{-1}$$

$$\Phi_{11}(\xi) = \frac{2r\sinh(\frac{\sqrt{\Delta}}{2}\xi)}{-p\sinh(\sqrt{\Delta}\xi) + \sqrt{\Delta}\cosh(\sqrt{\Delta}\xi) \pm \sqrt{\Delta}},$$

$$\Phi_{12}(\xi) = \frac{4r\sinh(\frac{\sqrt{\Delta}}{4}\xi)\cosh(\frac{\sqrt{\Delta}}{4}\xi)}{-2p\sinh(\frac{\sqrt{\Delta}}{4}\xi)\cosh(\frac{\sqrt{\Delta}}{4}\xi) + 2\sqrt{\Delta}\cosh^2(\frac{\sqrt{\Delta}}{2}\xi) - \sqrt{\Delta}},$$

Type 2: When $\Delta = p^2 - 4qr < 0$ and $pq \neq 0$ or $qr \neq 0$ we have:

$$\Phi_{13}(\xi) = \frac{1}{2q}[-p + \sqrt{-\Delta}\tan(\frac{\sqrt{-\Delta}}{2}\xi)],$$

$$\Phi_{14}(\xi) = -\frac{1}{2q}[p + \sqrt{-\Delta}\cot(\frac{\sqrt{-\Delta}}{2}\xi)],$$

$$\Phi_{15}(\xi) = \frac{1}{2q}[-p + \sqrt{-\Delta}(\tan(\sqrt{-\Delta}\xi) \pm \sec(\sqrt{-\Delta}\xi))],$$

$$\Phi_{16}(\xi) = -\frac{1}{2q}[p + \sqrt{-\Delta}(\cot(\sqrt{-\Delta}\xi) \pm \csc(\sqrt{-\Delta}\xi))],$$

$$\Phi_{17}(\xi) = \frac{1}{4q}[-2p + \sqrt{-\Delta}(\tan(\frac{\sqrt{-\Delta}}{4}\xi) - \cot(\frac{\sqrt{-\Delta}}{4}\xi))],$$

$$\Phi_{18}(\xi) = \frac{1}{2q}[-p + \frac{\pm\sqrt{-\Delta(A^2-B^2)} - A\sqrt{-\Delta}\cos(\sqrt{-\Delta}\xi)}{A\sin(\sqrt{-\Delta}\xi) + B}],$$

$$\Phi_{19}(\xi) = \frac{1}{2q}[-p - \frac{\pm\sqrt{-\Delta(A^2-B^2)} - A\sqrt{-\Delta}\sin(\sqrt{-\Delta}\xi)}{A\sin(\sqrt{-\Delta}\xi) + B}],$$

where *A* and *B* are two non-zero real constants satisfying $A^2 - B^2 > 0$,

$$\Phi_{20}(\xi) = -\frac{2r\cos(\frac{\sqrt{-\Delta}}{2}\xi)}{\sqrt{-\Delta}\sin(\frac{\sqrt{-\Delta}}{2}\xi) + p\cos(\frac{\sqrt{-\Delta}}{2}\xi)},$$

$$\Phi_{21}(\xi) = \frac{2r\sin(\frac{\sqrt{-\Delta}}{2}\xi)}{-p\sin(\frac{\sqrt{-\Delta}}{2}\xi) + \sqrt{-\Delta}\cos(\frac{\sqrt{-\Delta}}{2}\xi)},$$

$$\Phi_{22}(\xi) = -\frac{2r\cos(\frac{\sqrt{-\Delta}}{2}\xi)}{\sqrt{-\Delta}\sin(\sqrt{-\Delta}\xi) + p\cos(\sqrt{-\Delta}\xi) \pm \sqrt{-\Delta}},$$

$$\Phi_{23}(\xi) = \frac{2r\sin(\frac{\sqrt{-\Delta}}{2}\xi)}{-p\sin(\sqrt{-\Delta}\xi) + \sqrt{-\Delta}\cos(\sqrt{-\Delta}\xi) \pm \sqrt{-\Delta}},$$

$$\Phi_{24}(\xi) = \frac{4r\sin(\frac{\sqrt{-\Delta}}{4}\xi)\cos(\frac{\sqrt{-\Delta}}{4}\xi)}{-2p\sin(\frac{\sqrt{-\Delta}}{4}\xi)\cos(\frac{\sqrt{-\Delta}}{4}\xi) + 2\sqrt{-\Delta}\cos^2(\frac{\sqrt{-\Delta}}{2}\xi) - \sqrt{-\Delta}},$$

Type 3: When $r = 0 \; and \; pq \neq 0$ we have:

$$\Phi_{25}(\xi) = \frac{-pd}{q[d + \cosh(p\xi) - \sinh(p\xi)]},$$

$$\Phi_{26}(\xi) = -\frac{p[\cosh(p\xi) + \sinh(p\xi)]}{q[d + \cosh(p\xi) + \sinh(p\xi)]},$$

where *d* is an arbitrary constant.

Type 4: When $r = p = 0 \; and \; q \neq 0$ we have $\Phi_{27}(\xi) = \frac{-1}{q\xi + c_1}$, where c_1 is an arbitrary constant.

Step 6: Substituting the well known solutions of Equation (6) listed in Step 5 into Equation (5), we have many families of exact solutions of Equation (2).

Many families of exact traveling wave solutions for Equation (1)

In this section, we apply the proposed method of the

description of the improved Riccati equation mapping method, to find many families of new exact traveling wave solutions of Equation (1). To this end, we use the wave transformation

$$u(x,t) = u(\xi), \qquad \xi = \frac{1}{L}x - \frac{c}{\tau}t, \tag{7}$$

where $\tau = RC_0 = 0.6\times10^{-6}s,$ represents the characteristic charging (discharging) time of an EEU's capacitor C_0 through the resistance R and c is the dimensionless velocity of the wave, to reduce Equation (1) into the following ODE:

$$u''' + A_1 cuu' + (6 - B_1 c)u' + C_1 u = 0. \tag{8}$$

Here the set of abbreviations are arranged as follows:

$$A_1 = \frac{3Z^{\frac{1}{2}}}{\tau}(2\delta C_0 - \chi G_0),\ B_1 = \frac{3ZC_0}{\tau},\ C_1 = 3(RZ^{-1} - G_0 Z)$$

By balancing $u''' \ with \ uu'$, we have m = 2. Hence the formal solution of Equation (7) takes the form

$$u(\xi) = a_2 Q^2 + a_1 Q + a_0 + a_{-1}Q^{-1} + a_{-2}Q^{-2}, \tag{9}$$

where $a_2, a_1, a_0, a_{-1}, a_{-2}$ are parameters to be determined later, such that $a_{-2} \neq 0$ or $a_2 \neq 0$.

Inserting Equation (9) with the aid of Equation (6) into Equation (8), we get the following system of algebraic equations:

$$\begin{aligned}
Q^{-5}: &\quad -24a_{-2}r^3 - 2a_{-2}^2 rA_1 c = 0,\\
Q^{5}: &\quad 24a_2 q^3 + 2a_2^2 qA_1 c = 0,\\
Q^{-4}: &\quad -54a_{-2}pr^2 - 6a_{-1}r^3 - A_1 c(2a_{-2}^2 p + 3a_{-1}a_{-2}r) = 0,\\
Q^{4}: &\quad 54a_2 pq^2 + 6a_1 q^3 + A_1 c(2a_2^2 p + 3a_1 a_2 q) = 0,
\end{aligned}$$

$$\begin{aligned}
Q^{-3}: &\quad -40a_{-2}qr^2 - 38a_{-2}p^2 r - 12a_{-1}pr^2 - A_1 c(2a_{-2}^2 q + 3a_{-1}a_{-2}p + a_{-1}^2 r + 2a_0 a_{-2}r) - 2a_{-2}r(6 - B_1 c) = 0,\\
Q^{3}: &\quad 40a_2 q^2 r + 38a_2 p^2 q + 12a_1 pq^2 + A_1 c(2a_2^2 r + 3a_1 a_2 p + a_1^2 q + 2a_0 a_2 q) + 2a_2 q(6 - B_1 c) = 0,
\end{aligned}$$

$$\begin{aligned}
Q^{-2}: &\quad -52a_{-2}pqr - 8a_{-1}qr^2 - 7a_{-1}p^2 r - 8a_{-2}p^3 - A_1 c(3a_{-1}a_{-2}q + a_1 a_{-2}r + a_{-1}^2 p + 2a_0 a_{-2}p + a_0 a_{-1}r)\\
&\quad -(2a_{-2}p + a_{-1}r)(6 - B_1 c) + C_1 a_{-2} = 0,\\
Q^{2}: &\quad 52a_2 pqr + 8a_1 q^2 r + 7a_1 p^2 q + 8a_2 p^3 + A_1 c(3a_1 a_2 r + a_{-1}a_2 q + a_1^2 p + 2a_0 a_2 p + a_0 a_1 q)\\
&\quad +(2a_2 p + a_1 q)(6 - B_1 c) + C_1 a_2 = 0,
\end{aligned}$$

$$\begin{aligned}
Q^{-1}: &\quad -16a_{-2}q^2 r - 8a_{-1}pqr - 14a_{-2}p^2 q - a_{-1}p^3 - A_1 c(a_1 a_{-2}p + a_{-1}^2 q + 2a_0 a_{-2}q + a_0 a_{-1}p)\\
&\quad -(2a_{-2}q + a_{-1}p)(6 - B_1 c) + C_1 a_{-1} = 0,\\
Q: &\quad 16a_2 qr^2 + 8a_1 pqr + 14a_2 p^2 r + a_1 p^3 + A_1 c(a_{-1}a_2 p + a_1^2 r + 2a_0 a_2 r + a_0 a_1 p)\\
&\quad +(2a_2 r + a_1 p)(6 - B_1 c) + C_1 a_1 = 0,
\end{aligned}$$

$$\begin{aligned}
Q^{0}: &\quad -6a_{-2}pq^2 - 2a_{-1}q^2 r - a_{-1}p^2 q + a_1 p^2 r + 6a_2 pr^2 + 2a_1 qr^2\\
&\quad +A_1 c(-a_1 a_{-2}q + a_{-1}a_2 r - a_0 a_{-1}q + a_0 a_1 r) + (a_1 r - a_{-1}q)(6 - B_1 c) + C_1 a_0 = 0
\end{aligned}$$

By solving these algebraic equations with the aid of Maple or Mathematica we have the following cases:

Case 1

$$p = p,\ q = q,\ r = r,\ c = \frac{(p^2 + 8qr + 6)}{B_1 - a_0 A_1},\ a_0 = a_0,\ a_1 = \frac{-12pq(B_1 - a_0 A_1)}{A_1(p^2 + 8qr + 6)},$$
$$a_2 = \frac{-12q^2(B_1 - a_0 A_1)}{A_1(p^2 + 8qr + 6)},\ a_{-1} = 0,\ a_{-2} = 0$$

Case 2

$$p = 0,\ q = q,\ r = r,\ c = \frac{8qr + 6}{B_1 - a_0 A_1},\ a_0 = a_0,\ a_1 = 0, a_{-2} = \frac{-12r^2(B_1 - a_0 A_1)}{A_1(8qr + 6)},\ a_{-1} = 0,\ a_2 = 0$$

Case 3

$$p = 0,\ q = q,\ r = \frac{3}{4a_2 q}(2a_0 q^2 - a_2 - 2q^2(\frac{B_1}{A_1})),\ c = \frac{-12q^2}{a_2 A_1},\ a_0 = a_0,\ a_1 = 0,$$
$$a_{-2} = \frac{9}{16a_2 q^4}\left[2a_0 q^2 - a_2 - 2q^2(\frac{B_1}{A_1})\right]^2,\ a_{-1} = 0,\ a_2 \neq 0$$

Exact traveling wave solutions of Equation (1) for Case 1

By using the case 1 and according to the values of solutions of type 1, we obtain the following exact traveling

wave solutions for Equation (1):

$$u_1(x,t)=a_0+\frac{3(B_1-a_0A_1)}{A_1(p^2+8qr+6)}[p^2\sec h^2(\frac{\sqrt{\Delta}}{2}\xi)+4qr\tanh^2(\frac{\sqrt{\Delta}}{2}\xi)],$$

$$u_2(x,t)=a_0+\frac{3(B_1-a_0A_1)}{A_1(p^2+8qr+6)}[-p^2\csc h^2(\frac{\sqrt{\Delta}}{2}\xi)+4qr\,coth^2(\frac{\sqrt{\Delta}}{2}\xi)],$$

$$u_3(x,t)=a_0+\frac{3(B_1-a_0A_1)}{A_1(p^2+8qr+6)}[p^2-\Delta(\tanh(\sqrt{\Delta}\xi)\pm i\ \sec h(\sqrt{\Delta}\xi))^2],$$

$$u_4(x,t)=a_0+\frac{3(B_1-a_0A_1)}{A_1(p^2+8qr+6)}[p^2-\Delta(coth(\sqrt{\Delta}\xi)\pm\csc h(\sqrt{\Delta}\xi))^2],$$

$$u_5(x,t)=a_0+\frac{3(B_1-a_0A_1)}{4A_1(p^2+8qr+6)}[4p^2-\Delta(\tanh(\frac{\sqrt{\Delta}}{4}\xi)\pm coth(\frac{\sqrt{\Delta}}{4}\xi))^2],$$

$$u_6(x,t)=a_0+\frac{3(B_1-a_0A_1)}{A_1(p^2+8qr+6)}[p^2-\Delta\frac{(\sqrt{A^2+B^2}-A\cosh(\sqrt{\Delta}\xi))^2}{(A\sinh(\sqrt{\Delta}\xi)+B)^2}],$$

$$u_7(x,t)=a_0+\frac{3(B_1-a_0A_1)}{A_1(p^2+8qr+6)}[p^2-\Delta\frac{(\sqrt{B^2-A^2}+A\cosh(\sqrt{\Delta}\xi))^2}{(A\sinh(\sqrt{\Delta}\xi)+B)^2}],$$

where A and B are two non-zero real constants satisfying $B^2 - A^2 > 0$,

$$u_8(x,t)=a_0-\frac{24qr(B_1-a_0A_1)}{A_1(p^2+8qr+6)}\left(\frac{\cosh(\frac{\sqrt{\Delta}}{2}\xi)}{(\sqrt{\Delta}\sinh(\frac{\sqrt{\Delta}}{2}\xi)-p\cosh(\frac{\sqrt{\Delta}}{2}\xi))}\right)\times\left(p+2qr\frac{\cosh(\frac{\sqrt{\Delta}}{2}\xi)}{(\sqrt{\Delta}\sinh(\frac{\sqrt{\Delta}}{2}\xi)-p\cosh(\frac{\sqrt{\Delta}}{2}\xi))}\right),$$

$$u_9(x,t)=a_0+\frac{24qr(B_1-a_0A_1)}{A_1(p^2+8qr+6)}\left(\frac{\sinh(\frac{\sqrt{\Delta}}{2}\xi)}{(p\sinh(\frac{\sqrt{\Delta}}{2}\xi)-\sqrt{\Delta}\cosh(\frac{\sqrt{\Delta}}{2}\xi))}\right)\times\left(p-2qr\frac{\sinh(\frac{\sqrt{\Delta}}{2}\xi)}{(p\sinh(\frac{\sqrt{\Delta}}{2}\xi)-\sqrt{\Delta}\cosh(\frac{\sqrt{\Delta}}{2}\xi))}\right),$$

$$u_{10}(x,t)=a_0-\frac{24qr(B_1-a_0A_1)}{A_1(p^2+8qr+6)}\left(\frac{\cosh(\frac{\sqrt{\Delta}}{2}\xi)}{(\sqrt{\Delta}\sinh(\sqrt{\Delta}\xi)-p\cosh(\sqrt{\Delta}\xi)\pm i\sqrt{\Delta})}\right)\times\left(p+2qr\frac{\cosh(\frac{\sqrt{\Delta}}{2}\xi)}{(\sqrt{\Delta}\sinh(\sqrt{\Delta}\xi)-p\cosh(\sqrt{\Delta}\xi)\pm i\sqrt{\Delta})}\right),$$

$$u_{11}(x,t)=a_0-\frac{24qr(B_1-a_0A_1)}{A_1(p^2+8qr+6)}\left(\frac{\sinh(\frac{\sqrt{\Delta}}{2}\xi)}{(-p\sinh(\sqrt{\Delta}\xi)+\sqrt{\Delta}\cosh(\sqrt{\Delta}\xi)\pm\sqrt{\Delta})}\right)\times\left(p+2qr\frac{\sinh(\frac{\sqrt{\Delta}}{2}\xi)}{(-p\sinh(\sqrt{\Delta}\xi)+\sqrt{\Delta}\cosh(\sqrt{\Delta}\xi)\pm\sqrt{\Delta})}\right),$$

$$u_{12}(x,t)=a_0-\frac{48qr(B_1-a_0A_1)}{A_1(p^2+8qr+6)}\left(\frac{\sinh(\frac{\sqrt{\Delta}}{4}\xi)\cosh(\frac{\sqrt{\Delta}}{4}\xi)}{(-2p\sinh(\frac{\sqrt{\Delta}}{4}\xi)\cosh(\frac{\sqrt{\Delta}}{4}\xi)+2\sqrt{\Delta}\cosh^2(\frac{\sqrt{\Delta}}{4}\xi)-\sqrt{\Delta})}\right)\times\left(p+4qr\frac{\sinh(\frac{\sqrt{\Delta}}{4}\xi)\cosh(\frac{\sqrt{\Delta}}{4}\xi)}{(-2p\sinh(\frac{\sqrt{\Delta}}{4}\xi)\cosh(\frac{\sqrt{\Delta}}{4}\xi)+2\sqrt{\Delta}\cosh^2(\frac{\sqrt{\Delta}}{4}\xi)-\sqrt{\Delta})}\right).$$

According to the values of solutions of Type 2, we obtain the following exact traveling wave solutions for Equation (1):

$$u_{13}(x,t)=a_0+\frac{3(B_1-a_0A_1)}{A_1(p^2+8qr+6)}[p^2\sec^2(\frac{\sqrt{-\Delta}}{2}\xi)-4qr\tan^2(\frac{\sqrt{-\Delta}}{2}\xi)],$$

$$u_{14}(x,t)=a_0+\frac{3(B_1-a_0A_1)}{A_1(p^2+8qr+6)}[p^2\csc^2(\frac{\sqrt{-\Delta}}{2}\xi)-4qr\cot^2(\frac{\sqrt{-\Delta}}{2}\xi)],$$

$$u_{15}(x,t)=a_0+\frac{3(B_1-a_0A_1)}{A_1(p^2+8qr+6)}[p^2+\Delta(\tan(\sqrt{-\Delta}\xi)\pm\sec(\sqrt{-\Delta}\xi))^2],$$

$$u_{16}(x,t)=a_0+\frac{3(B_1-a_0A_1)}{A_1(p^2+8qr+6)}[p^2+\Delta(\cot(\sqrt{-\Delta}\xi)\pm\csc(\sqrt{-\Delta}\xi))^2],$$

$$u_{17}(x,t)=a_0+\frac{3(B_1-a_0A_1)}{4A_1(p^2+8qr+6)}[4p^2+\Delta(\tan(\frac{\sqrt{-\Delta}}{4}\xi)-\cot(\frac{\sqrt{-\Delta}}{4}\xi))^2],$$

$$u_{18}(x,t)=a_0+\frac{3(B_1-a_0A_1)}{A_1(p^2+8qr+6)}[p^2+\Delta\left(\frac{\sqrt{A^2-B^2}-A\cos(\sqrt{-\Delta}\xi)}{A\sinh(\sqrt{-\Delta}\xi)+B}\right)^2,$$

$$u_{19}(x,t)=a_0+\frac{3(B_1-a_0A_1)}{A_1(p^2+8qr+6)}[p^2+\Delta\left(\frac{\pm\sqrt{A^2-B^2}+A\cos(\sqrt{-\Delta}\xi)}{A\sin(\sqrt{-\Delta}\xi)+B}\right)^2,$$

$$u_{20}(x,t)=a_0+\frac{24qr(B_1-a_0A_1)}{A_1(p^2+8qr+6)}\left(\frac{\cos(\frac{\sqrt{-\Delta}}{2}\xi)}{\sqrt{-\Delta}\sin(\frac{\sqrt{-\Delta}}{2}\xi)+p\cos(\frac{\sqrt{-\Delta}}{2}\xi)}\right)\times\left(p-qr\frac{\cos(\frac{\sqrt{-\Delta}}{2}\xi)}{\sqrt{-\Delta}\sin(\frac{\sqrt{-\Delta}}{2}\xi)+p\cos(\frac{\sqrt{-\Delta}}{2}\xi)}\right),$$

$$u_{21}(x,t)=a_0-\frac{24qr(B_1-a_0A_1)}{A_1(p^2+8qr+6)}\left(\frac{\sin(\frac{\sqrt{-\Delta}}{2}\xi)}{-p\sin(\frac{\sqrt{-\Delta}}{2}\xi)+\sqrt{-\Delta}\cos(\frac{\sqrt{-\Delta}}{2}\xi)}\right)\times\left(p+2qr\frac{\sin(\frac{\sqrt{-\Delta}}{2}\xi)}{-p\sin(\frac{\sqrt{-\Delta}}{2}\xi)+\sqrt{-\Delta}\cos(\frac{\sqrt{-\Delta}}{2}\xi)}\right),$$

$$u_{22}(x,t)=a_0+\frac{24qr(B_1-a_0A_1)}{A_1(p^2+8qr+6)}\left(\frac{\cos(\frac{\sqrt{-\Delta}}{2}\xi)}{\sqrt{-\Delta}\sin(\frac{\sqrt{-\Delta}}{2}\xi)+p\cos(\frac{\sqrt{-\Delta}}{2}\xi)\pm\sqrt{-\Delta}}\right)$$
$$\times\left(p-2qr\frac{\sin(\frac{\sqrt{-\Delta}}{2}\xi)}{\sqrt{-\Delta}\sin(\frac{\sqrt{-\Delta}}{2}\xi)-p\cos(\frac{\sqrt{-\Delta}}{2}\xi)\pm\sqrt{-\Delta}}\right),$$

$$u_{23}(x,t)=a_0-\frac{24qr(B_1-a_0A_1)}{A_1(p^2+8qr+6)}\left(\frac{\sin(\frac{\sqrt{-\Delta}}{2}\xi)}{-p\sin(\sqrt{-\Delta}\xi)+\sqrt{-\Delta}\cos(\sqrt{-\Delta}\xi)\pm\sqrt{-\Delta}}\right)$$
$$\times\left(p+2qr\frac{\sin(\sqrt{-\Delta}\xi)}{-p\sin(\sqrt{-\Delta}\xi)+\sqrt{-\Delta}\cos(\sqrt{-\Delta}\xi)\pm\sqrt{-\Delta}}\right),$$

$$u_{24}(x,t)=a_0-\frac{48qr(B_1-a_0A_1)}{A_1(p^2+8qr+6)}\left(\frac{\sin(\frac{\sqrt{-\Delta}}{4}\xi)\cos(\frac{\sqrt{-\Delta}}{4}\xi)}{-2p\sin(\frac{\sqrt{-\Delta}}{4}\xi)\cos(\frac{\sqrt{-\Delta}}{4}\xi)+2\sqrt{-\Delta}\cos^2(\frac{\sqrt{-\Delta}}{4}\xi)-\sqrt{-\Delta}}\right)$$
$$\times\left(p+4qr\frac{\sin(\frac{\sqrt{-\Delta}}{4}\xi)\cos(\frac{\sqrt{-\Delta}}{4}\xi)}{-2p\sin(\frac{\sqrt{-\Delta}}{4}\xi)\cos(\frac{\sqrt{-\Delta}}{4}\xi)+2\sqrt{-\Delta}\cos^2(\frac{\sqrt{-\Delta}}{4}\xi)-\sqrt{-\Delta}}\right),$$

where $\xi=\frac{1}{L}x-\frac{(p^2+8qr+6)}{(B_1-a_0A_1)}\frac{t}{\tau}$, and a_0 is an arbitrary constant.

According to the values of solutions of the type, we obtain the following exact traveling wave solutions for Equation (1):

$$u_{25}(x,t)=a_0+\frac{12p^2d(B_1-a_0A_1)}{A_1(p^2+6)}\left(\frac{\cosh(p\xi)-\sinh(p\xi)}{(d+\cosh(p\xi)-\sinh(p\xi))^2}\right),$$

$$u_{26}(x,t)=a_0+\frac{12p^2d(B_1-a_0A_1)}{A_1(p^2+6)}\left(\frac{\cosh(p\xi)+\sinh(p\xi)}{(d+\cosh(p\xi)+\sinh(p\xi))^2}\right).$$

where $\xi=\frac{1}{L}x-\frac{(p^2+6)}{(B_1-a_0A_1)}\frac{t}{\tau}$, a_0 is an arbitrary constant.

According to the values of the type 4, we obtain the following exact traveling wave solution for (1):

$$u_{27}(x,t)=a_0-\frac{2q(B_1-a_0A_1)}{A_1}\left(\frac{q}{(q\xi+C_1)^2}\right),$$

where $\xi=\frac{1}{L}x-\frac{6}{(B_1-a_0A_1)}\frac{t}{\tau}$.

Exact traveling wave solutions of Equation (1) for Case 2

By using the Case 2 and according to the values of solutions of type 1, we obtain the following exact traveling wave solutions for Equation(1) :

$$u_1(x,t)=a_0+\frac{12qr(B_1-a_0A_1)}{A_1(8qr+6)}\coth^2(\sqrt{-qr}\xi),$$
$$u_2(x,t)=a_0+\frac{12qr(B_1-a_0A_1)}{A_1(8qr+6)}\tanh^2(\sqrt{-qr}\xi),$$

$$u_3(x,t)=a_0+\frac{12qr(B_1-a_0A_1)}{A_1(8qr+6)}\frac{1}{[\tanh(\sqrt{-4qr}\xi)\pm i\,\mathrm{sec}\,h(\sqrt{-4qr}\xi)]^2},$$
$$u_4(x,t)=a_0+\frac{12qr(B_1-a_0A_1)}{A_1(8qr+6)}\frac{1}{[\coth(\sqrt{-4qr}\xi)\pm\mathrm{csc}\,h(\sqrt{-4qr}\xi)]^2},$$
$$u_5(x,t)=a_0+\frac{48qr(B_1-a_0A_1)}{A_1(8qr+6)}\frac{1}{[\tanh(\frac{\sqrt{-qr}}{2}\xi)\pm\coth(\frac{\sqrt{-qr}}{2}\xi)]^2},$$
$$u_6(x,t)=a_0+\frac{12qr(B_1-a_0A_1)}{A_1(8qr+6)}\left[\frac{A\sinh(\sqrt{-4qr}\xi)+B}{-A\cosh(\sqrt{-4qr}\xi)+\sqrt{A^2+B^2}}\right]^2,$$
$$u_7(x,t)=a_0+\frac{12qr(B_1-a_0A_1)}{A_1(8qr+6)}\left[\frac{A\sinh(\sqrt{-4qr}\xi)+B}{A\cosh(\sqrt{-4qr}\xi)+\sqrt{B^2-A^2}}\right]^2.$$

where A and B are two non-zero real constants satisfying $B^2-A^2>0$,

$$u_8(x,t)=u_2(x,t)$$
$$u_9(x,t)=u_1(x,t)$$
$$u_{10}(x,t)=a_0+\frac{12qr(B_1-a_0A_1)}{A_1(8qr+6)}\left[\frac{\sinh(\sqrt{-4qr}\xi)\pm i}{\cosh(\sqrt{-qr}\xi)}\right]^2,$$
$$u_{11}(x,t)=a_0+\frac{12qr(B_1-a_0A_1)}{A_1(8qr+6)}\left[\frac{\cosh(\sqrt{-4qr}\xi)\pm 1}{\sinh(\sqrt{-qr}\xi)}\right]^2,$$
$$u_{12}(x,t)=a_0+\frac{48qr(B_1-a_0A_1)}{A_1(8qr+6)}\left(\frac{\cosh(\sqrt{-4qr}\xi)}{\sinh(\sqrt{-qr}\xi)}\right)^2.$$

According to the values of the solutions of the type 2, we obtain the exact traveling wave solutions for Equation (1):

$$u_{13}(x,t)=a_0-\frac{12qr(B_1-a_0A_1)}{A_1(8qr+6)}\cot^2(\sqrt{qr}\xi),$$
$$u_{14}(x,t)=a_0-\frac{12qr(B_1-a_0A_1)}{A_1(8qr+6)}\tan^2(\sqrt{qr}\xi),$$
$$u_{15}(x,t)=a_0-\frac{12qr(B_1-a_0A_1)}{A_1(8qr+6)}\left[\tan(\sqrt{4qr}\xi)\pm\sec(\sqrt{4qr}\xi)\right]^{-2},$$
$$u_{16}(x,t)=a_0-\frac{12qr(B_1-a_0A_1)}{A_1(8qr+6)}\left[\cot(\sqrt{4qr}\xi)\pm\csc(\sqrt{4qr}\xi)\right]^{-2}$$

$$u_{17}(x,t)=a_0-\frac{48qr(B_1-a_0A_1)}{A_1(8qr+6)}\left[\tan(\frac{\sqrt{qr}}{2}\xi)-\cot(\frac{\sqrt{qr}}{2}\xi)\right]^{-2},$$

$$u_{18}(x,t)=a_0-\frac{12qr(B_1-a_0A_1)}{A_1(8qr+6)}\left[\frac{\pm\sqrt{A^2-B^2}-A\cos(\sqrt{4qr}\xi)}{B+A\sin(\sqrt{4qr}\xi)}\right]^{-2},$$

$$u_{19}(x,t)=a_0-\frac{12qr(B_1-a_0A_1)}{A_1(8qr+6)}\left[\frac{\pm\sqrt{A^2-B^2}+A\cos(\sqrt{4qr}\xi)}{B+A\sin(\sqrt{4qr}\xi)}\right]^{-2},$$

where A and B are two non-zero real constants satisfying $A^2 - B^2 > 0$,

$$u_{20}(x,t)=u_{14}(x,t),$$
$$u_{21}(x,t)=u_{13}(x,t),$$

$$u_{22}(x,t)=a_0-\frac{12qr(B_1-a_0A_1)}{A_1(8qr+6)}\left[\frac{\sin(\sqrt{4qr}\xi)\pm1}{\cos(\sqrt{qr}\xi)}\right]^{2},$$

$$u_{23}(x,t)=a_0-\frac{12qr(B_1-a_0A_1)}{A_1(8qr+6)}\left[\frac{\cos(\sqrt{4qr}\xi)\pm1}{\sin(\sqrt{qr}\xi)}\right]^{2},$$

$$u_{24}(x,t)=u_{13}(x,t).$$

$$\xi=\frac{1}{L}x-\frac{(8qr+6)}{(B_1-a_0A_1)}\frac{t}{\tau}.$$

Exact traveling wave solutions of Equation (1) for Case 3

By using the Case 3 and according to the values of the solutions of the Type 1, we obtain the following exact traveling wave solutions for Equation (1):

$$u_1(x,t)=u_2(x,t)=a_0-\frac{a_2r}{q}\left[\tanh^2(\sqrt{-qr}\xi)+\coth^2(\sqrt{-qr}\xi)\right],$$

$$u_3(x,t)=a_0-\frac{a_2r}{q}\left[\begin{array}{l}\left(\tanh(\sqrt{-4qr}\xi)\pm i\,\mathrm{sech}(\sqrt{-4qr}\xi)\right)^2\\+\left(\tanh(\sqrt{-4qr}\xi)\pm i\,\mathrm{sech}(\sqrt{-4qr}\xi)\right)^{-2}\end{array}\right],$$

$$u_4(x,t)=a_0-\frac{a_2r}{q}\left[\begin{array}{l}\left(\coth(\sqrt{-4qr}\xi)\pm\mathrm{csch}(\sqrt{-4qr}\xi)\right)^2\\+\left(\coth(\sqrt{-4qr}\xi)\pm\mathrm{csch}(\sqrt{-4qr}\xi)\right)^{-2}\end{array}\right],$$

$$u_5(x,t)=a_0-\frac{a_2r}{4q}\left[\left(\tanh(\frac{\sqrt{-qr}}{2}\xi)\pm\coth(\frac{\sqrt{-qr}}{2}\xi)\right)^2\right]-\frac{4a_2r}{q}\left[\left(\tanh(\frac{\sqrt{-qr}}{2}\xi)\pm\coth(\frac{\sqrt{-qr}}{2}\xi)\right)^{-2}\right],$$

$$u_6(x,t)=a_0-\frac{a_2r}{q}\left[\left[\frac{\sqrt{A^2+B^2}-A\cosh(\sqrt{-4qr}\xi)}{B+A\sinh(\sqrt{-4qr}\xi)}\right]^2+\left[\frac{B+A\sinh(\sqrt{-4qr}\xi)}{\sqrt{A^2+B^2}-A\cosh(\sqrt{-4qr}\xi)}\right]^{-2}\right],$$

$$u_7(x,t)=a_0-\frac{a_2r}{q}\left[\left[\frac{\sqrt{B^2-A^2}+A\cosh(\sqrt{-4qr}\xi)}{B+A\sinh(\sqrt{-4qr}\xi)}\right]^2+\left[\frac{B+A\sinh(\sqrt{-4qr}\xi)}{\sqrt{B^2-A^2}+A\cosh(\sqrt{-4qr}\xi)}\right]^{-2}\right].$$

where A and B are two non-zero real constants satisfying $B^2 - A^2 > 0$,

$$u_8(x,t)=u_9(x,t)=u_1(x,t),$$

$$u_{10}(x,t)=a_0-\frac{a_2r}{q}\left[\left(\frac{\cosh(\sqrt{-qr}\xi)}{\sinh(\sqrt{-4qr}\xi)\pm i}\right)^2+\left(\frac{\sinh(\sqrt{-4qr}\xi)\pm i}{\cosh(\sqrt{-qr}\xi)}\right)^2\right],$$

$$u_{11}(x,t)=a_0-\frac{a_2r}{q}\left[\left(\frac{\sinh(\sqrt{-qr}\xi)}{\cosh(\sqrt{-4qr}\xi)\pm1}\right)^2+\left(\frac{\cosh(\sqrt{-4qr}\xi)\pm1}{\sinh(\sqrt{-qr}\xi)}\right)^2\right],$$

$$u_{12}(x,t)=a_0-\frac{a_2r}{q}\left[\left(\frac{\sinh(\sqrt{-qr}\xi)}{\cosh(\sqrt{-4qr}\xi)}\right)^2+\left(\frac{\cosh(\sqrt{-4qr}\xi)}{\sinh(\sqrt{-qr}\xi)}\right)^2\right].$$

According to the value of the solutions of the type, we obtain the exact traveling wave solutions for Equation (1):

$$u_{13}(x,t)=u_{14}(x,t)=a_0+\frac{a_2r}{q}\left(\tan^2(\sqrt{qr}\xi)+\cot^2(\sqrt{qr}\xi)\right),$$

$$u_{15}(x,t)=a_0+\frac{a_2r}{q}\left[\left(\tan(\sqrt{4qr}\xi)\pm\sec(\sqrt{4qr}\xi)\right)^2+\left(\tan(\sqrt{4qr}\xi)\pm\sec(\sqrt{4qr}\xi)\right)^{-2}\right],$$

$$u_{16}(x,t)=a_0+\frac{a_2r}{q}\left[\left(\cot(\sqrt{4qr}\xi)\pm\mathrm{csc}(\sqrt{4qr}\xi)\right)^2+\left(\cot(\sqrt{4qr}\xi)\pm\mathrm{csc}(\sqrt{4qr}\xi)\right)^{-2}\right],$$

$$u_{17}(x,t)=a_0+\frac{a_2r}{4q}\left(\tan\left(\frac{\sqrt{qr}}{2}\xi\right)-\cot\left(\frac{\sqrt{qr}}{2}\xi\right)\right)^2+\frac{4a_2r}{q}\left(\tan\left(\frac{\sqrt{qr}}{2}\xi\right)-\cot\left(\frac{\sqrt{qr}}{2}\xi\right)\right)^{-2},$$

$$u_{18}(x,t)=a_0+\frac{a_2r}{q}\left[\left(\frac{\pm\sqrt{A^2-B^2}-A\cos(\sqrt{4qr}\xi)}{B+A\sin(\sqrt{4qr}\xi)}\right)^2+\left(\frac{B+A\sin(\sqrt{4qr}\xi)}{\pm\sqrt{A^2-B^2}-A\cos(\sqrt{4qr}\xi)}\right)^2\right],$$

$$u_{19}(x,t)=a_0+\frac{a_2r}{q}\left[\left(\frac{\pm\sqrt{A^2-B^2}+A\cos(\sqrt{4qr}\xi)}{B+A\sin(\sqrt{4qr}\xi)}\right)^2+\left(\frac{B+A\sin(\sqrt{4qr}\xi)}{\pm\sqrt{A^2-B^2}+A\cos(\sqrt{4qr}\xi)}\right)^2\right].$$

where A and B are two non-zero real constants satisfying $A^2-B^2>0$,

$$u_{20}(x,t)=u_{21}(x,t)=u_{13}(x,t),$$

$$u_{22}(x,t)=a_0+\frac{a_2r}{q}\left[\left(\frac{\cos(\sqrt{qr}\xi)}{\sin(\sqrt{4qr}\xi)\pm1}\right)^2+\left(\frac{\sin(\sqrt{4qr}\xi)\pm1}{\cos(\sqrt{qr}\xi)}\right)^2\right],$$

$$u_{23}(x,t)=a_0+\frac{a_2r}{q}\left[\left(\frac{\sin(\sqrt{qr}\xi)}{\cos(\sqrt{4qr}\xi)\pm1}\right)^2+\left(\frac{\cos(\sqrt{4qr}\xi)\pm1}{\sin(\sqrt{qr}\xi)}\right)^2\right],$$

$$u_{24}(x,t)=u_{13}(x,t).$$

$$where\,\xi = \frac{1}{L}x - \left(\frac{-12q^2}{a_2 A_1}\right)\frac{t}{\tau},\ r = \frac{3}{4a_2 q}(2a_0 q^2 - a_2 - 2q^2(\frac{B}{A}))$$

DISCUSSION AND CONCLUSION

In this section, we will compare some of our results obtained in this article with the well-known results obtained in (Sekulic et al., 2011) with the interchanges $r \leftrightarrow b,\ A_1 \leftrightarrow A, B_1 \leftrightarrow B$ as follows:

1. If we set *p = 0* and *q* = 1 in our results $u_1(x,t)$ and $u_{13}(x,t)$, we have respectively the special forms:

$$u_1(x,t) = a_0 - a_2 \tanh^2(\sqrt{-r}\,\xi), \tag{10}$$

And

$$u_{13}(x,t) = a_0 + a_2 \tan^2(\sqrt{r}\,\xi), \tag{11}$$

Where

$$r = \frac{3}{4a_2}(2a_0 - a_2 - 2\frac{B_1}{A_1}),\quad \xi = \frac{1}{L}x + (\frac{12}{a_2 A_1})\frac{t}{\tau}. \tag{12}$$

We have noted that the results (10) and (11) are equivalent to the well-known results (10) and (11) obtained in (Sekulic et al., 2011) respectively.

2. If we set *q* = 1 in our results $u_1(x,t)$ and $u_{13}(x,t)$, we have respectively the special forms:

$$u_1(x,t) = a_0 + \frac{12r}{A_1}\left(\frac{B_1 - a_0 A_1}{8r+6}\right)\coth^2(\sqrt{-r}\,\xi), \tag{13}$$

and

$$u_{13}(x,t) = a_0 - \frac{12r}{A_1}\left(\frac{B_1 - a_0 A_1}{8r+6}\right)\cot^2(\sqrt{r}\,\xi), \tag{14}$$

where *r* is an arbitrary constant, while

$$\xi = \frac{1}{L}x - (\frac{8r+6}{B_1 - a_0 A_1})\frac{t}{\tau}.$$

After our careful revisions for the article (Sekulic et al, 2011), we found a minor error in the results (12) and (13) of this reference, which can be corrected here to become respectively as:

$$u(x,t) = a_0 + \frac{12b}{A}\left(\frac{B - a_0 A}{8b+6}\right)\coth^2(\sqrt{-b}\,\xi), \tag{15}$$

and

$$u(x,t) = a_0 - \frac{12b}{A}\left(\frac{B - a_0 A}{8b+6}\right)\cot^2(\sqrt{b}\,\xi), \tag{16}$$

In this case our above results (13) and (14) are equivalent to the corrected results (15) and (16) respectively.

3- If we set *q* = 1 in our results $u_1(x,t)$ and $u_{13}(x,t)$, we have respectively the special forms:

$$u_1(x,t) = a_0 - \frac{3}{4}(2a_0 - a_2 - 2\frac{B_1}{A_1})\left\{\tanh^2(\sqrt{-r}\,\xi) + \coth^2(\sqrt{-r}\,\xi)\right\}, \tag{17}$$

And

$$u_{13}(x,t) = a_0 + \frac{3}{4}(2a_0 - a_2 - 2\frac{B_1}{A_1})\left\{\tan^2(\sqrt{r}\,\xi) + \cot^2(\sqrt{r}\,\xi)\right\}, \tag{18}$$

where *r* and ξ have the same forms of (12). We have noted that the results (17) and (18) are equivalent to the results (14) and (15) obtained in (Sekulic et al., 2011) respectively.

From these discussions, we deduce that the exact solutions of Equation (1) obtained in (Sekulic et al., 2011) using the modified extended tanh-function method are special cases of some of our results obtained in the present article using the improved Riccati equation mapping method. Furthermore, the proposed method in this article has been played an important role in obtaining many families of exact solutions of Equation (1) which look new and recover the well-known exact solutions obtained in (Sekulic et al., 2011) using the modified extended tanh-function method. Finally, all the solutions obtained in the present article have been checked with Maple or Mathematica by putting them back into the original Equation (1).

Numerical examples

In this section, we will give some numerical examples to illustrate some of our obtained results in this article. To this end, we select some special values of the parameters obtained in the exact traveling wave solutions of Equation (1) for case 1. So, we choose the following values:

$$C_0 = 4,\ Z = 3,\ G_0 = 1,\ \delta = 6,\ R = 2,\ L = \frac{1}{2}, \tau = \frac{1}{2},\ p = 8, r = 3$$

,

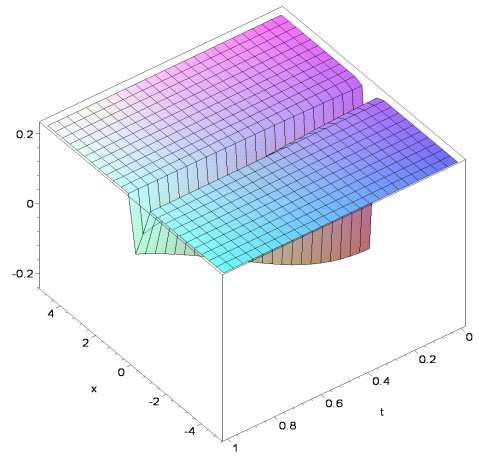

$u_1(x,t)$

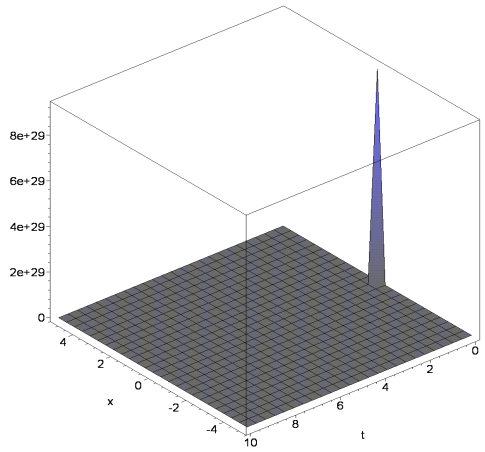

$u_2(x,t)$

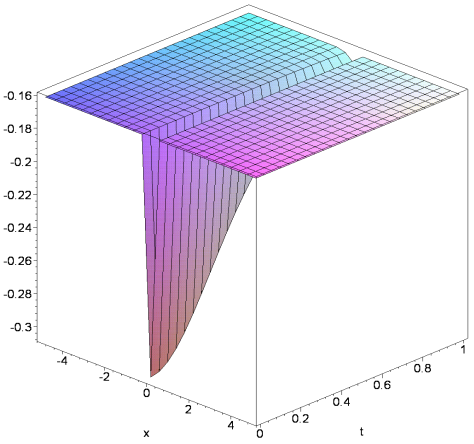

$\mathrm{Re}\,u_3(x,t)$

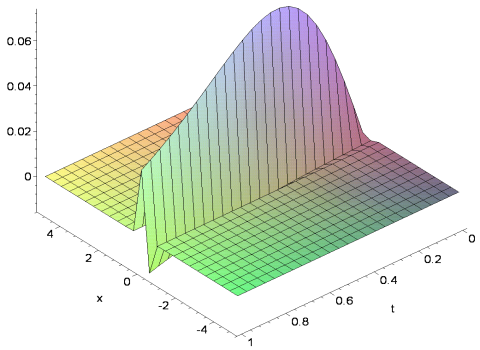

$\mathrm{Im}\,u_3(x,t)$

Figure 1. Some numerical solutions of Equation (1).

a_0 = 0.5, and using the computer programs, such as the Matlab, to draw diagrams for some of our results (Figure 1)

ACKNOWLEDGEMENT

The authors wish to thank the referees for their comments.

REFERENCES

Abdou MA (2007). The extended tanh method and its applications for solving nonlinear physical models. Appl. Math. Comput. 190(1):988-996.

Ablowitz MJ, Clarkson PA (1991). Solitons, nonlinear evolution equations and inverse scattering transform, Cambridge University Press. New York.

Aslan I (2010). A note on the (G'/G) -expansion method again. Appl. Math. Comput. 217(2):937-938.

Aslan I (2011). Comment on application of exp-function method (3+1)dimensional nonlinear evolution equation.[Comput Math. Appl. 56 (2008) 1451-1456], Comput. Math. Appl. 61(6):1700-1703.

Aslan I (2011). Exact and explicit solutions to the discrete nonlinear Schrödinger equation with a saturable nonlinearity. Phys. Lett. A. 375(47):4214-4217.

Aslan I (2012a). Some exact solutions for Toda type lattice differential equations using the improved (G'/G)– expansion method," Math. Methods Appl. Sci. 35(4): 474-481.

Aslan I (2012b). The discrete (G'/G) -expansion method applied to the differential-difference Burgers equation and the relativistic Toda lattice system. Numer. Methods Par. Diff. Eqs. 28(1):127-137.

Ayhan B, Bekir A (2012). The (G'/G) -expansion method for the nonlinear lattice equations. Commu. Nonlinear Sci. Numer. Simul. 17(9):3490-3498.

Bekir A (2008). Application of the (G'/G) -expansion method for nonlinear evolution equations. Phys. Lett. A. 372(19):3400-3406.
Bekir A (2009). The exp-function for Ostrovsky equation. Inter. J. Nonlinear Sci. Numer. Simul. 10:735-739.
Bekir A (2010). Application of exp-function method for nonlinear differential-difference equations. Appl. Math. Comput. 215(11):4049-4053,
Chen Y, Wang Q (2005). Extended Jacobi elliptic function rational expansion method and abundant families of Jacobi elliptic function solutions to (1+1)-dimensional dispersive long wave equation. Chaos, Solitons Fractals. 24(3):745-757.
Fan E (2000). Extended tanh-function method and its applications to nonlinear equations Phys. Lett. A. 277:212-218.
He JH, Wu XH (2006). Exp-function method for nonlinear wave equations. Chaos, Solitons Fractals. 30(3):700-708.
Hirota R (1971).Exact solutions of the KdV equation for multiple collisions of solutions. Phys. Rev. Lett. 27:1192-1194.
Kudryashov NA (1988). Exact solutions of a generalized evolution of wave dynamics. J. Appl. Math. Mech. 52:361-365.
Kudryashov NA (1990). Exact solutions of a generalized Kuramoto-Sivashinsky equation. Phys. Lett. A. 147(5-6):287-291.
Kudryashov NA (1991). On types of nonlinear nonintegrable equations with exact solutions. Phys. Lett. A. 155(4-5):269-275.
Liu S, Z, Fu Z, Zhao Q (2001). Jacobi elliptic function expansion method and periodic wave solutions of nonlinear wave equations. Phys. Lett. A. 289(1-2):69-74.
Lu D (2005). Jacobi elliptic function solutions for two variant Boussinesq equations, Chaos, Solitons Fractals. 24(5):1373.
Miura MR (1978). Backlund transformation, Springer, Berlin, Germany.
Sataric MV, Llic DI, Ralevic N, Tuszynshi JA (2009). A nonlinear model of ionic wave propagation along microtubules. Eur. Biophys. J. 38(5):637-647.
Sataric MV, Sekulic DL, Zivanov MB (2010). Solitonic ionic currents along microtubules. J. Comput. Theor. Nanosci. 7:2281-2290.
Sekulic DL, Sataric BM, Tuszynshi JA, Sataric MV, (2011). Nonlinear ionic pulses along microtubules. Eur. Phys. J. E. 34(5):49.
Sekulic DL, Sataric MV, Zivanov MB (2011). Symbolic computation of some new nonlinear partial differential equations of nanobiosciences using modified extended tanh-function method. Appl. Math. Comput. 218:3499-3506.
Wang M, X. Li X, Zhang JJ (2008). The (G'/G)-expansion method and traveling wave solutions of nonlinear evolution equations in mathematical physics," Phys. Lett. A. 372:417-423.
Weiss J, Tabor T, Carnevale G (1983). The Painlevé property for partial differential equations. J. Math. Phys. 24(3):552-526.
Yusufoglu E (2008).New solitary for the MBBM equations using exp-function method. Phys. Lett. A. 372:442-446.
Yusufoglu E, Bekir A (2008). Exact solutions of coupled nonlinear Klein-Gordon equations. Math. Comput. Model. 48:1694-1700.
Zayed EME (2009). The (G'/G)-expansion method and its applications to some nonlinear evolution equations in the mathematical physics. J. Appl. Math. Comput. 30:89-103.
Zayed EME (2010). Traveling wave solutions for higher dimensional nonlinear evolution equations using the (G'/G)-expansion method. J. Appl. Math. Inf. 28:383-395.
Zayed EME, Arnous AH (2013). Many exact solutions for nonlinear dynamics of DNA model using the generalized Riccati equation mapping method. Sci. Res. Ess. 8:340-346.
Zhang S, Tong JL, Wang W (2008). A generalized (G'/G)-expansion method for the mKdV equation with variable coefficients. Phys. Lett. A. 372:2254-2257.
Zhang S, Xia T (2008). A further improved tanh function method exactly solving the (2+1)- dimensional dispersive long wave equations, Appl. Math. E-Notes. 8:58-66.
Zhu SD (2008). The generalized Riccati equation mapping method in nonlinear evolution equation: application to (2+1)-dimensional Boiti-lion-Pempinelle equation. Chaos, Solitons Fractals. 37:1335-1342.

academicJournals

Vol. 8(22), pp. 1256-1265, 16 June, 2013
DOI: 10.5897/IJPS2013.3911
ISSN 1992-1950 © 2013 Academic Journals
http://www.academicjournals.org/IJPS

International Journal of Physical Sciences

Full Length Research Paper

Decentralized management of a multi-source electrical system: A multi-agent approach

Abdoul K. MBODJI*, Mamadou L. NDIAYE and Papa A. NDIAYE

Centre International de Formation et de Recherche en Energie Solaire (C.I.F.R.E.S), ESP BP 5085 Dakar-Fann, Sénégal.

Accepted 3 June, 2013

The objective of this paper was design and implementation of a self-adaptive management system of a set of production sources in a changing and unpredictable energy demand environment. The strategy proposed made it possible to achieve optimal management of the energy resource production of the electrical system facing the changing demand. After showing the need to follow «intelligently» the behavior of different entities of the electrical system by a distributed, collaborative and self-adaptive model, the emphasis was placed on the modeling of an energy management multi-agent system. The proposed model allowed the overall production to be optimized in relation with the demand profile and in function of a cost or greenhouse gas reduction criterion. The flexibility of this model could in priority allow both the integration of multi-objectives optimization and that of information.

Key words: Energy, modeling, complex system, multi-agent system, optimization, multi-source system, greenhouse gas.

INTRODUCTION

Electrical energy management goes with the protection, monitoring and control of the entire electrical network. For the operator, the question also concerns the optimizing of the energy consumption cost of different production sources without any prejudice for the activity. This requires effective and real-time control of the overall electrical system parameters. Modern solutions to this control need are products and services using information and communication technologies based on the paradigm of–smart systems, such as data loggers and supervision and control software. Research has been done on the multi-source decentralized power grid management optimization. Logenthiran et al. (2012), present a Multi-Agent System (MAS) for the real-time operation of a microgrid. The multi-agent model proposed in this paper, provides a common communication interface for the entire components of the microgrid. Implementation the MAS allows not only to maximize energy production from local distributed generators, but also to minimize the microgrid operating cost to be minimized. The recent studies by Monica et al. (2012); Mao et al. (2011); and Pipattanasomp et al. (2009) present an optimal design and implementation method for the intelligent management of electrical distribution networks. The research mentioned focuses on microgrids especially in the electrical distribution part. It would be interesting to enlarge the fieldwork and integrate both transport and production parts into energy management in order to take advantage of more room for maneuver and flexibility in the management system.

Other MAS applications allowing a diagnosis of disturbances on the grid to be made were presented in the work of Nagata and Sasaki (2002) and Wang (2001). An application that makes it possible to monitor the power system is presented in the work of Cristaldi et al. (2003), a secondary voltage control system in that of Phillips et al. (2006) and a visualization power system in that of Dimeas and Hatziargyriou (2005a).

*Corresponding author. E-mail: akmbodji@yahoo.fr.

Some other studies, to mention only those of Dimeas and Hatziargyriou (2005b); Dimeas and Hatziargyriou (2004) and Butler-Purry et al. (2004), focus on the control of the micro network operation from a MAS. However, most of that work was applied to power grid using PV generators, batteries and controllable loads. Besides, the emphasis was more on technical than on economic and environmental aspects such as the reduction of operating costs and the amount of greenhouse gases (GHG) emitted by the electrical network.

The present paper proposes a model of generic system management of electrical systems that can be applied to a micro grid as well as to a macro grid. This model can be implemented in a real system thanks to advanced communication techniques, software agents can be embedded in different sources of power generation and loads. These agents cooperate and make decisions together to optimize system management both in technical and economic terms, taking into account technological constraints and resources availability. So, the contribution of this paper is to implement an optimal management platform of decentralized electrical systems minimizing the production cost or the amount of GHG emissions released by the power plants.

MATERIALS AND METHODS

Presentation of power grid (PG)

PG as shown in Figure 1 is a distributed system on several sites S_k. Each site consists of several power plant $C_{j\,(Sk)}$ and each plant site consists of several production generators $G_{i(Cj(Sk))}$. Each generator produces power P_i and the total power supplied by the power grid is given by Equation (1):

$$P_f^T = \sum_{k=1}^{S}\left(\sum_{j=1}^{C}\left(\sum_{i=1}^{G} P_i\right)\right) \quad (1)$$

Where, G: is the number of generators in power plant $C_{j(Sk)}$; C: is the number of power plants in a site S_k; S: is the number of network sites.

The total power demand is given by the following Equation (2):

$$P_D^T = \sum_{k=1}^{H}\left(\sum_{j=1}^{M}\left(\sum_{i=1}^{B} P_{\delta_i}\right)\right) \quad (2)$$

With: B: is the number of clients managed by a low-voltage departure d_i; M: is the number of low-voltage departures; H: is the number of high-voltage departures of the grid. The total power supplied P_S^T by the network at t time is then given by Equation (3):

$$P_S^T = P_D^T + Losses \quad (3)$$

Where, the losses are due to the technical or not technical losses. The production cost of energy sources as shown in Equation (4) takes into account the costs of fuel, oil and maintenance.

$$C_P = C_f + C_o + C_m \quad (4)$$

C_f , cost of fuel consumption; C_o , cost of oil consumption; C_m , cost of maintenance.

Estimation of the quantities of greenhouse gas emissions

The estimation of emissions from fossil fuels combustion in fossil energy sources is presented in three levels of approaches in the 2006 Guidelines (Amit et al., 2006).

Level 1 approach

It requires the knowledge of data such as the quantity of fuel burned per unit of energy and a default emission factor. The associated equation is:

$$E_{G,F} = Q_F \times F.E_{G,F} \quad (5)$$

The total emission of greenhouse gases due to combustion (E_G) is obtained by adding the GHG emissions attributable to the combustion of each fuel (Richalet, 1987). This results in the following Equation (6):

$$E_G = \sum_F E_{G,F} \quad (6)$$

Level 2 approach

In Level 2, the default emission factors from Level 1 are simply replaced by specific emission factors of the corresponding country (Amit et al., 2006).

Level 3 approach

The Level 3 approach considers an emission factor per fuel and per technology (Amit et al., 2006). The mathematical model associated with this approach is given by Equation (7):

$$E_{G,F,T} = Q_{F,T} \times F.E_{G,F,T} \quad (7)$$

The total emission of GHG generated by different technologies is given by Equation (8):

$$E_{G,F} = \sum_T E_{G,F,T} \quad (8)$$

Typology and structure of agents

The approach is to translate the problem of vector processing exchanges of energy flow in an agent space where the system entities cooperate with each other. A situated approach, cooperative and decentralized, is proposed for power system management. This is an approach into which an agent «Source Agent» (Ag_S) is associated with each energy source and an agent

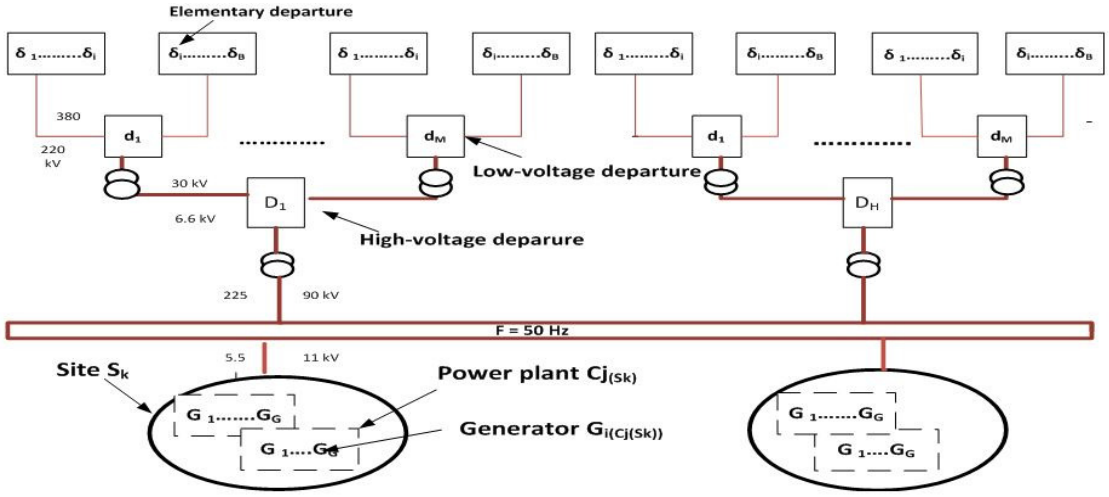

Figure 1. Power grid.

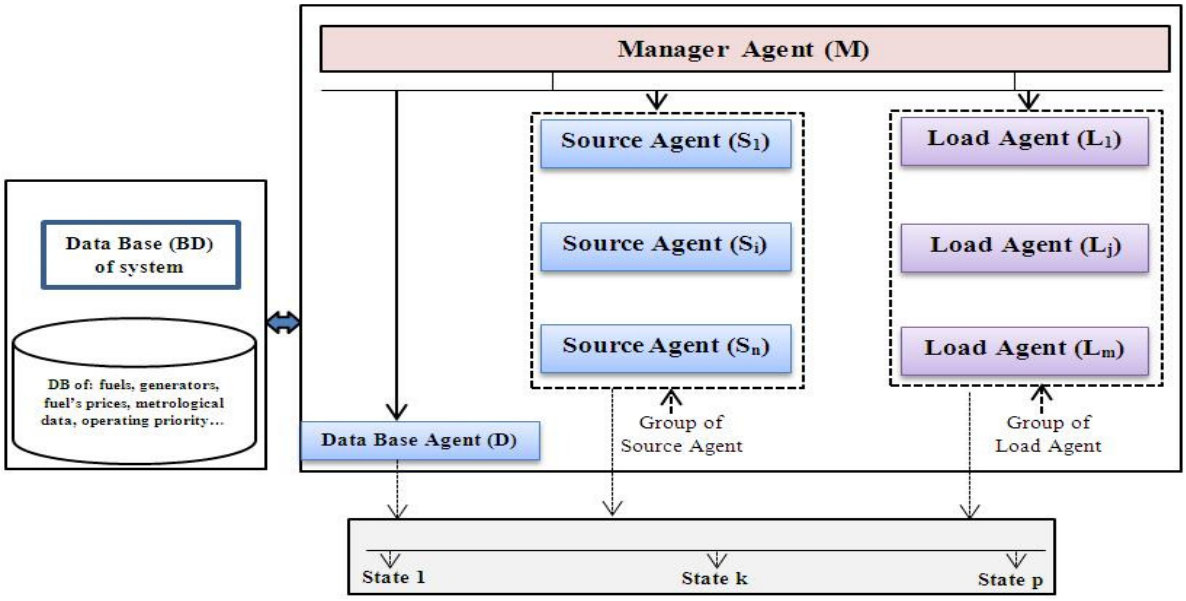

Figure 2. General architecture of the platform developed by a multi agent development kit (MADKIT).

«Load Agent» (Ag_L) is associated with each low-voltage departure.

The proposed architecture (Figure 2) is hybrid and is divided in two layers: the first layer consists of two types of reactive agents (Source Agent and Load Agent). Each Ag_{S_i} (i ∈ [1 - N]) and each Ag_{L_k} (k ∈ [1 - K]), have their own characteristics (Table 1). The second layer consists of a cognitive agent called «Manager Agent» (Ag_M) and a reactive agent called «Data Base Agent» (Ag_D), which manages the database of information handled by Source Agent and Load Agent.

Agent priority is a decisive parameter in the working of the management system. It allows the agents, depending on their priority, to participate or not in meeting the demand. Priority (p_{Si}) of Source Agent is a parameter which depends on the optimization criterion, the availability of the source, the source production cost and / or the amount of GHG released (Equation 9). This is a real value between zero (0) and one (1). A production source has all the higher priority as the value of its priority is closer to one (1).

The priority of Load Agent varies between zero (0), one (1), two (2) and three (3). A Load Agent has all the higher priority as the priority value of its priority is greater. Departures supplying sensitive areas (major national institutions, hospitals, etc.) have a higher priority equal to three (3). Departures supplying secondary areas (industrial, etc.) have a priority equal to two (2). Departures supplying non-priority areas (residential, etc.) have a priority equal to one (1).

Table 1. Attribute of source agent and load agent.

Source agent (Ag_{S_i})	Load agent (Ag_{L_k})
I_{S_i} : Identification number	I_{D_k} **:** Identification number
Comb **:** consumed fuel	P_{L_k} : Power demand (MW)
P_{S_i} : Power supply (MW)	p_{Lk}**:** operation priority
A_{Si} : availability	
C_{Si} : cost per kWh (FCFA/kWh)	
Q_{Si} : quantity of CO_2 released to produce 1 kWh (g/kWh)	
p_{Si} **:** operation priority	

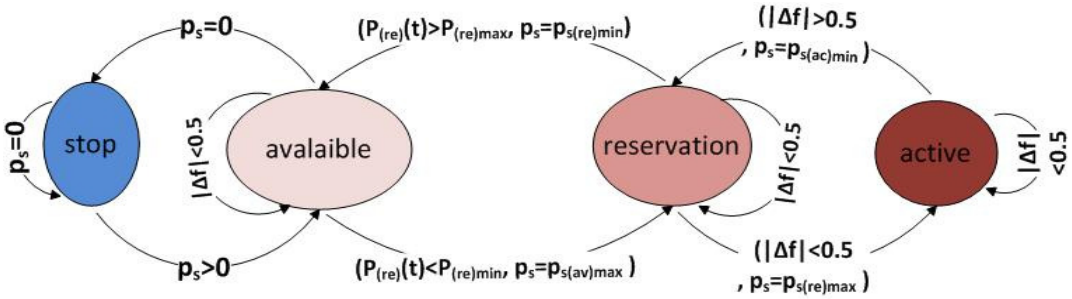

Figure 3. Behavioral model of source agent.

Source Agent can be in four (4) different states (Figure 3): active (ac), reserve (re) or standby, available (av) and stop (st). In each state, the instantaneous power of the source agent is delimited by a minimum and a maximum allowable power ($P_{(state)min} \leq P_{(state)}(t) \leq P_{(state)max}$). The numbers of source agents in state ac, re, av and st are respectively denoted N_1, N_2, N_3 and N_4. Equation 10 gives the instantaneous power reserve which is the sum of the powers of sources agents in the reserve state at t time. The reserve instantaneous power $P_{(re)}(t)$ should always be remaining between a minimum value $P_{(re)\min}$ and a maximum value $P_{(re)\max}$. Production sources that are in the reserve state can regulate the frequency around 50 Hz.

$$f:\{1,-1\}\times\{0,1\}\times[0,1]\rightarrow[0,1]$$
$$v_1,v_2,v_3 \rightarrow p_s = f(v_1,v_2,v_3) = v_2\left(1-|v_1\times v_3|\right) \quad (9)$$

v_1 is optimization criterion, v_1 =1 or -1, $v_1 \in \{-1\ 1\}$; v_2 is the source availability, v_2 =1 if the source is available otherwise v_2 =0, $v_2 \in \{0\ 1\}$; Let $\{C_{S_i}\}$ be the set of kWh costs associated with energy sources of the system and $Max\{C_{S_i}\}$ the maximum of this set. Let $\{Q_{S_i}\}$ be the set of all the amounts GHGs released associated with energy sources of the system and $Max\{Q_{S_i}\}$ the maximum of this set. v_3 is equal to the following value:

$v_3 = \dfrac{C_{S_i}}{Max\{C_{S_i}\}}$ or $v_3 = \dfrac{Q_{S_i}}{Max\{Q_{S_i}\}}$ $i = \{1,2,.....,N\}$ by construction $v_3 = [0\ \ 1]$.

$$P_{(re)\min} \leq P_{(re)}(t) = \sum_{i=1}^{N_2} P_{(re)i}(t) \leq P_{(re)max} \quad (10)$$

Model system management

The main objective of the management system is to minimize the cost per kWh or reduce the amount GHG generated by the system with the constraint of maintaining the equilibrium of the system which requires the frequency in a fixed interval. Satisfaction function of system (SF) is a Boolean variable, it is equal to one (1) if the frequency of the electrical system is in [49.5 50.5] otherwise it is equal to zero (0). The Manager Agent is a cognitive agent and supervises staff departures and production sources, and their associated states (Figure 4). It plays a major role in the timing and coherence of the activities of different agents. It is involved in the cooperation between the different agents of the system. It supervises and coordinates the operation of the system agents.

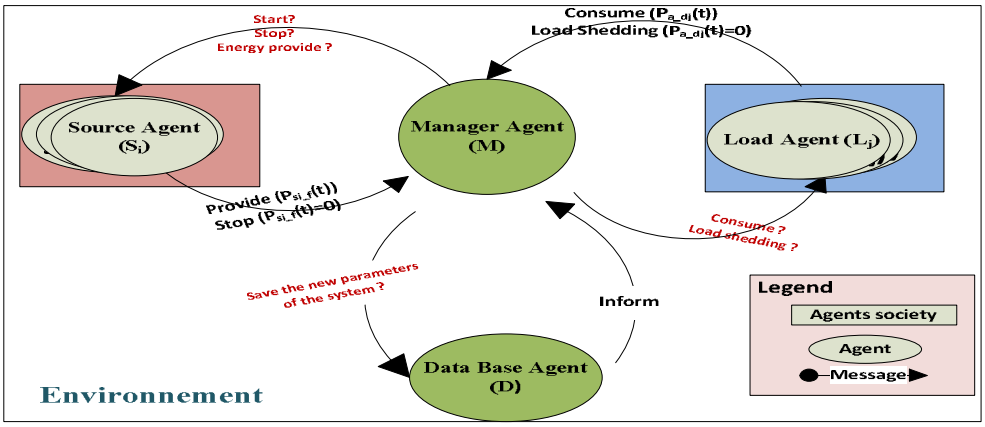

Figure 4. Model of energy management system.

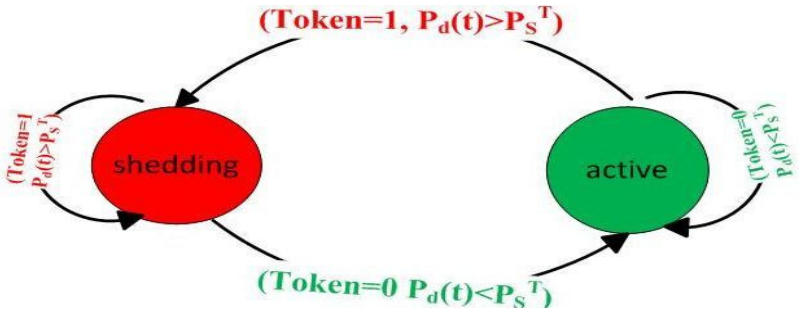

Figure 5. Behavioral model of load agent.

Source agent

According to the demand and the characteristics of the source, a Source Agent can be in four (4) different states: active, reserve, available and stop (Figure 3). A Source Agent

(i) is in the «stop» state when it cannot run because of a maintenance case following a breakdown, incident, etc., Its priority is then zero (p_s = 0). It goes into the available state as soon as it is functional again.
(ii) changes from the stop state to the available state when it can run, its priority is then evaluated and is positive. It may at any time switch to the reserve state according to the request and its priority.
(iii) is in the reserve state when it is ready to provide energy. Its production is equal to zero (0). This allows regulation of the frequency by continuous adaptation of the production level to that of the consumption. It goes into the active state according to the demand and its priority.
(iv) is in the active state when it supplies energy. In this state its priority is the greatest of all those of the agents that are in other states.
With:
(v) Δf (Hz) is the variation of the system frequency, it is equal to the absolute value of the difference between the frequency (f) (Hz) of the system at t time and the reference frequency (f_0 = 50 Hz) (Δf =| f-f_0 | Hz). It is the direct image of the imbalance between the production and the consumption.
(vi) $p_{s(re)min}$ is the lowest source priority among the sources that are in the reserve state.
(vii) $p_{s(re)max}$ is the priority of the most favorable source among the sources that are at the reserve state.
(viii) $p_{s(av)max}$ is the priority of the most favorable source among the sources that are in the available state.
(ix) $p_{s(ac)min}$ is the lowest source priority among the sources that are in the active state.

Load agent

Load Agent (Ag_L) of the system is in an active state or in a shedding state as shown in Figure 5. The management of load shedding is done following attribution of a token «shedding». Load agents having the token « shedding» can pass from the active state to the load shedding state.
Where: P_d *(t)* is equal to the instantaneous power called by all departures; P_S^T is the total power available in the electrical network.

Power system

An electrical grid similar to that of Senegal was deliberately chosen (Table 2). This table provides a description of the power plants and generators, types of fuel, power installed. More than 88% of the production are of thermal origin. This makes it possible to get closer to reality.

Table 2. Production park of power network.

Power plants	Generators	Fuels	Installed power (MW)	Power plants	Generators	Fuels	Installed power (MW)
C1	Source1 1	Heavy fuel	15.95	C5	Source5 2	Diesel oil	18
	Source1 2	Heavy fuel	15.95		Source5 3	Kerosene	36
	Source1 3	Heavy fuel	15.95		Source5 5	Diesel oil	30
	Source1 4	Heavy fuel	15.95		Source6 1	Diesel oil	15
C2	Source2 1	Heavy fuel	18	C6	Source6 2	Diesel oil	15
	Source2 2	Heavy fuel	18		Source6 3	Diesel oil	15
	Source2 3	Heavy fuel	18		Source6 4	Diesel oil	15
	Source2 4	Heavy fuel	15	C7	Source7 1	Hydraulic	60
	Source2 5	Heavy fuel	15		Source8 1	Heavy fuel	20
C3	Source3 1	Heavy fuel	67.5	C8	Source8 2	Heavy fuel	13
C4	Source4 1	Naphtha	50		Source8 3	Heavy fuel	20

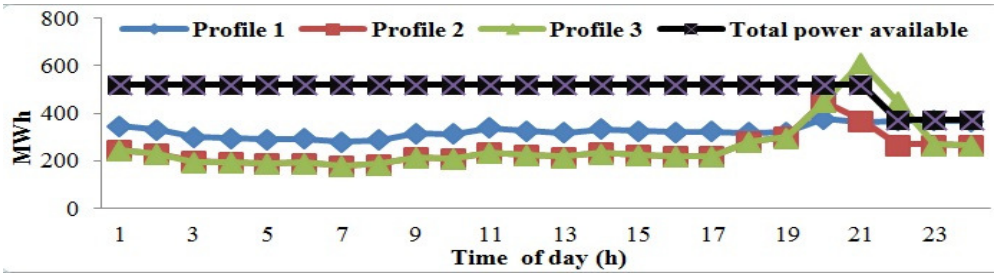

Figure 6. Profiles of the power demand of the network.

RESULTS AND DISCUSSION

To test the simulation model presented previously, three scenarios were set up to show the behavior of the system as clearly as possible.

Load profiles

To test the simulation model presented previously, three different load profiles were used (Figure 6). The first load profile is characterized by a nearly constant demand around 350 MW. The second profile is characterized by a peak power high demand of more than 37% within an interval of one hour. The third profile is characterized by a power demand exceeding the available power equal to 522.3 MW. Several scenarios were simulated in order to show the behavior of the system as clearly as possible.

Scenarios

The simulations were carried out following three criteria:

An optimization criterion based on minimizing the production cost, a criterion based on the minimization of the amount of GHG emissions released and a criterion based on random rules. A test scenario consisted in simulating the behavior of the system when the power system presented below, a given load profile (1, 2, 3) and a given optimization criterion (minimizing the production cost or minimization of the amount of GHG) were applied. Several simulations of each load profile were also performed with a generator assessment criterion based on random rules. The results of various simulations were then compared. Those scenarios made it possible to highlight the robustness and effectiveness of the management system.

Simulation results

The results obtained with the first two criteria (cost and GHG) are compared to the third criterion (random). Figures 7, 8, 9, 10, 11, 12 and 13 show the results of different simulations with the platform.

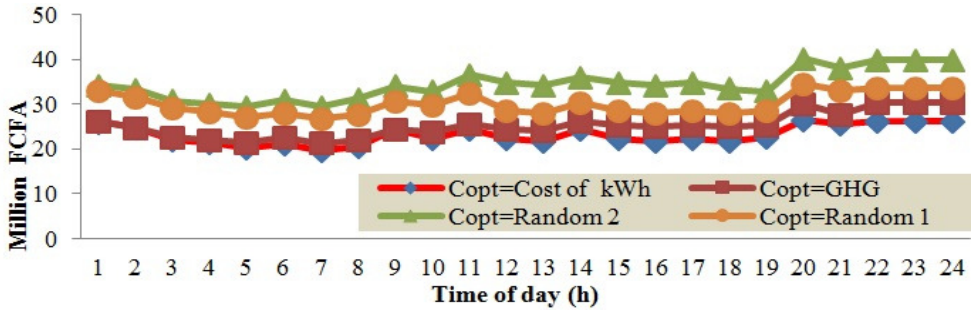

Figure 7. Production sources operating costs (Profile 1).

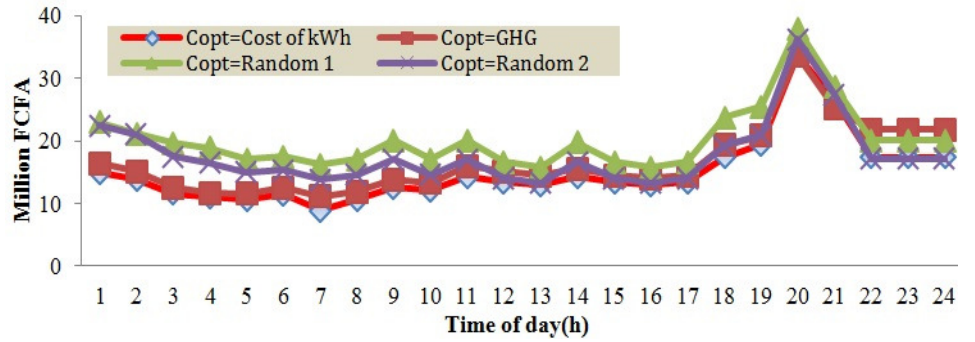

Figure 8. Production sources operating costs (Profile 2).

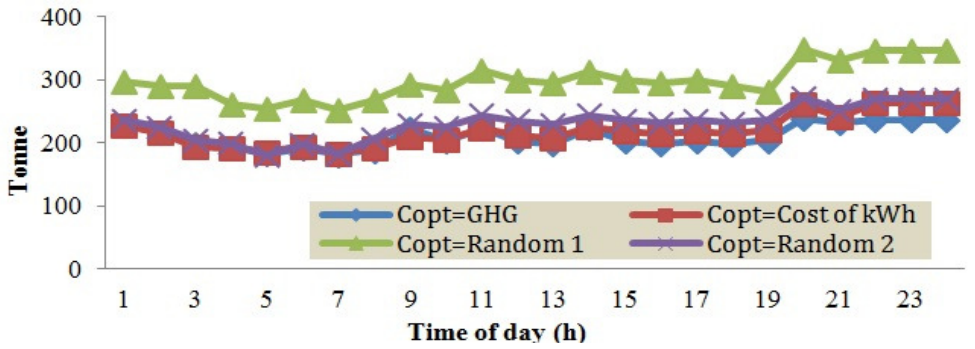

Figure 9. CO_2 quantity (Profile 1).

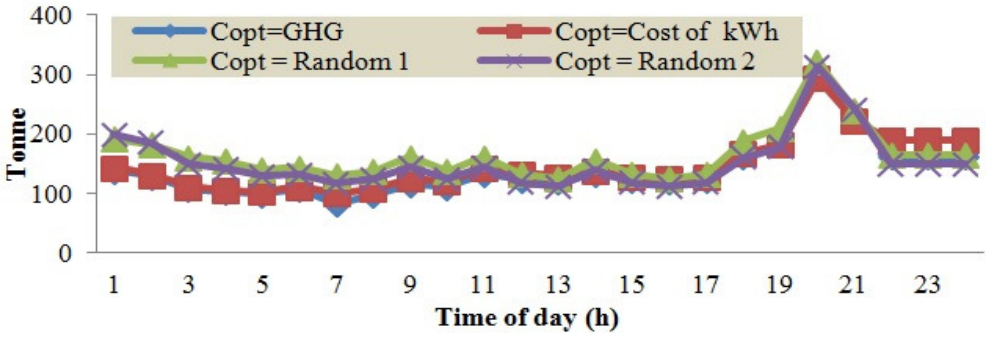

Figure 10. CO_2 quantity (Profile 2).

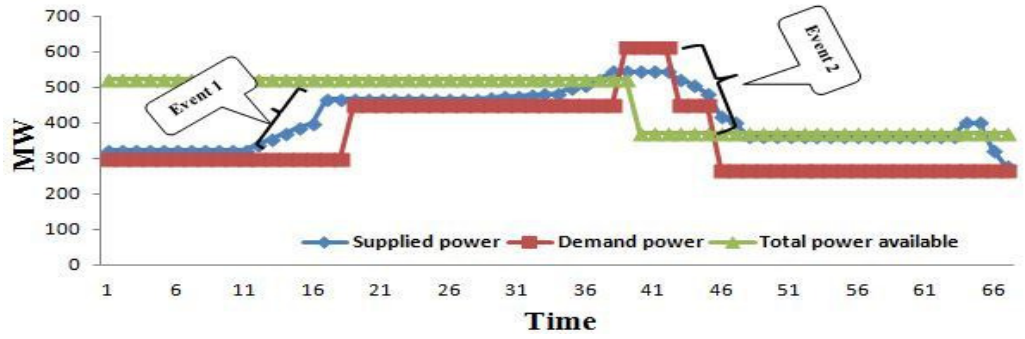

Figure 11. Behavior of management system on the critical moments of the day (between: 19 to 23 h).

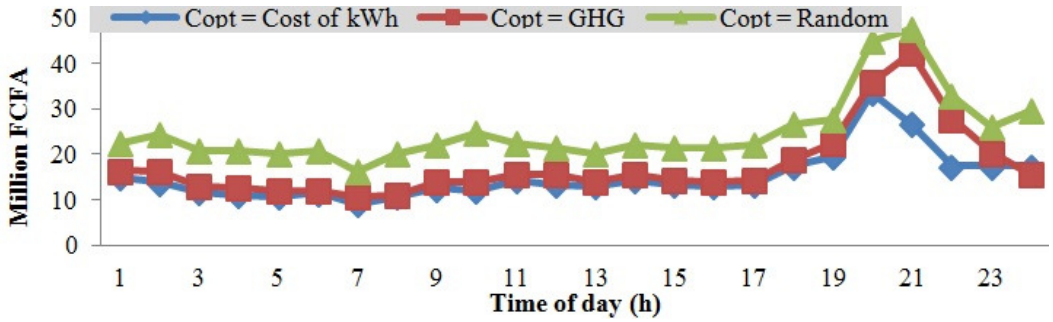

Figure 12. Production sources operating cost (Profile 3).

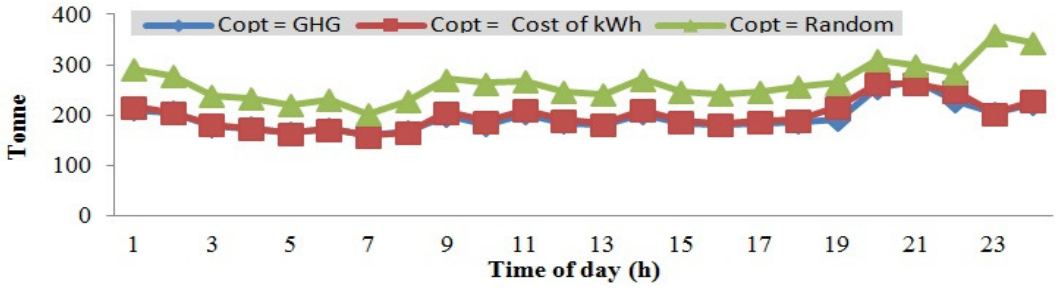

Figure 13. CO_2 quantity (Profile 3).

Results obtained with the first and second scenarios

Optimization criterion: The kWh production cost: Figures 7 and 8 show the operating costs of generation sources obtained respectively with Profile 1 and 2. The results show that the optimal cost is always lower than the cost obtained with the criterion based on random rules.

Optimization criterion: The amount of greenhouse gas emissions: Figures 9 and 10 show the amount of CO_2 released by the sources of production respectively with Profile 1 and 2. The difference between the results obtained by random criterion and optimized criterion remains significant for the amount of GHG released.

Results obtained with the third scenario

The third load profile shows the behavior of the system facing load shedding. Figure 11 shows many fluctuations between 19 to 23 h with a power peak of the demand exceeding the total power available (P_S^T) of the electrical network, a power loss in the production facilities and a departure opening (load shedding). The management system always tries to balance the inbalance between the

energy production and consumption quickly. For the disturbances brought to the electrical network, the reaction time always remains in the interval [0 50] seconds.

Event 1: satisfaction of the 20 h demand (duration of the event 35.39 s); Event 2: peak (exceeding the total power PT), shedding load, satisfaction of demand, (duration of the event 48.9 s).

Optimization criterion: The kWh production cost

Figure 12 shows the operating cost of generating sources obtained with the simulation. The input data of the system are those of Profile 3. Costs obtained with the optimization criterion kWh cost are still lower than all other costs.

Optimization criterion: The amount of greenhouse gas emissions

Figure 13 shows the amount of CO_2 emitted by the sources of production respectively with Profile 3.

Conclusion

The work presented in this paper proposed a design and implementation of a simulation platform for decentralized management based on a multi-agent system. Using a located multi-agent paradigm built model seemed then to be an innovative and promising option for the development of decision support tools. The methodology adopted in this paper set up a control strategy over the agents in order to organize, schedule and interpret the amount of information exchanged between the different entities of the system. The results later achieved with the established platform showed that the optimized production costs of the arrangements of the energy sources by the platform were always better than any other arrangement. The platform also made it possible to assess and minimize the amounts of GHG released by the electrical system. Some incompatibility on the simultaneous satisfaction of the two optimization criteria was noted. The explanation is that generators, whose production cost is cheapest, are the most polluting of the power source.

One of the prospects of this work is to find an arrangement of production sources for optimal operation, taking into account two optimization criteria: the network operation cost and the quantity of greenhouse gas emissions. The other prospect focuses on the diversification of the production sources by integrating the renewable energies. Indeed, new energy sources such as wind, solar generators, are getting into our electrical systems and the user will increasingly be confronted with energy prices varying according to the supplier, the date and the time. It is in this varied and dynamic context of production and energy consumption that a «smart» control system takes all its importance from both consumption and pricing points of view (production).

ACKNOWLEDGEMENTS

The authors wish to thank the Direction de la Qualité, de la Sécurité et de l'Environnement (DQSE) of Sénégal and particularly Mr DIOP Moussa.

NOMENCLATURE

Ag_D Database Agent
Ag_L Departure Agent
Ag_M Manager Agent
Ag_S Source Agent
C_{S_i} Cost of kWh of the energy source
Q_{S_i} Quantity of fuel burned in the energy source
E_G Total emission of greenhouse gases (kg)
$E_{G,F}$ Emission of a given GHG per fuel type (kg)
$E_{G,F,T}$ Emission of a given GHG per fuel type and per technology (kg)
$E.F_{G,F}$ Emission factor of a given GHG per type of fuel used (kg/GJ)
$E.F_{G,F,T}$ Emission factor of a given GHG per fuel and per technology (kg/GJ)
P_D^T Total power Demand (W)
P_S^T Total power Supplied (W)
$P_{(state)min}$ Minimum power allowable in a state (W)
$P_{(state)max}$ Maximum power allowable in a state(W)
p Operating priority of a system agent (GJ)
Q_F Quantity of fuel burned in energy unit
$Q_{F,T}$ Quantity of burned fuel per energy unit per technology type (GJ)
GHG Greenhouse Gases

REFERENCES

Amit G, Kainou K, Tinus P (2006). Chapitre 2: Combustion stationnaire. Lignes directrices du GIEC, vol. 2 Energie, P. 53.
Butler-Purry KL, Sarma NDR, Hicks IV (2004). Service restoration in naval shipboard power systems. IEE Generation, Transmission, Distribution, 151:1.
Cristaldi L, Monti A, Ottoboni R, Ponci F (2003). Multi-agent based power systems monitoring platform: a prototype. IEEE Power Tech. Conf. 2(5).
Dimeas AL, Hatziargyriou N (2005a). Operation of a multiagent system for microgrid control. IEEE trans. power syst. 20(3):1447-1455.
Dimeas AL, Hatziargyriou ND (2004). A multi-agent system for microgrids. IEEE Power Eng. Soc. General Meeting, 1: 55-58.
Dimeas A, Hatziargyriou N (2005b). A MAS architecture for microgrid control . In Proc. the 13th International Conference on Intelligent Systems Application to Power Systems, November, P. 5.

Logenthiran T, Srinivasan D, Khambadkone AM, Aung HN (2012). Multiagent system for real-time operation of a microgrid in real-time digital simulator. IEEE Transactions on Smart Grid, Article number 6180026, 3(2):925-933.

Mao Meiquin, Dong W, Liuchen C (2011). Design of a novel simulation platform for the EMS-MG Based on MAS.IEEE Energy Conversion Congress and Exposition: Energy Conversion Innovation for a Clean Energy, pp. 2670-2675.

Monica A, Hortensia A, Carlos AO (2012). Integration of renewable energy sources in smart grids by means of evolutionary optimization algorithms. Expert Syst. Applications, 39(5):5513–5522.

Nagata T, Sasaki H (2002). A multi-agent approach to power system. IEEE Transactions on Power Systems, May 2002, 17:457-462.

Phillips L, Link H, Smith R, Weiland L (2006). Agent-based control of distributed infrastructure resources. Sandia National Laboratories, SAND2005-7937. Available: www.sandia.gov/ scada/documents/sand_2005_7937.pdf.

Pipattanasomp M, Feroze H, Rahman S (2009). Multi-Agent Systems in a Distributed Smart Grid: Design and Implementation. IEEE PES Power Systems Conference and Exposition (PSCE'09), Seattle, Washington, USA.

Richalet J (1987). Modélisation et identification des processus . Techniques de l'ingénieur R7140.

Wang HF (2001). Multi-agent co-ordination for the secondary voltage control in power system contingencies. IEE Generation, Transmission Distribution, 148:61-66.

UPCOMING CONFERENCES

ICNMB 2013 : International Conference on Nuclear Medicine and Biology Switzerland, Zurich, July 30-31, 2013

International Conference on Mathematical Modeling in Physical Sciences Prague, Czech Republic, September 1-5, 2013

Conferences and Advert

July 2013
ICNMB 2013 : International Conference on Nuclear Medicine and Biology
Switzerland, Zurich, July 30-31, 2013

September 2013
International Conference on Mathematical Modeling in Physical Sciences
Prague, Czech Republic, September 1-5, 2013

International Journal of Physical Sciences

Related Journals Published by Academic Journals

- *African Journal of Pure and Applied Chemistry*
- *Journal of Internet and Information Systems*
- *Journal of Geology and Mining Research*
- *Journal of Oceanography and Marine Science*
- *Journal of Environmental Chemistry and Ecotoxicology*
- *Journal of Petroleum Technology and Alternative Fuels*

academicJournals